WIPFGN

DOE/ET-0058/4

PE-16 Swell - 42
- Tensile - 48
Mo Band DBTT - 89

Alloy Development for Irradiation Performance

Quarterly Progress Report

~~January-March, 1978~~ October - December '78

May 1979

U.S. Department of Energy
Assistant Secretary for Energy Technology
Office of Fusion Energy

DOE/ET-0058/4
uc-20. 20c

Alloy Development for Irradiation Performance

Quarterly Progress Report
~~January-March, 1978~~

May 1979

U.S. Department of Energy
Assistant Secretary for Energy Technology
Office of Fusion Energy
Washington, DC 20545

Available from:

National Technical Information Service (NTIS)
U.S. Department of Commerce
5285 Port Royal Road
Springfield, Virginia 22161

Price: **Printed Copy:** $ 7.25
Microfiche: $ 3.00

FOREWORD

This report is the fourth in a series of Quarterly Technical Progress Reports on *"Alloy Development for Irradiation Performance"* (ADIP), which is one element of the Fusion Reactor Materials Program, conducted in support of the Magnetic Fusion Energy Program of the U.S. Department of Energy. Other elements of the Materials Program are:

- *Damage Analysis and Fundamental Studies (DAFS)*
- *Plasma-Materials Interaction (PMI)*
- *Special-Purpose Materials (SPM)*

The ADIP program element is a national effort composed of contributions from a number of National Laboratories and other government laboratories, universities, and industrial laboratories. It was organized by the Materials and Radiation Effects Branch, Office of Fusion Energy, DOE, and a Task Group on *Alloy Development for Irradiation Performance*, which operates under the auspices of that Branch. The purpose of this series of reports is to provide a working technical record of that effort for the use of the program participants, for the fusion energy program in general, and for the Department of Energy.

This report is organized along topical lines in parallel to a Program Plan of the same title so that activities and accomplishments may be followed readily relative to that Program Plan. Thus, the work of a given laboratory may appear throughout the report. Chapters 1, 2, 7, and 8 review activities on analysis and evaluation, test methods development, status of irradiation experiments, and corrosion testing and hydrogen permeation studies, respectively. These activities relate to each of the alloy development paths. Chapters 3, 4, 5, and 6 present the ongoing work on each alloy development path. The Table of Contents is annotated for the convenience of the reader.

This report has been compiled and edited under the guidance of the Chairman of the Task Group on *Alloy Development for Irradiation Performance*, E. E. Bloom, Oak Ridge National Laboratory, and his efforts, those of the supporting staff of ORNL and the many persons who made technical contributions are gratefully acknowledged. T. C. Reuther, Materials and Radiation Effects Branch, is the Department of Energy Counterpart to the Task Group Chairman and has responsibility for the ADIP Program within DOE.

Klaus M. Zwilsky, Chief,
Materials and Radiation Effects Branch
Office of Fusion Energy

CONTENTS

1. ANALYSIS AND EVALUATION STUDIES

The designs for power-producing fusion reactors are in a very embryonic and rapidly changing state, Requirements for materials performance are thus not well defined. However, regardless of the final designs, the environment will clearly be extremely demanding on materials in regions of high neutron flux. One cannot identify a class of alloys on which the development efforts should focus — thus the parallel paths of the Alloy Development Program. The combination of reactor designs that are evolving and the necessity for including alloys with widely different physical, chemical, and mechanical properties in the program could lead to an impossibly large number of potential problems and possible solutions. Analysis and evaluation studies are an essential part of the Alloy Development Program in order to translate fusion reactor performance goals into material property requirements and to identify crucial and generic problems on which development activities should be focused. As the Alloy Development Program proceeds and a better understanding of the behavior of materials in potential fusion reactor environments is attained, these studies will also identify problems that will necessitate design solutions.

2. TEST MATRICES AND TEST METHODS DEVELOPMENT

An important part of the alloy development effort is the definition of test matrices and development of test methods. The alloy development strategy will proceed through stages requiring tests of generally increasing difficulty and complexity.

1. Scoping tests will be used to make relative judgments between materials and metallurgical conditions and to identify critical properties. Such tests, which will be used where large numbers of variables are involved, must be rapid, simple, and decisive.

2. Developmental tests will be used for optimization of the Prime Candidate Alloys. They will be broader and more extensive than the scoping tests. In-reactor testing will be an important part of this work.

3. Engineering property tests will be devised to provide the broad data base needed for reactor design.

2.1 ADAPTATION OF AN ELECTRICAL POTENTIAL TECHNIQUE TO MEASURE FATIGUE CRACK GROWTH - J. L. Straalsund and D. A. Mervyn

(Hanford Engineering Development Laboratory)

2.1.1 ADIP Task

Task I.A.2, define test matrices and test procedures.

2.1.2 Objective

An electrical potential technique to measure crack growth was developed to facilitate the high volume of postirradiation testing necessary to characterize the fatigue behavior of fusion first wall materials.

2.1.3 Summary

An adaptation of an electrical potential technique to measure crack growth on miniature center-cracked specimens has been shown to produce reliable, accurate results. Measurement of crack growth rate (da/dN) using this technique is at least as accurate as visual methods. As developed, the technique is conducive to high-volume postirradiation fatigue crack growth testing.

2.1.4 Progress and Status

Since current fusion reactor concepts are cyclic in nature, it becomes important to characterize the fatigue behavior of first wall materials. In fact, wall life predictions for 316 SS indicate fusion reactor shut-down from the growth of crack-like flaws before the effects of fatigue or creep and stress rupture can alter first wall life. Since little postirradiation fatigue crack growth testing has been done, a large data base needs to be established in order to characterize fusion materials.

By adapting an electrical potential technique to measure crack growth on miniature specimens, the feasibility of conducting the high volume postirradiation fatigue crack growth testing necessary to characterize fusion materials has been demonstrated. Since this technique eliminates the typical visual measurement of crack extension, crack growth can be monitored continuously on irradiated specimens in a hot cell environment with a high degree of accuracy.

The electrical potential technique entails passing a constant d.c. current through a miniature center cracked specimen underload, Figure 2.1.1, and measuring the potential difference between two points on either

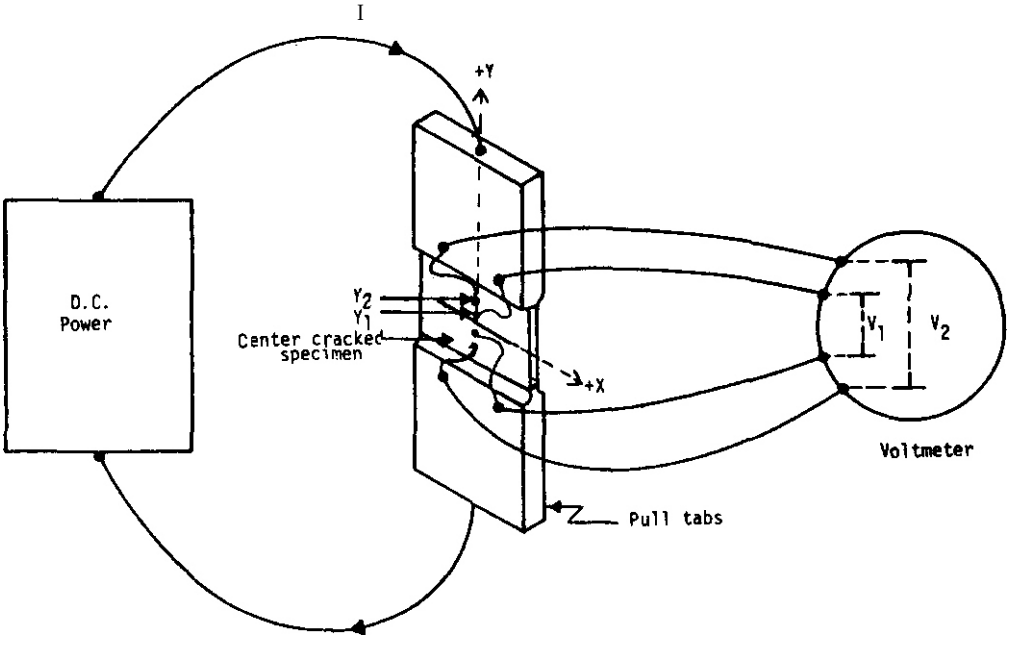

Figure 2.1.1. Crack Measurement Details.

side of the crack. As the crack propagates the current path increases and accordingly the output voltage increases. By measuring the potential difference at two distances, Y_1 and Y_2, from the crack, a voltage ratio V_1/V_2 can be obtained which eliminates material dependent parameters which may vary from test to test or under irradiation conditions. This is a direct result of Ohm's Law which for our specimen geometry can be written as:

$$V_i = f\ (a,\ Y_i) \qquad \text{Equation 1}$$

or

$$\frac{V_1}{V_2} = \frac{f\ (a,\ Y_1)}{f\ (a,\ Y_2)} \qquad \text{Equation 2}$$

where V_i is the potential difference measured at a distance Y_i from the crack, a the half crack length, and $f(a, Y_i)$ a geometric function.

Material dependent variable such as thickness, resistivity, and initial crack length are eliminated by obtaining this voltage ratio which is simply a geometric function of the half crack length and potential probe placement.

The miniature specimen used in this study was 1.27 cm by 2.54 cm (0.5 inches by 1.0 inches) 26 gauge 304 SS electron beam welded pull tabs. The development of this miniature specimen design was reported previously.[2] The size of the specimen permits irradiation in-reactor, and data obtained from this miniature specimen produce reliable, accurate results. A 0.38 cm EDM slit was used as a starter notch. Two sets of 1.27×10^{-2} cm (5 mil) diameter stainless steel wire probes were spot welded to the specimen, the first as close to the crack as possible (approximately 6.35×10^{-2} cm from center) and the second as far from the crack as possible yet still on the specimen (approximately 9.47 cm from center).

Specimens were cycled using a MTS feedback-controlled test machine using load as the control parameter at 300 lb. maximum load, 15 Hz, and load ratio (R) of 0.05. A constant 5 amp d.c. current was supplied to the specimen from a Kepco 55 volt power supply through a 1 ohm resistor. Measurements of V_1 and V_2 were made using a Doric integratin- microvoltmeter while crack length was measured using a traveling micrometer.

In this manner a calibration curve relating voltage ratio V_1/V_2 to half crack length was generated, Figure 2.1.2. Once a calibration curve has been established for a particular specimen geometry and probe placement crack length can be determined in subsequent tests by simply measuring the voltage ratio. This can be accomplished without interrunti-no the test. Data obtained by this technique exhibit excellent agreement with a theoretical solution for the potential drop across a crack in a center-cracked specimen proposed by H. H. Johnson.[3] For the miniature specimen and potential probe placement, this function can be written in the following form:

$$\frac{V_1}{V_2} = \frac{\cosh^{-1}\left(\frac{\cos \frac{\pi Y_1}{2W}}{\cos \frac{\pi a}{2W}}\right)}{\cosh^{-1}\left(\frac{\cos \frac{\pi Y_2}{2W}}{\cos \frac{\pi a}{2W}}\right)} \qquad \text{Equation 3}$$

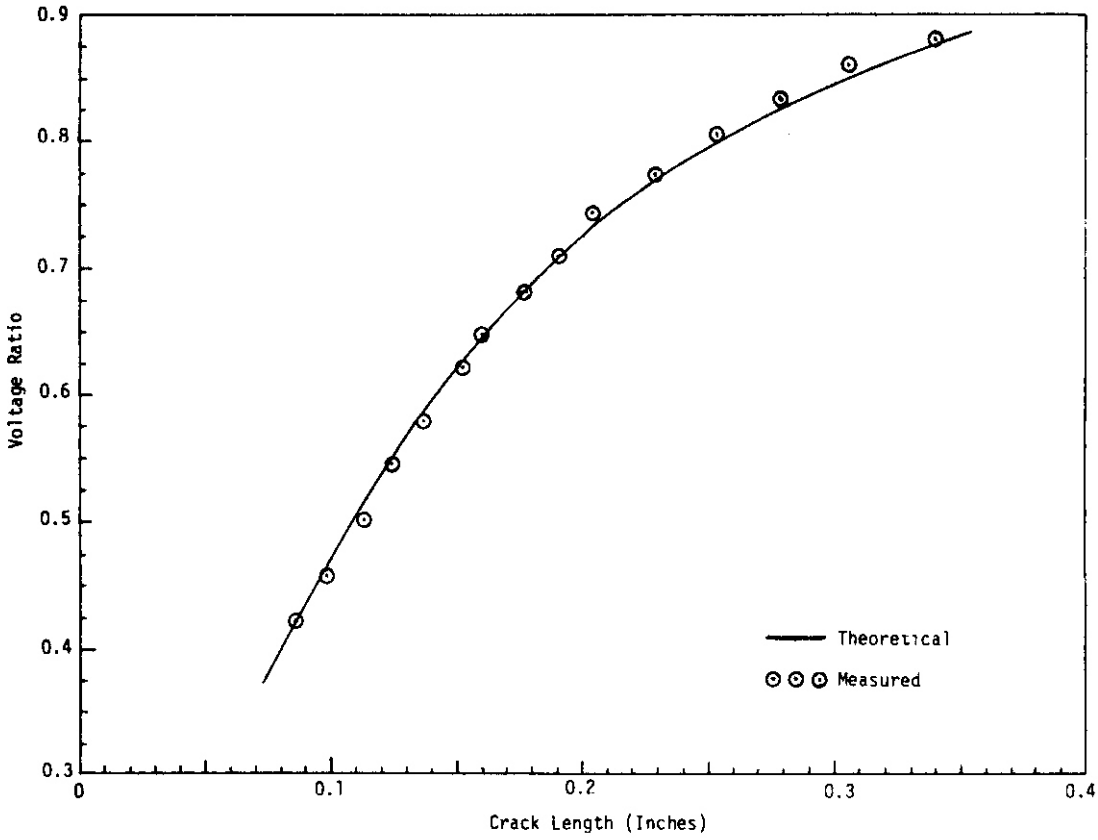

Figure *2.1.2.* Electrical Potential Calibration Curve.

The theoretical solution emphasizes that the measured voltage at Y_2, farthest from the crack, is more sensitive to probe positioning than V_1. The magnitude of error in crack growth rate generated by an error in lead placement was determined **using** Equation 3, Figure 2.1.3. The accumulated error in voltage ratio measurements as a function of lead placement error over an entire test was considered, that is crack growth from 0.38 cm to 2.03 cm. For a 1.27 **x** 10^{-2}cm (5 mil) error in lead placement, a 0.8% error in crack growth measurement was generated from lead **1** and *2.4%* from lead *2*. This corresponds to a 2.5% error in calculated fatigue crack growth rate, da/dN. For a *2.54* **x** 10^{-2}cm (10 mil) error in probe positioning the error generated in crack growth measurements is 1.7% and 4.8%, for lead **1** and **2** respectively. This is a 5.1% error in the calculated crack growth rate da/dN. This magnitude of error is comparable with that associated with typical visual measurements. The effect of horizontal error in lead placement is more difficult to

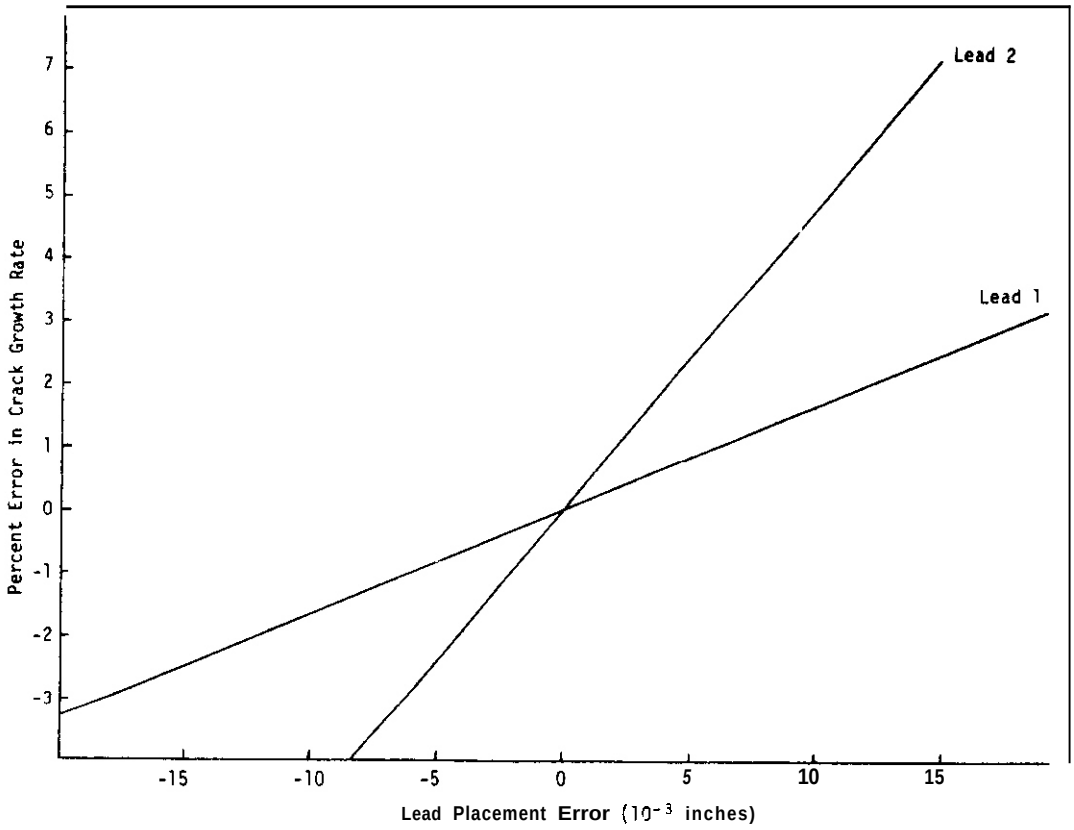

Figure 2.1.3. Lead Placement Effects.

assess although it is expected to be much less than the error associated with vertical positioning.

Presently, multiple tests of various lead placements are being conducted to verify the reproducibility of the electrical potential data. Testing at elevated temperatures to determine the effect of temperature gradients on the results is the next step in this feasibility study.

2.1.5 Conclusions

1. An electrical potential technique has been developed to measure fatigue crack growth in center-cracked specimens. The technique produces reliable, accurate results and can be adopted to a miniature specimen easily irradiated in-reactor.

2. Since the technique is condusive to high volume postirradiation testing, the feasibility of generating a large data base necessary to characterize the fatigue crack growth behavior of fusion materials has been demonstrated.

2.1.6 References

1. R. E. Gold, et al., "Technical Assessment of Vanadium-Base Alloys for Fusion Reactor Applications," *Department of Energy Report* COO-*4540-1,* April 1978, Westinghouse Electric Corporation.

2. L. A. James, R. E. Bauer, and J. L. Straalsund, "Development of Small Fatigue-Crack Growth Specimens for In-Reactor and Postirradiation Testing," *Alloy Development for Irradiation Performance Quarterly Progress Report for Period Ending June 30, 1978.*

3. H. H. Johnson, "Calibrating the Electrical Potential Method for Studying Slow Crack Growth," *Materials Research and Standards,* 5 (1965).

2.2 DESIGN OF MATERIALS IRRADIATION EXPERIMENTS UTILIZING SPECTRAL TAILORING — T. A. Gabriel, K. R. Thoms, and J. W. Woods (ORNL)

2.2.1 ADIP Task

ADIP Task I.A.2, Define Test Matrices and Test Procedures.

2.2.2 Objective

In order to reproduce in approximately real time in fission reactors the ratio of helium to displacements per atom (He/dpa) expected near or at the first wall in fusion reactors for stainless steel and nickel-base alloys, the thermal-to-fast neutron flux ratio within the experimental locations must be varied since the He production will be dominated by the thermal flux and the fast flux will determine the dpa. The objective of this work is to determine the amount of variation necessary and to design experimental capsules that will produce the needed changes.

2.2.3 Summary

We calculated the effects of C-3 core piece composition and added fuel loaded around the C-3 position in the ORR. Adding 20 g fuel in each of the positions B-3, C-4, and D-3 reduces the thermal flux by about 4% and increases the dpa by about 6%. Additional calculations are contemplated for larger fuel loadings. A conceptual design of the experimental vehicle has been completed and the core pieces required for the first two stages or spectral tailoring are being fabricated. The composition of the experimental capsule differs from that used in the initial scoping calculations. As soon as final detailed information on the composition becomes available, the neutron flux and dpa will be recalculated. Calculations are in progress to obtain cross sections for neutron absorbers to be used in the latter stages of spectral tailoring to reduce the thermal flux.

2.2.4 Progress and Status

The ORR core loading that was used in the VENTURE[1] calculations is shown in Fig. 2.2.1. By varying the amounts of water and aluminum

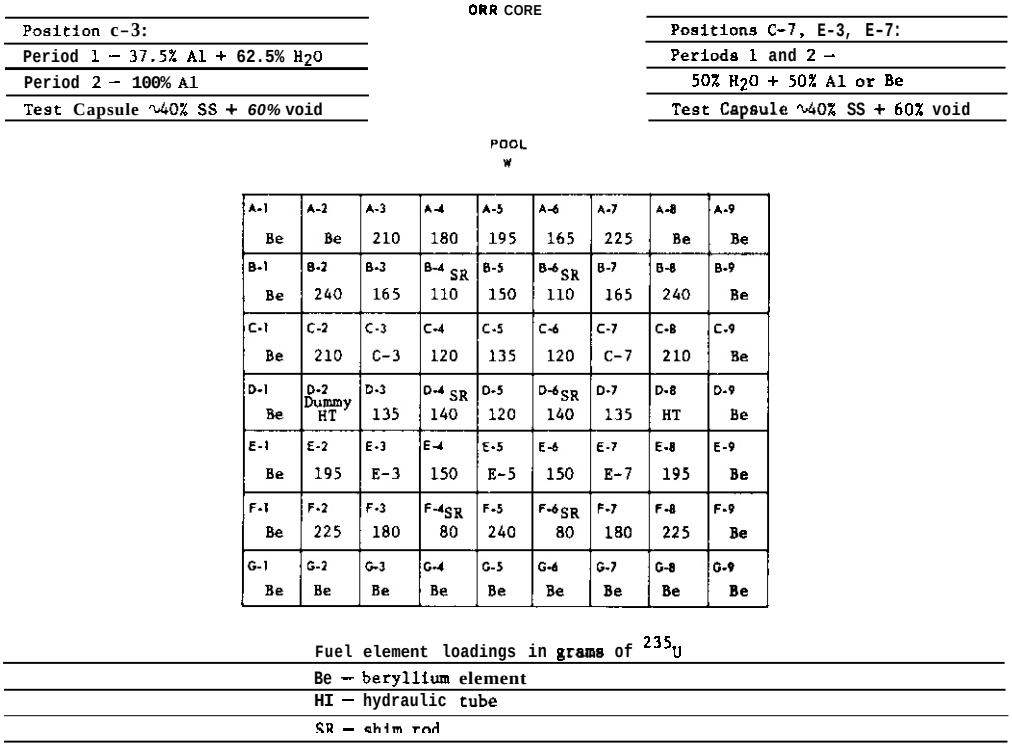

Fig. 2.2.1. ORR Core Loading for Neutronics Calculations.

in the C–3 core piece (76.2 by 76.2 mm) surrounding the experimental capsule, which has an effective radius of 22.2 mm, the thermal neutron flux and dpa rate can be modified. This variation is shown on the right side of Fig. 2.2.2. These data have been used to specify the design of the core piece for the first two periods of irradiation. During the first period of irradiation, the core piece will be composed of about 63% H_2O and 37% Al. During the second period, the core piece will be nearly all aluminum with minimum water cooling (<2%). The resultant dpa and gas production correlation for the first two irradiation periods is shown in Fig. 2.2.3. The solid line is for the first wall of a fusion reactor at 1 MW/m^2. Because the composition of the experimental capsule has changed since these calculations were performed, additional calculations will be necessary to check the sensitivity of the dpa rate and helium production to these changes.

The changes in the thermal neutron flux and the dpa rate resulting from additional fuel (20 g each to B–3, C–4, and D–3) around the C–3 core piece are shown on the left side of Fig. 2.2.2.

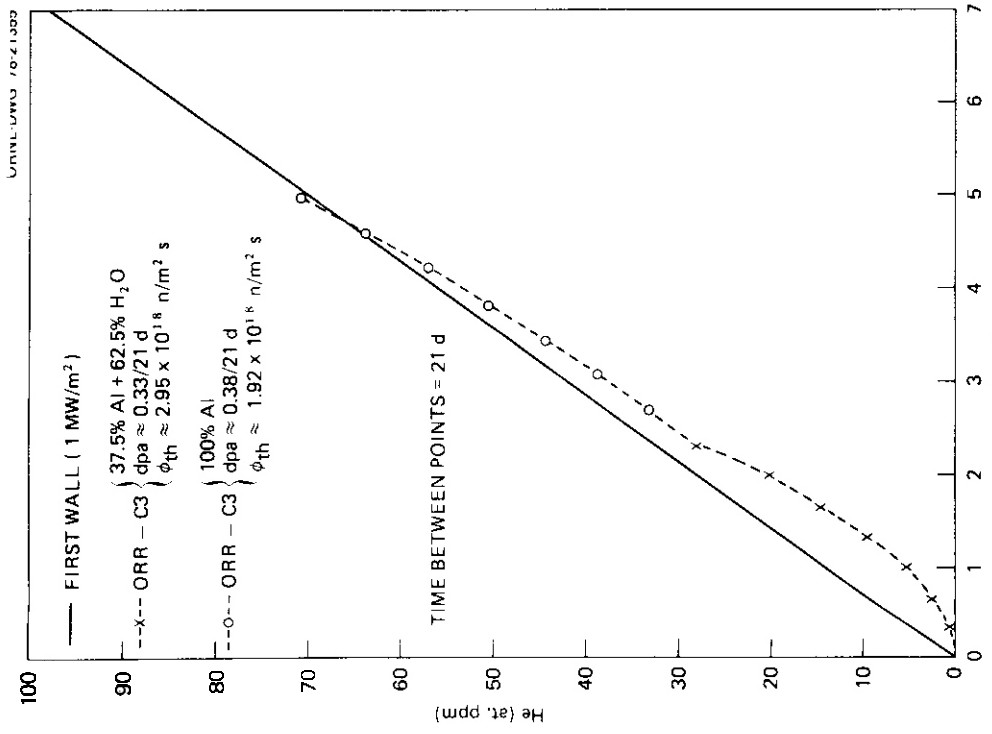

Fig. 2.2.3. Helium versus Displacement Production Expected on First Wall of Fusion Reactor and What Can Be Obtained in ORR-C-3.

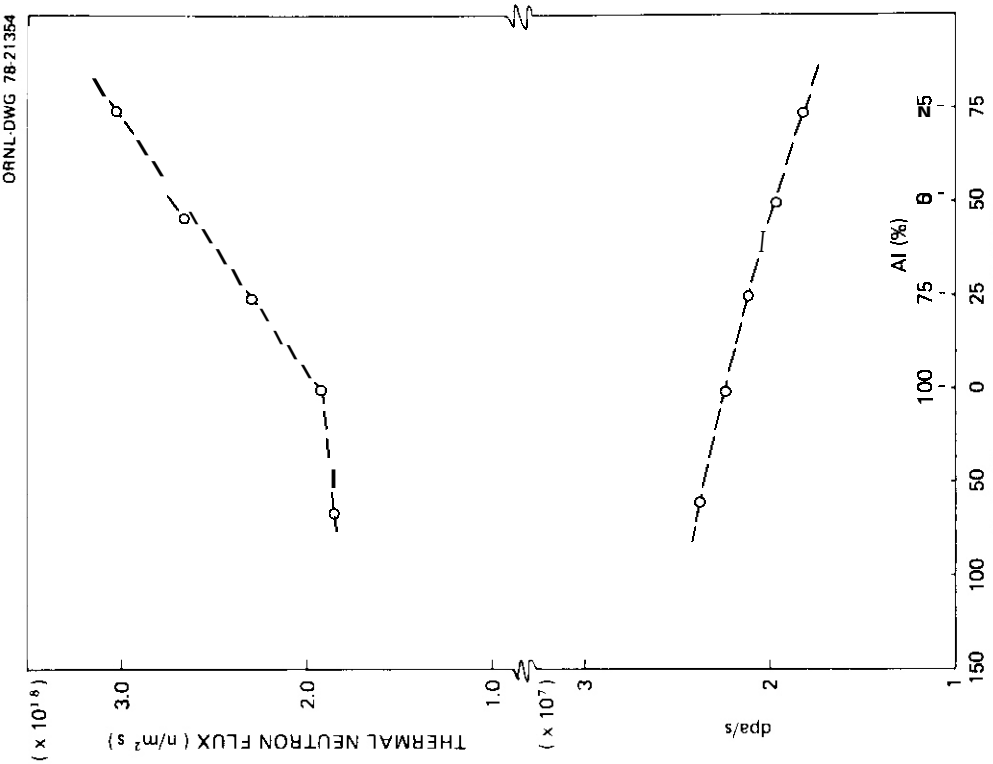

Fig. 2.2.2. Variation in the Displacement Rate and Thermal Neutron Flux in the C-3 Position in ORR as Functions of Core Piece Composition and Fuel Loading Around C-3.

The calculations were done for a 100% Al core piece surrounding the experimental capsule. The results indicate that the thermal flux can be reduced by about 4% and the dpa can be increased by about 6%. In a previous progress report, a 15% increase in the dpa was set as the goal to reach. Additional calculations are contemplated for larger fuel loadings. To obtain larger decreases in the thermal flux, the aluminum core piece must be replaced by neutron absorbers, such as tantalum or tungsten. The calculations to obtain cross sections for these elements are in progress. These cross sections are difficult to produce and verify.

The first two core pieces are presently being fabricated. The neutronics calculations called for the first core piece to have a cross-sectional area (exclusive of the capsule) of 37.5% Al and 62.5% H_2O and the second core piece to be solid aluminum with a minimum of water. We have developed a design for the first core piece, which has a cross-sectional area of 37.1% Al and 62.9% H_2O. The second core piece will be solid aluminum with a 47.0-mm (1.85-in.) hole to accomodate the capsule and allow a 1.27-mm (0.050-in.) coolant water annulus. The cross-sectional area (exclusive of the capsule) will be 96.0% Al and 4.0% H_2O. We have ordered two of each of these core pieces, with delivery of one of each expected by January 1, 1979. The first of each type core piece will be used in the reactor, while the second will be used as spares and to check fitup of the capsule in the ORR mockup. The first of these core pieces will also be used to determine the gamma heating rate that the capsule will be subjected to during irradiation. This information is necessary to perform an accurate thermal design of the proposed capsule.

A conceptual design of the proposed spectrum tailoring experiment has been developed. A schematic of the portion of the capsule that will be in the reactor tank is shown in Fig. 2.2.4. As can be seen, the in-core section of the capsule will contain four specimen holder cans. The specimens in these cans will operate from top to bottom at 250, 450, 550, and 350°C. Since these capsules must be capable of being reloaded with radioactively hot specimens, special assembly techniques and procedures must be developed. The proposed design

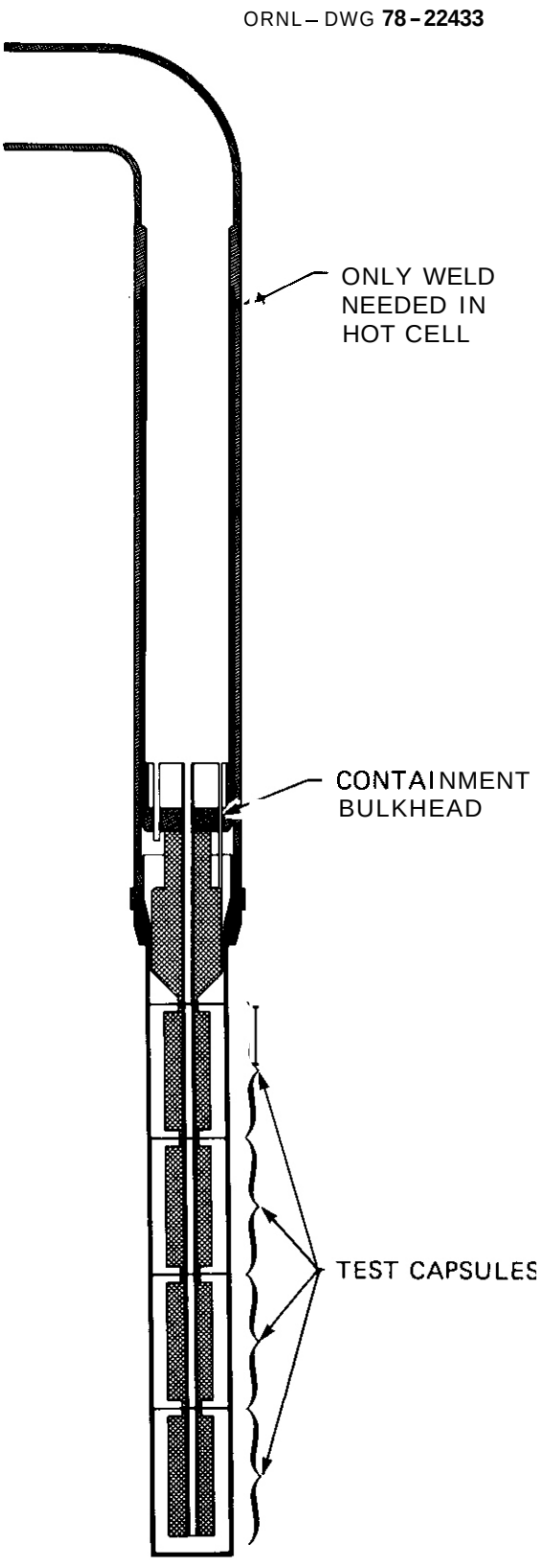

Fig. 2.2.4. Schematic of Proposed Spectrum Tailoring Experiment.

should allow the assembly of everything outside of a hot cell, with the exception of the specimen holder cans and the primary containment vessel. The specimen cans must be loaded within a hot cell and positioned in place on a spline, the primary containment must be slipped over the cans, and one weld must be made to seal the primary containment.

An axial cross-sectional view through the test specimen cans is shown in Fig. 2.2.5. Although this is a view of the top can (250°C specimen temperature), it is typical of the construction of the other three test cells also. Figure 2.2.6 is a radial cross section of the top test cell. Each test cell will have three Chromel vs Alumel thermocouples inserted in a well, which in turn is immersed in the sodium heat transfer medium of the cell. The primary source of temperature control will be the helium-neon gap between the specimen container wall and the capsule primary containment. The electric heaters (two for each cell) wound around the heater mandrel will be used to fine tune the temperature of each test cell. The stainless steel center spline will serve as the primary gas (He-Ne) supply to the capsule. We are trying to devise a system whereby flux monitors can be inserted into and removed from the center spline while the capsule is in the reactor.

It should be pointed out once again that this is an initial conceptual design and is subject to numerous changes as we work out the thermal analyses, stress analyses, and assembly techniques.

2.2.5 Conclusions and Future Work

The design of the ORR core piece required for the first two irradiation periods and the conceptual design of the experimental capsule have been completed. Final neutronic design calculations will be carried out shortly. Additional calculations are necessary to determine the amount of additional fuel required to increase the dpa by 15%. The cross sections for neutron absorbers such as tantalum and tungsten are difficult to obtain, but should be available in the next several months.

ORNL-DWG 78-21356

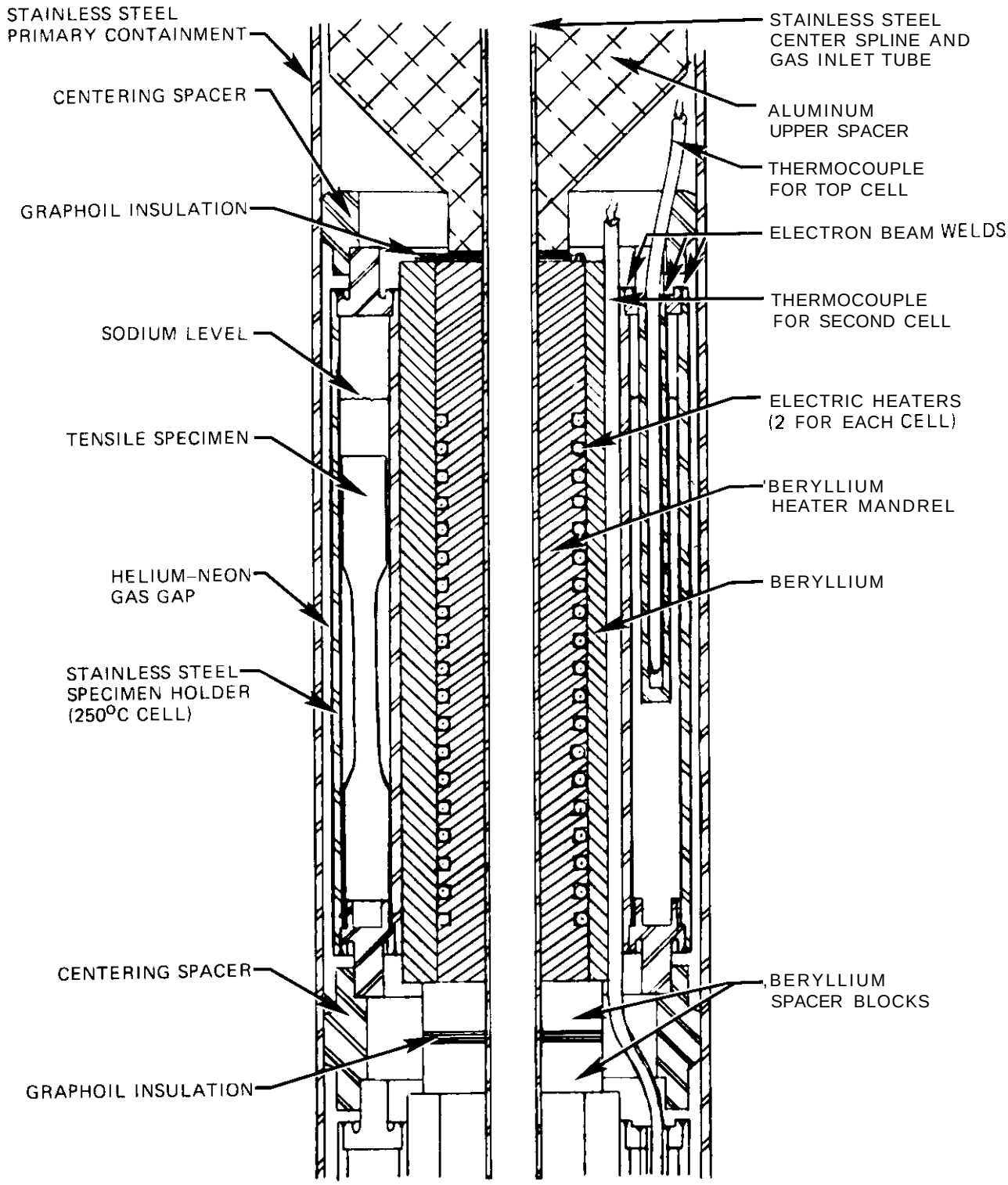

Fig. 2.2.5. Axial Cross Section of Top Test Cell of Proposed Spectrum Tailoring Experiment.

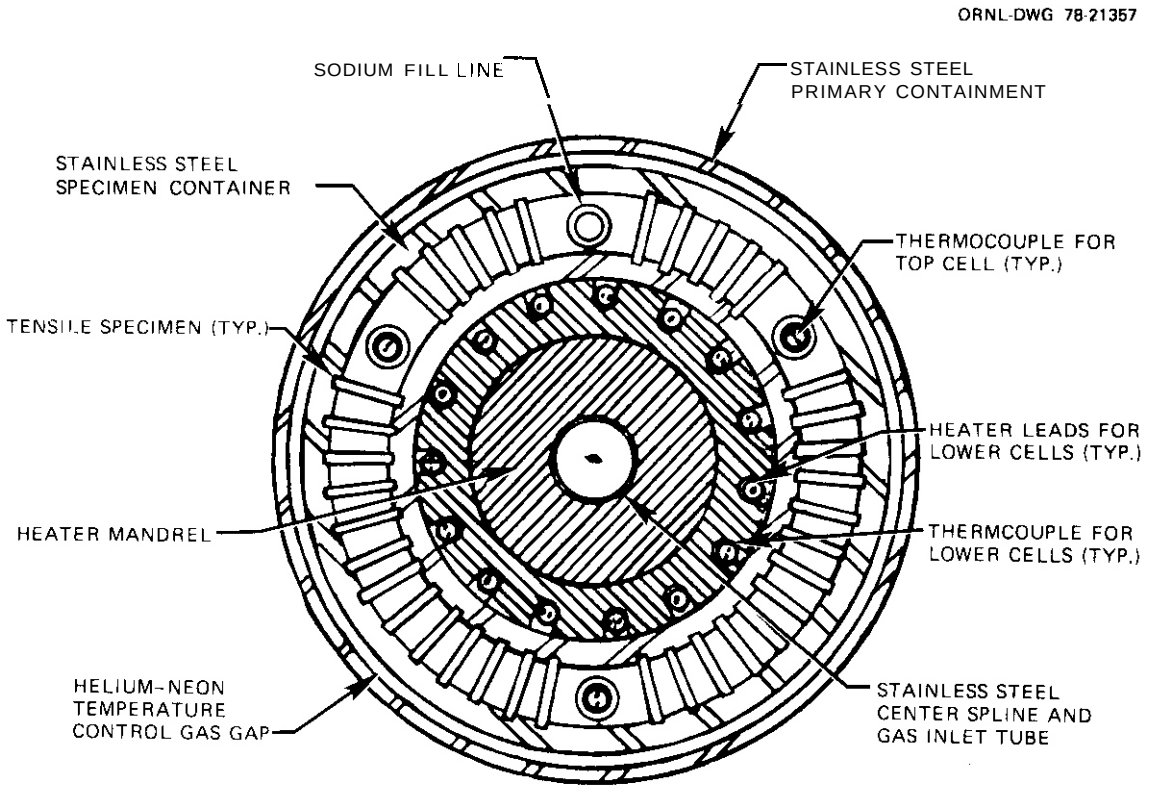

Fig. 2.2.6. Radial Cross Section of Top Cell of Proposed Spectrum Tailoring Experiment.

2.2.6. Reference

1. **D. R. Vondy, T. B. Fowler, and G. W. Cunningham,** *VENTURE, A Code Block for Solving Multigroup Neutron Problems Applying the Finite-Diffusion-Theory Approximations to Neutron Transport,* **ORNL-5062 (October 1975).**

2.3 STATUS OF FATIGUE TESTING FACILITY — K. C. Liu and M. L. Grossbeck (ORNL)

2.3.1 ADIP Task

ADIP Task I.A.2, Define Test Matrices and Test Procedures.

2.3.2 Objective

The objective of this effort is the development and application of an apparatus for use in mechanical testing irradiated specimens by remote operation in a radiation-shielded hot cell. The system is capable of performing a variety of mechanical property experiments in a high vacuum at elevated temperatures under programmed loading histories.

2.3.3 Summary

The fatigue testing system for in-cell testing has been completed and is currently being operated for testing irradiated specimens under cyclic fatigue loading. Excellent performances have been demonstrated for a few initial in-cell tests on two irradiated and two unirradiated 20%-cold-worked type 316 stainless steel specimens at 430°C in high vacuum.

2.3.4 Progress and Status

An electrohydraulic closed-loop controlled fatigue tester capable of testing irradiated specimens at elevated temperatures in high vacuum, described in earlier progress reports, has been completed for in-cell testing and is in commission. The system is complete with a set of special tools specifically developed for remote handling of irradiated specimens and test preparation, including a remotely operated device that calibrates a strain transducer in high vacuum. Among many other features, it includes a diametral extensometer, which measures the diametral strain directly from the minimum gage section of hourglass-shaped fatigue specimens. Cyclic fatigue loadings are controlled by an equivalent axial strain calculated from the diametral strain through a strain computer.

An examination of test results indicates that the testing system is performing at its optimum condition. However, room for further improvements exists, and the effort is continuing. A detailed description of the testing system and its functional features will be presented in a topical report, which is currently in preparation.

Cyclic fatigue tests of 20%-cold-worked type 316 stainless steel irradiated in HFIR have been initiated. Two irradiated specimens were tested at 430°C in a vacuum below 0.1 mPa. These tests were controlled by the axial strain, fully reversed in tension and compression, at ranges of ±0.75 and ±0.5%. A symmetric triangular function beginning with compression was used in all the tests at a strain rate of 0.004/s.

Cold-worked stainless steels under constant strain-controlled cyclic loadings are known to initially exhibit cyclic hardening followed by gradual cyclic softening. To capture cyclic behavioral features of the hysteresis stress-strain relationship, the stress-strain loops were recorded continuously only for a few initial cycles as shown in Figs. 2.3.1 and 2.3.2. Subsequently, they were recorded at intervals as necessary to observe the changes. The stress and strain responses were, however, recorded independently by a strip chart recorder on a continuous time basis. Information not recorded between two hysteresis loops was supplemented by the strip chart. In addition, it provides information to aid in the determination of fatigue crack initiation.

To facilitate comparison, two unirradiated specimens prepared from the same heat of sample material were tested by the same procedure and test conditions as those used for the irradiated specimens. Results of the tests are plotted in Figs. 2.3.1 and 2.3.2. Table 2.3.1 summarizes the results of four cyclic fatigue tests.

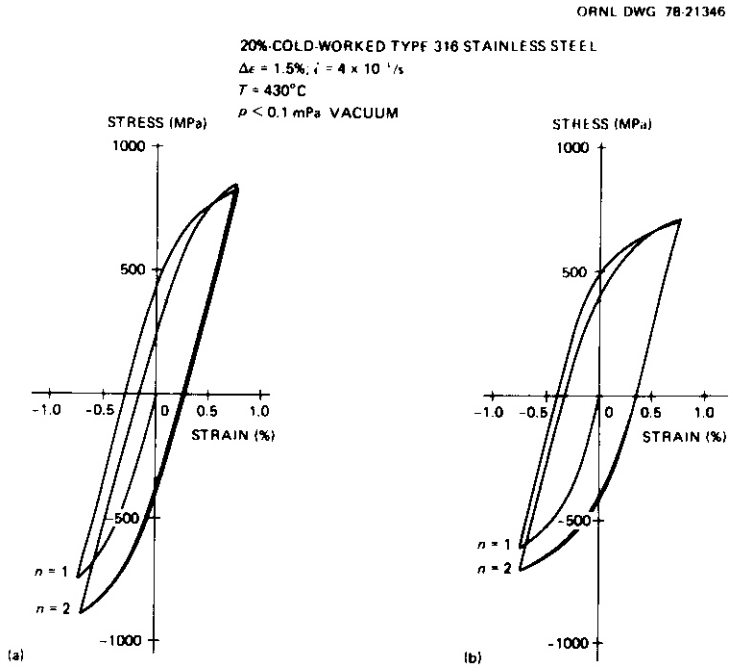

Fig. 2.3.1. Comparison of Cyclic Stress–Strain Behavior Between Irradiated and Unirradiated 20%–Cold–Worked Type 316 Stainless Steel Subjected to Strain–Controlled Cyclic Loadings at a Total Strain Range of 1.5%. (a) Irradiated. (b) Unirradiated.

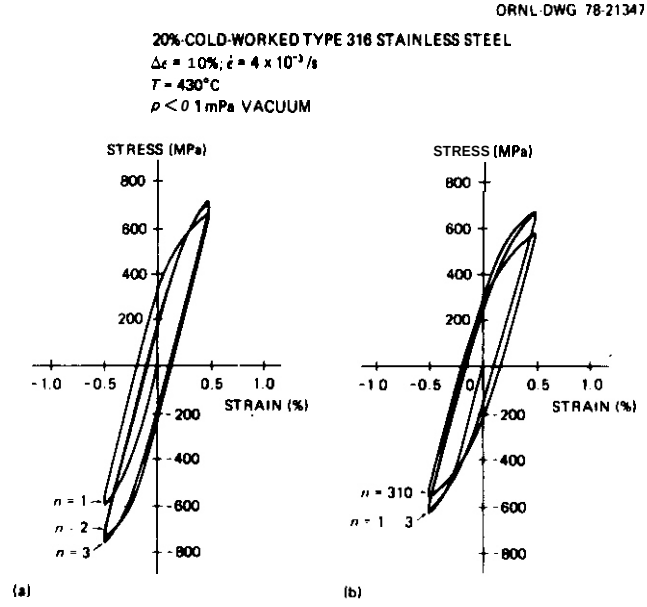

Fig. 2.3.2. Comparison of Cyclic Stress–Strain Behavior Between Irradiated and Unirradiated 20%-Cold-Worked Type 316 Stainless Steel Subjected to Strain–Controlled Cyclic Loadings at a Total Strain Range of 1.0%. (a) Irradiated. (b) Unirradiated.

Table 2.3.1. Cyclic Fatigue Life of 20%-Cold-Worked Type 316 Stainless Steel in Irradiated and Unirradiated Conditions[a]

Specimen Number	Axial Strain Amplitude (%)	Fluence >0.1 MeV (n/m^2)	Number of Cycles to Fracture
A-39	± 0.75	0.9×10^{26}	1,272
A-96	± 0.75	0	2,602
A-23	± 0.5	0.9×10^{26}	1,881
A-68	± 0.5	0	28,740

[a]Nominal specimen diameter 3.18 mm (0.125 in.), strain rate 0.004/s, test temperature 430°C.

2.3.5 Conclusions

No attempt is made here to elaborate a detailed discussion on cyclic fatigue lifetimes of the material tested so far, since the limited number of test data are far from adequate to draw any significant conclusions. However, a brief examination of 'the data appears to indicate that radiation damage reduces the cyclic fatigue life of the material.

No indication of specimen buckling was observed before fracture in complete separation. Excellent performance of the test machine was demonstrated, and it is now in commission.

3. PATH A ALLOY DEVELOPMENT — AUSTENITIC STAINLESS STEELS

Path A Alloys are those alloys generally known as austenitic stainless steels. The most common U.S. designations are AISI types 304, 316, 321, and 347. Primary considerations for selecting this class of alloys for further development are:

1. state-of-the-art production and fabrication technology;
2. extensive data on the effects of neutron irradiation on properties, which show the potential of these alloys for MFR applications;
3. compatibility with proposed coolants and breeding fluids;
4. evidence that for MFR conditions (He, dpa, temperatures) the properties are sensitive to composition and microstructure — thus showing potential for further development.

The strategy for development of these alloys has two related objectives:

1. to determine for a reference alloy the effects of irradiation on those properties most important to fusion reactor design;
2. to develop a path A alloy that is optimized for fusion reactor applications.

The first objective will provide a data base for near-term reactor design and, most important, guidance as to which properties limit performance of this type alloy. Work on the reference alloy will provide direction for the actual alloy development efforts of the second objective. Type 316 stainless steel in the 20%-cold-worked condition appears to be the best choice as a reference alloy. It is the present reference cladding and duct alloy in the breeder reactor programs, and there are extensive data on the unirradiated mechanical properties, effects of heat treatment on properties, structure, and phase stability, and the effects of fast neutron irradiation on properties. The present technology of austenitic stainless steels, including understanding of the physical and mechanical properties and irradiation response, is such that alloy development efforts can move to optimization for use in fusion reactor applications. A Prime Candidate Alloy (PCA) (Fe—16% Ni—14% Cr—2% Mo—2% Mn—0.5% Si—0.2% Ti—0.05% C) has been selected by the ADIP task group. Efforts will now focus on optimizing the composition and microstructure of the PCA leading toward the selection of OPT-A1 (Program Plan designation of first optimized path A alloy).

3.1 TENSILE PROPERTIES OF HFIR-IRRADIATED TYPES 316 AND 316 + 0.23% Ti STAINLESS STEELS — M. L. Grossbeck and P. J. Maziasz (ORNL)

3.1.1 ADIP Task

ADIP Task I.B.13, Tensile Properties of Austenitic Alloys (Path A).

3.1.2 Objectives

This series of experiments is being done to evaluate the strength, ductility, and fracture mechanisms in types 316 and 316 + 0.23% Ti stainless steel irradiated in the High Flux Isotope Reactor (HFIR) to medium fluence and helium levels.

3.1.3 Summary

Miniature tensile specimens of types 316 and 316 + 0.23% Ti (TiM 316) stainless steel in the annealed and 20%-cold-worked conditions were irradiated in HFIR to displacement damage levels of 5–17 dpa and 200–1000 at. ppm He. The specimens were tested near the irradiation temperatures. Reduction of area and true fracture stress were determined, and scanning electron microscope (SEX) fractographs were made to study the fracture mechanisms and the effect of titanium on fracture. Type 316 stainless steel showed an unusual brittle behavior at *450°C*. Associated with this behavior was a cavity structure visible on the fracture surface. The cavities are tentatively believed to be associated with helium.

3.1.4 Progress and Status

In a fusion reactor the first wall will be subject to intense neutron radiation, resulting in displacement damage as well as formation of helium and hydrogen from transmutation reactions. Since type 316 stainless steel is a candidate first-wall material, its strength and ductility and those of a titanium-modified variation were investigated. Irradiations were conducted in the High Flux Isotope Reactor (HFIR), which has an appropriate spectrum to produce both displacement damage and helium through a two-step thermal neutron reaction with nickel contained in the stainless steel.

3.1.4.1 Experimental Description

Miniature tensile specimens were fabricated from types 316 and 316 + 0.23 wt % Ti (TiM 316) stainless steel of the compositions shown in Table 3.1.1. The specimens were irradiated in HFIR in a peripheral target position, where the peak thermal flux is 2.5×10^{19} n/m^2 s and the peak fast flux is 1.3×10^{19} n/m^2 s (>0.1 MeV). The specimen and specimen holder geometry have been reported previously.[1] A gas gap around each specimen restricted radial heat transfer so as to obtain the desired elevated temperature.

Table 3.1.1. Composition of Stainless Steel Investigated

Alloy	Content,[a] wt %										
	Cr	Ni	Mo	Mn	Ti	Si	C	P	S	N	B
316	18.0	13.0	2.58	1.9	0.05	0.8	0.05	0.013	0.016	0.05	0.0005
TiM	17.0	12.0	2.50	0.5	0.23	0.40	0.06	0.01	0.013	0.0055	0.0007

[a] Balance Fe.

All specimen material was initially annealed 1 h at 1150°C. The standard type 316 stainless steel was then swaged to a 50% reduction of area and annealed for 1 h at 1050°C. The cold-worked samples were swaged to a 20% reduction of area, and then tensile specimens were machined. The annealed samples were machined from the material annealed for 1 h at 1050°C and then annealed an additional 15 min at 1050°C to relieve any surface cold work. The type TiM 316 stainless steel was initially annealed for 1 h at 1150°C. The cold-worked material was swaged to a 28% reduction of area, annealed for 1 h at 1050°C, swaged to a 20% reduction of area, and machined into tensile specimens. The annealed material was swaged to 42.4% reduction of area. Tensile specimens were machined, and these were annealed for 1 h at 1050°C.

No instrumentation was installed in the capsule; however, extensive dosimetry has been done in the past, and temperature monitors from more recent irradiations are now being analyzed. Helium levels were calculated from an empirical relation determined by Wiffen et al.[2]

and based on fusion mass spectrographic analysis of HFIR-irradiated specimens. The calculations are believed to have an accuracy of ±25%.

Tensile tests were conducted on a hot-cell-installed Instron machine using a crosshead speed of 0.85 μm/s, resulting in a nominal strain rate of 4.6×10^{-5}/s. Tests were performed in air in a resistance furnace with a 150-mm hot zone to provide temperature uniformity over the center region of 50 mm.

Following imersion density measurements to determine swelling as previously reported,[3] postirradiation tensile tests were performed on specimens irradiated at temperatures in the range from 300 to 600°C. Test temperatures were chosen as 350, 450, and 575°C, and specimens were selected with calculated irradiation temperatures as close to these values as possible. Fluences ranged from 0.63×10^{26} to 2.1×10^{26} n/m^2 (>0.1 MeV) and damage levels from 5 to 17 dpa. Helium contents ranged from 200 to 1000 at. ppm.

Following tensile testing, the specimen buttonhead was removed to minimize the radiation activity level. The portion including the fracture surface was then mounted in a shielded scanning electron microscope (SEM). It was photographed at 30x to obtain a measurement of the fracture surface area. A standard microscope grid was used for magnification calibration for each specimen since the vertical position, and therefore the magnification, varied from one specimen to another. Since the original specimen diameter was known, reduction of area could be calculated.

Load at fracture was known from the tensile testing machine. Therefore, since the area of the fracture surface was determined, true fracture stress could be calculated.

3.1.4.2 Results

Measurements of yield strength and total tensile elongation were reported previously.[1] Therefore, only the results of reduction of area measurements, true fracture stress determinations, and SEM fractography will be reported.

Figure 3.1.1 shows reduction of area as a function of fluence for 350, 450, and 575°C. Both alloys in the 20%-cold-worked condition show

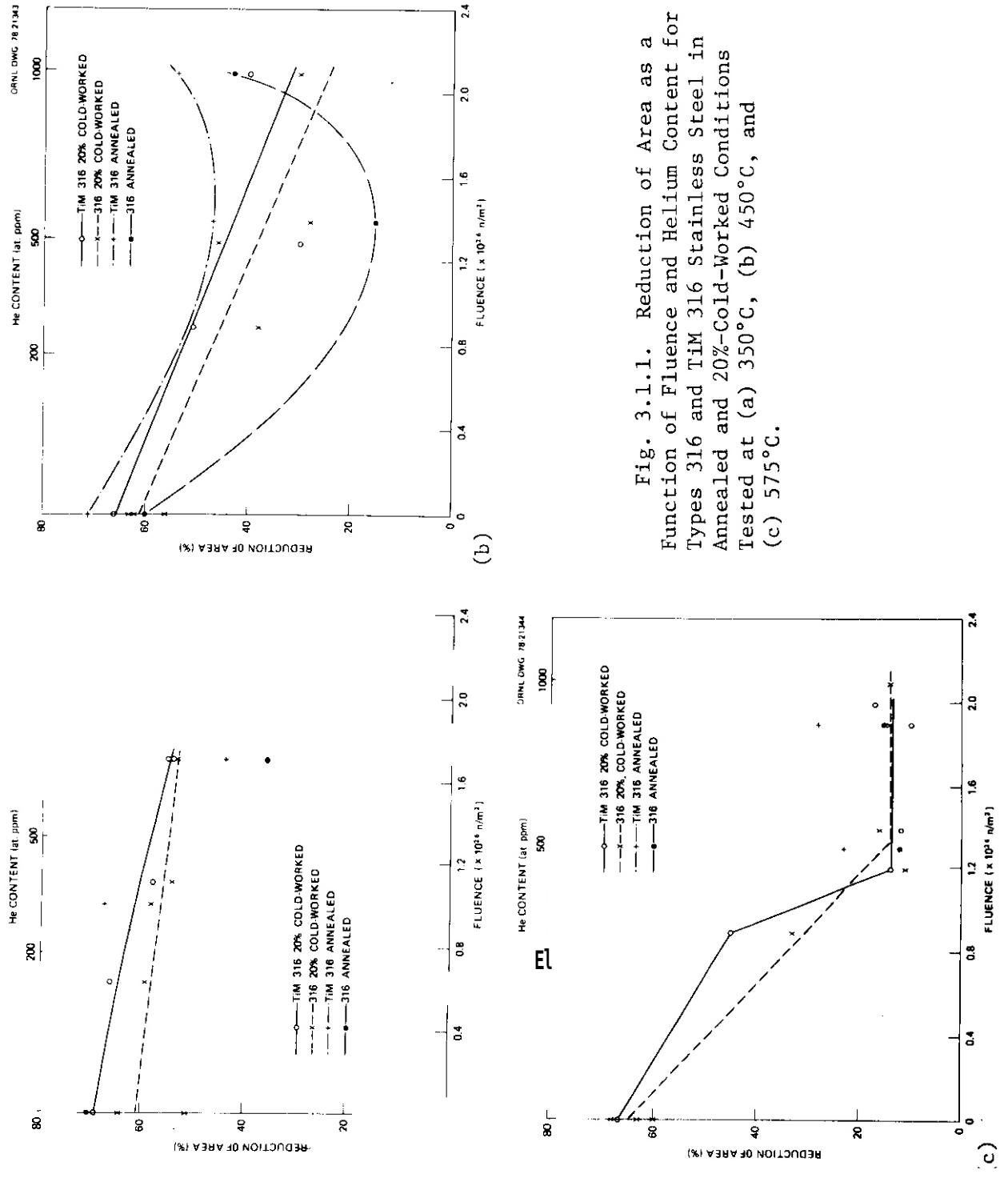

Fig. 3.1.1. Reduction of Area as a Function of Fluence and Helium Content for Types 316 and TiM 316 Stainless Steel in Annealed and 20%-Cold-Worked Conditions Tested at (a) 350°C, (b) 450°C, and (c) 575°C.

only a slight decrease in ductility at 350°C and a more pronounced drop at 450°C. At 575°C, the drop in ductility is comparatively rapid, reaching a constant value through the range of 1.2 to 2.1×10^{26} n/m^2. For the annealed condition, data are very sparse, but ductility tended to pass through a minimum at 450°C and perhaps even at 575°C. However, more data are necessary before any conclusions on this can be reached. It is important to note that ductility as measured by reduction of area remains at or above 10% for both alloys at all temperatures examined below 2.1×10^{26} n/m^2 and that ductility appears to saturate at this value for these low fluences.

Figure 3.1.2 shows true fracture stress as a function of fluence. At 350°C, strengthening appears to be followed by reduction in strength for both cold-worked alloys. At both 450 and 575°C, reduction in strength is followed by appparent saturation for the cold-worked material and perhaps an increase in fracture strength of the annealed material.

3.1.4.3 Discussion

The reduction of area curves for the cold-worked alloys in Fig. 3.1.1 have been replotted separately with the addition of SEM fractographs. These sets of fractographs suggest some of the failure mechanisms and will be used as a guide in determining areas for further study.

In the 20%-cold-worked type 316 stainless steel at 350°C, the fractographs in Fig. 3.1.3 support the reduction of area data, which demonstrate a slow decrease in ductility with increasing fluence. Extreme ductile tearing and microvoid coalescence evident in the unirradiated sample evolve into a rather fine-scale simple rupture. Additionally, the fracture surface appears to have some cavities that are not associated with ductile rupture and are not surrounded by cup-type deformation.

At 450°C (Fig. 3.1.4), the reduction in ductility and fracture stress is accompanied by a transition in fracture mechanism. At a fluence of 1.3×10^{26} n/m^2, the fracture surface clearly exhibits

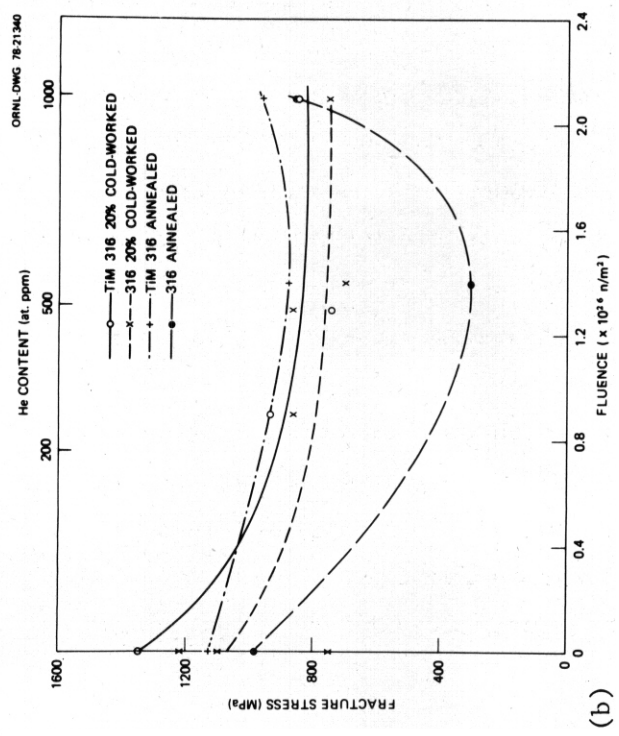

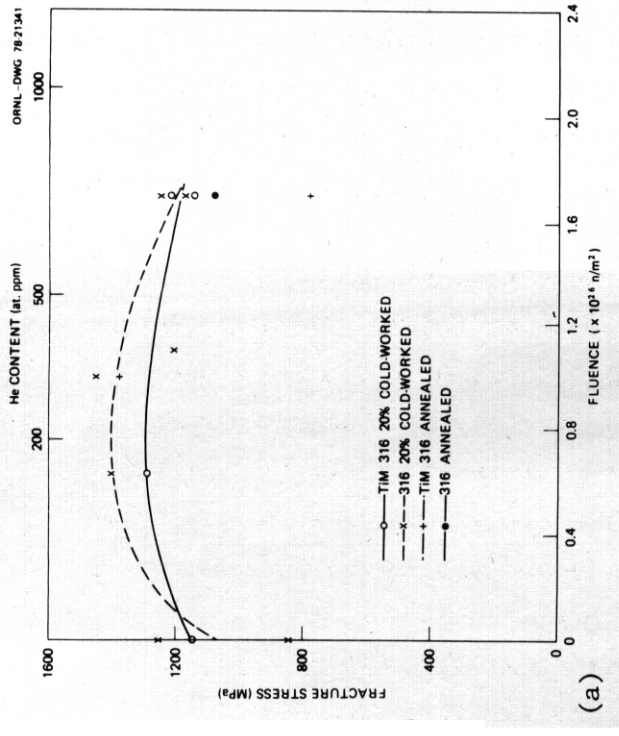

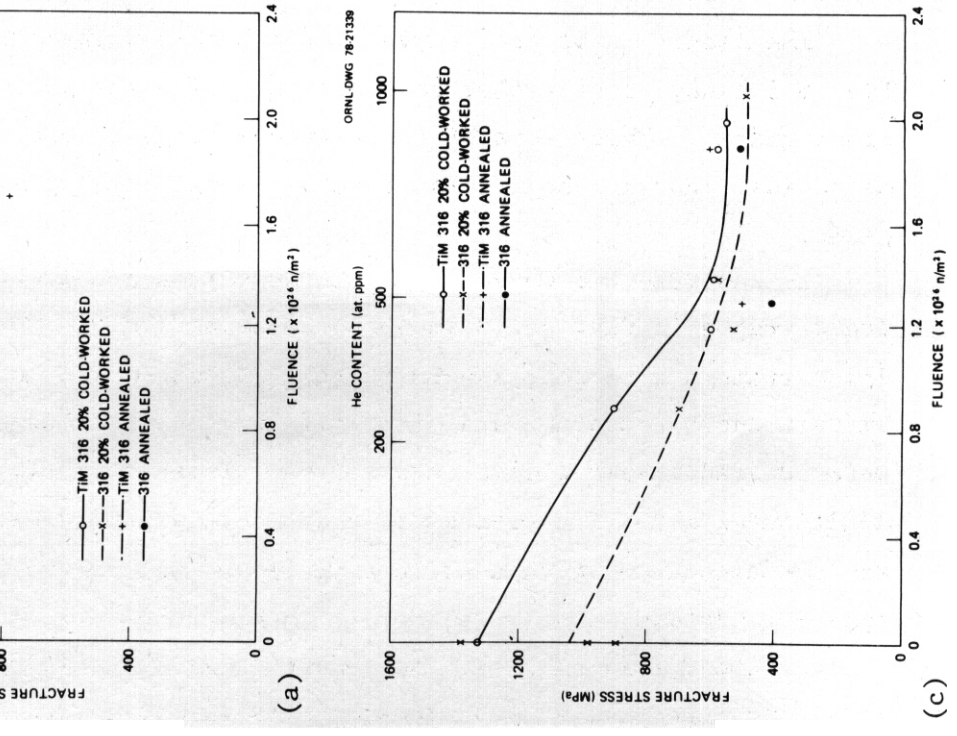

Fig. 3.1.2. True Fracture Stress as a Function of Fluence and Helium Content for Types 316 and TiM 316 Stainless Steel in Annealed and 20%-Cold-Worked Conditions Tested at (a) 350°C, (b) 450°C, and (c) 575°C.

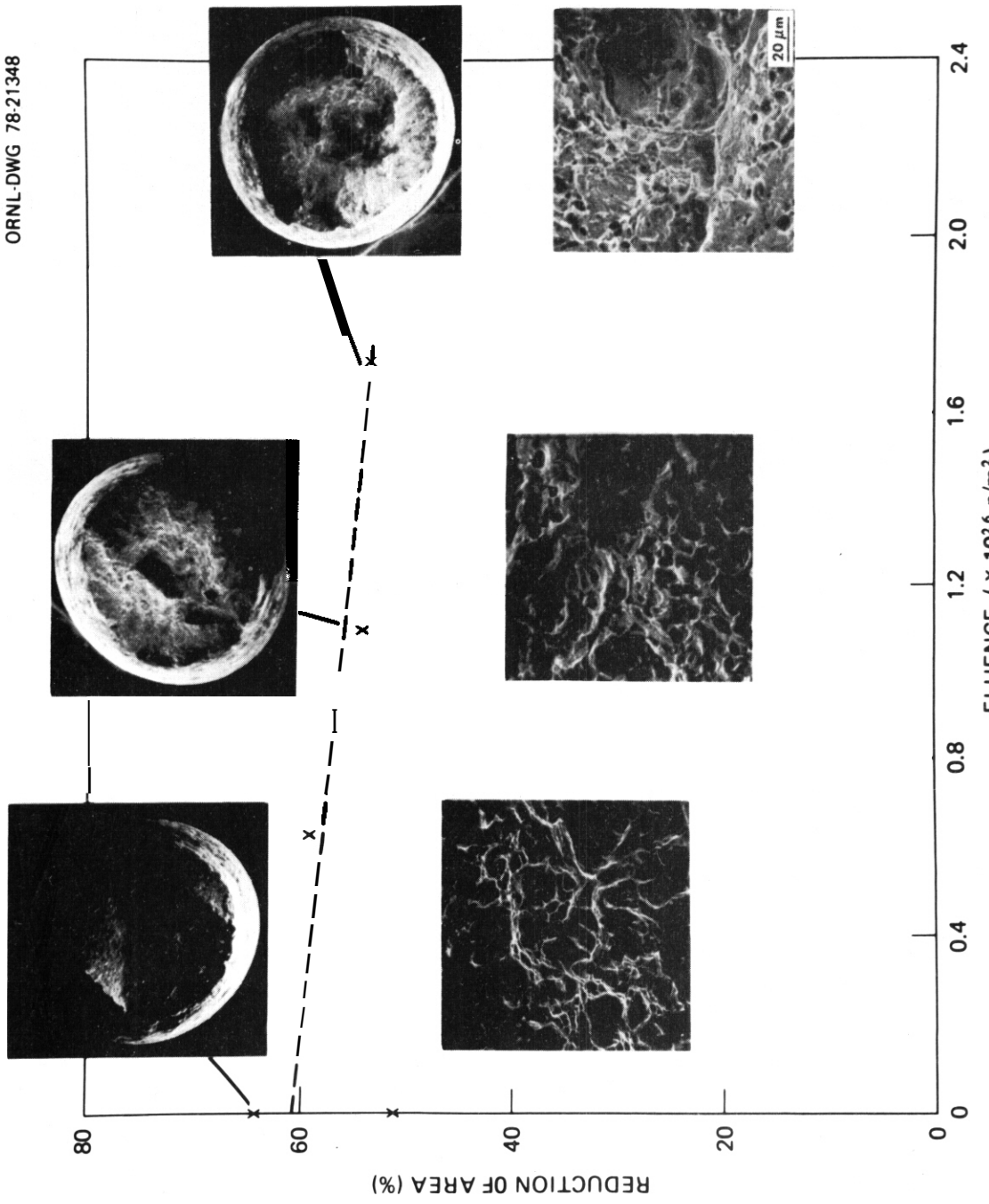

Fig. 3.1.3. Reduction of Area as a Function of Fluence Showing Fracture Surface Morphology for 20%-Cold-Worked Type 316 Stainless Steel Tested at 350°C.

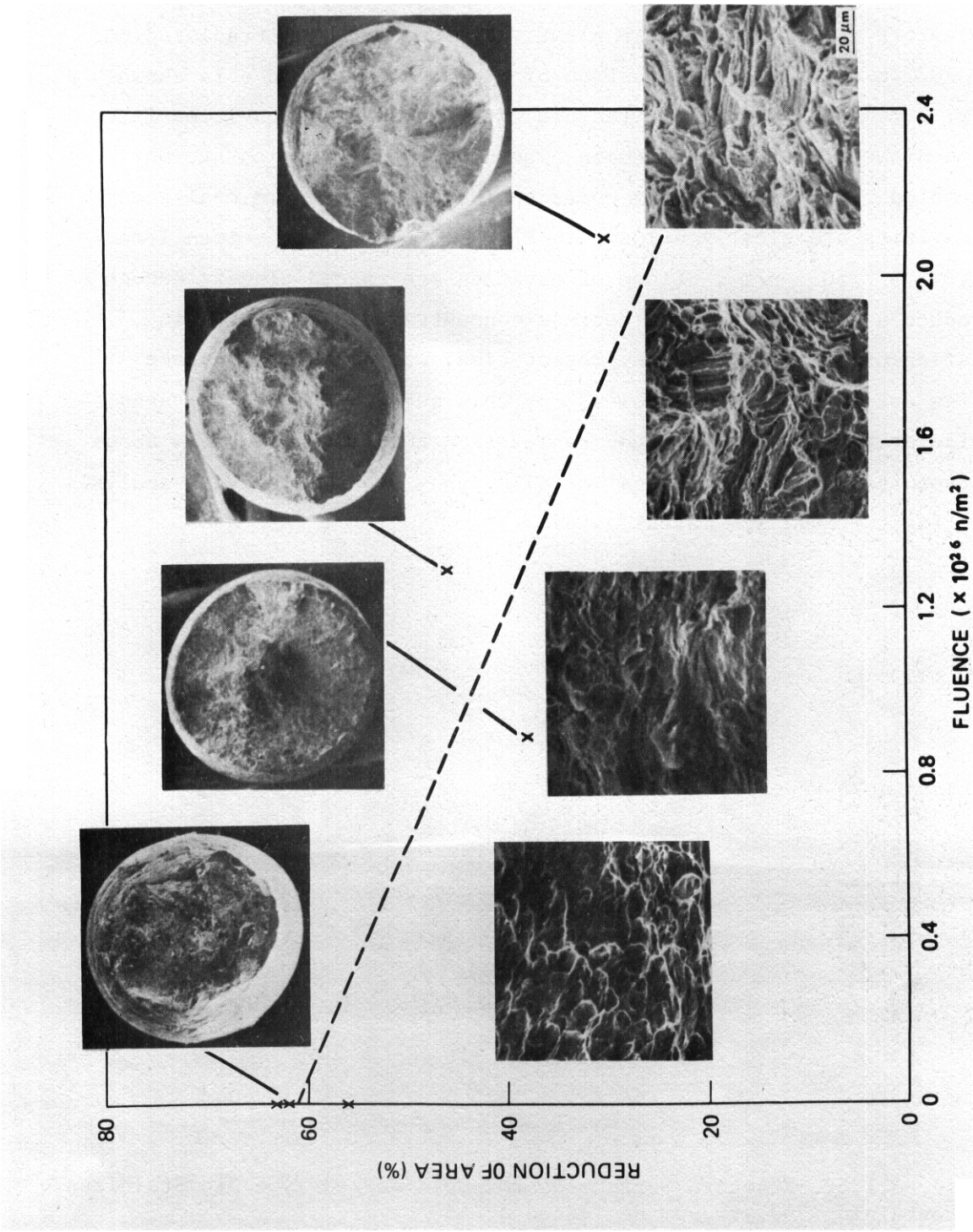

Fig. 3.1.4. Reduction of Area as a Function of Fluence Showing Fracture Surface Morphology for 20%-Cold-Worked Type 316 Stainless Steel Tested at 450°C.

areas of flat plates reminiscent of cleavage or even channel fracture.[4,5] However, although the fracture is platelike and apparently crystallographic, river lines characteristic of cleavage are absent. The steplike feature is shown even more clearly in the specimen irradiated to 1.4×10^{26} n/m^2, of which a portion of the fracture surface is shown in Fig. 3.1.5. This type of fracture is accompanied by cavities 1 to 2 μm in diameter, similar to those observed at 350°C, which are not accompanied by cuplike tearing characteristic of microvoid coalescence. Such cavities are clearly evident in Fig. 3.1.6 of the specimen irradiated to 1.3×10^{26} n/m^2. Lines of cavities are spaced closely enough to produce a significant local stress concentration, resulting in initiation of a crack. At the present time, we suggest that these cavities are large helium bubbles, but this suggestion is being used to guide areas for further study rather than to draw conclusions about the fracture mechanism. Optical metallography and residual gas analysis during fracture will be investigated.

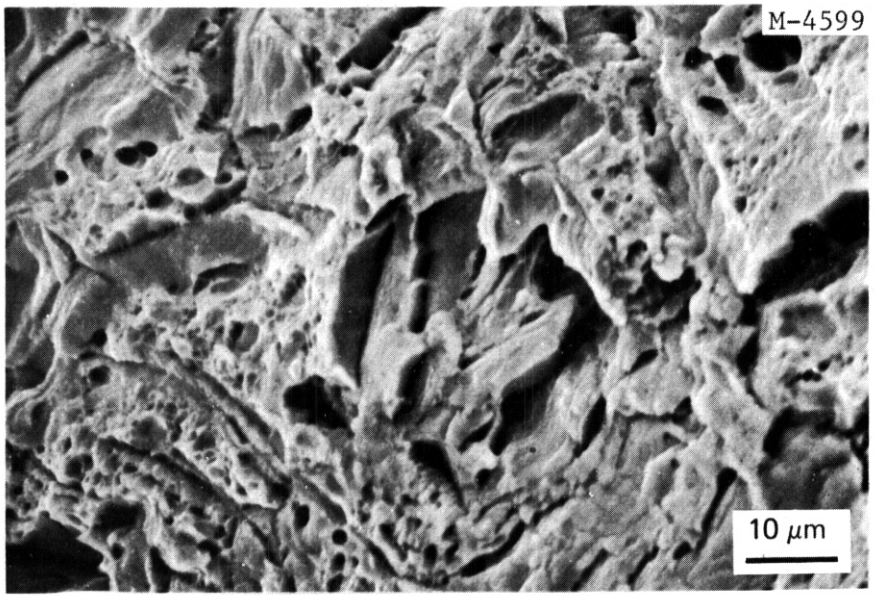

32

Fig. 3.1.5. Fracture Surface of 20%-Cold-Worked Type 316 Stainless Steel Containing 500 at. ppm He Tested at 450°C.

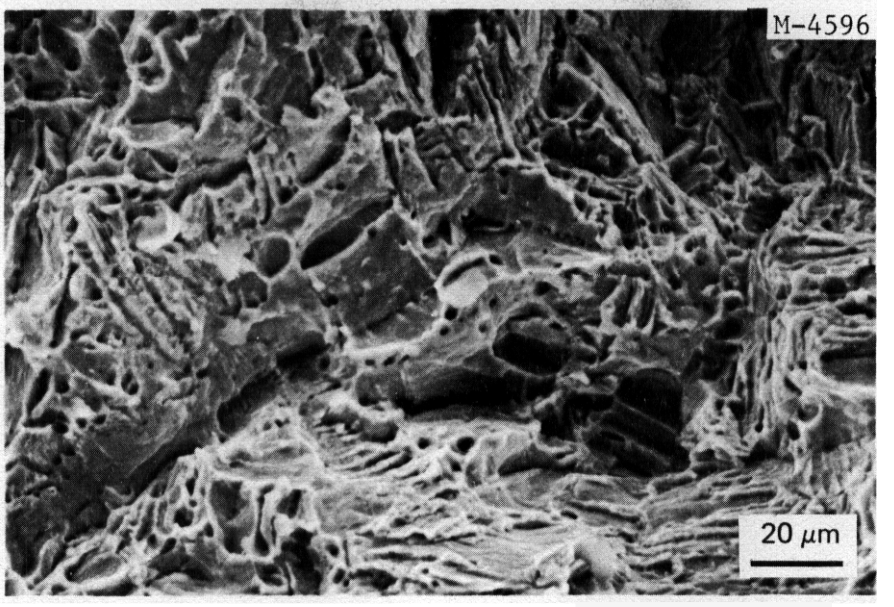

Fig. 3.1.6. Fracture Surface of 20%-Cold-Worked Type 316 Stainless Steel Containing 500 at. ppm He Tested at 450°C, Showing Cavities.

At 575°C, intergranular fracture begins to appear, as shown in Fig. 3.1.7. There is evidence of a dense concentration of cavities in a small area of the specimen irradiated to 1.4×10^{26} n/m^2. We do not know if the particular face showing the cavities is a grain boundary or a transgranular fracture plane. At 2.1×10^{26} n/m^2, the fracture surface begins to exhibit characteristics of the specimens fractured at 450°C.

The 20%-cold-worked type TIM 316 stainless steel shows a higher f'raction of ductile rupture at 350 and 450°C (Figs. 3.1.8 and 3.1.9). The dimple rupture pattern becomes finer as fluence increases, perhaps because the voids causing the fracture originate as finely spaced helium bubbles at the high fluences. The phenomenon could also result from irradiation strengthening in the type TiM 316 stainless steel. At 450°C, there is no evidence of facets on the fracture surface, but there is clear evidence of coalescence of small cavities in the absence of cup-type ductile rupture.

The specimens fractured at 575°C (Fig. 3.1.10) exhibit intergranular fracture similar to type 316 stainless steel except that

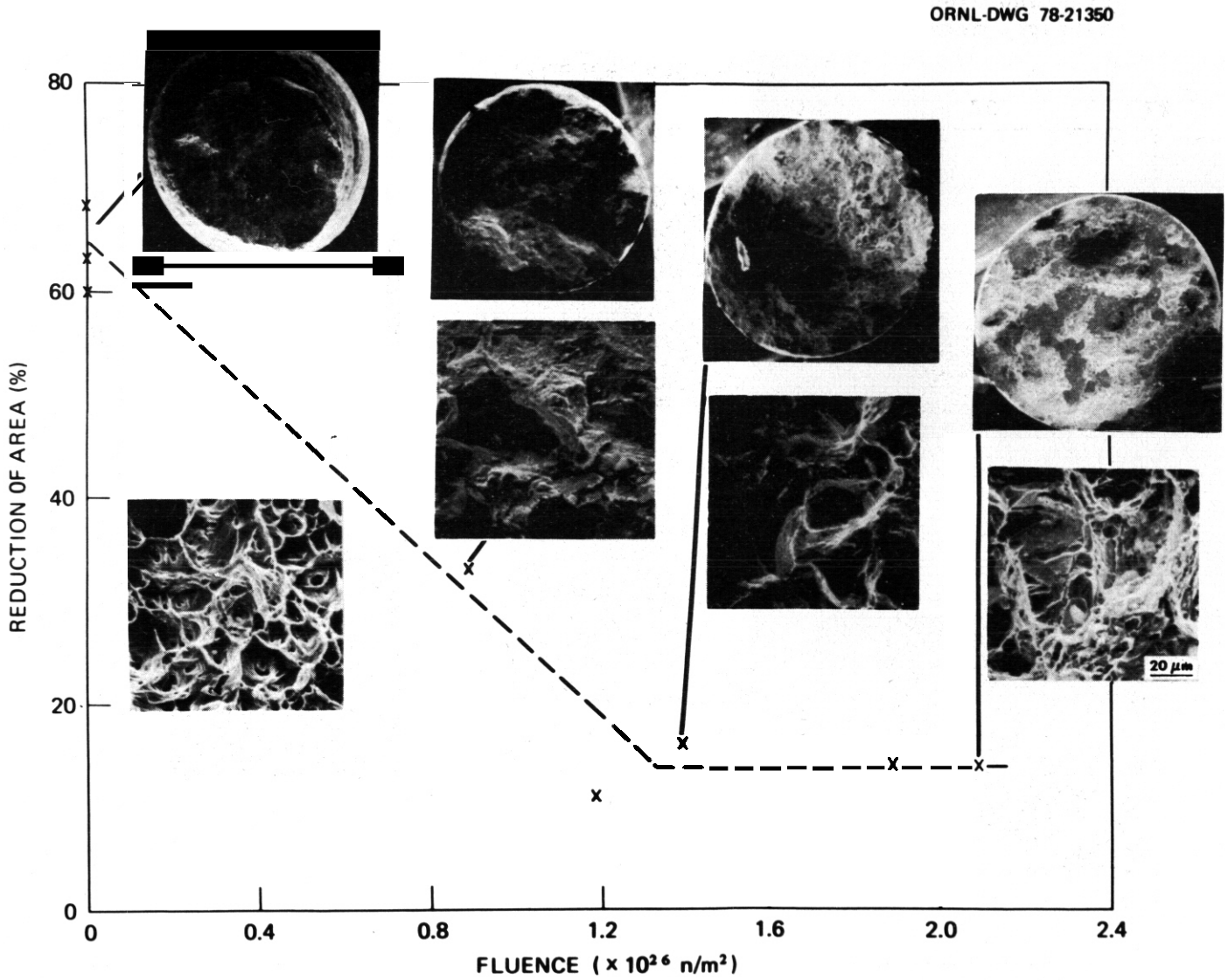

Fig. 3.1.7. Reduction of Area as a Function of Fluence Showing Fracture Surface Morphology for 20%-Cold-Worked Type 316 Stainless Steel Tested at 575°C.

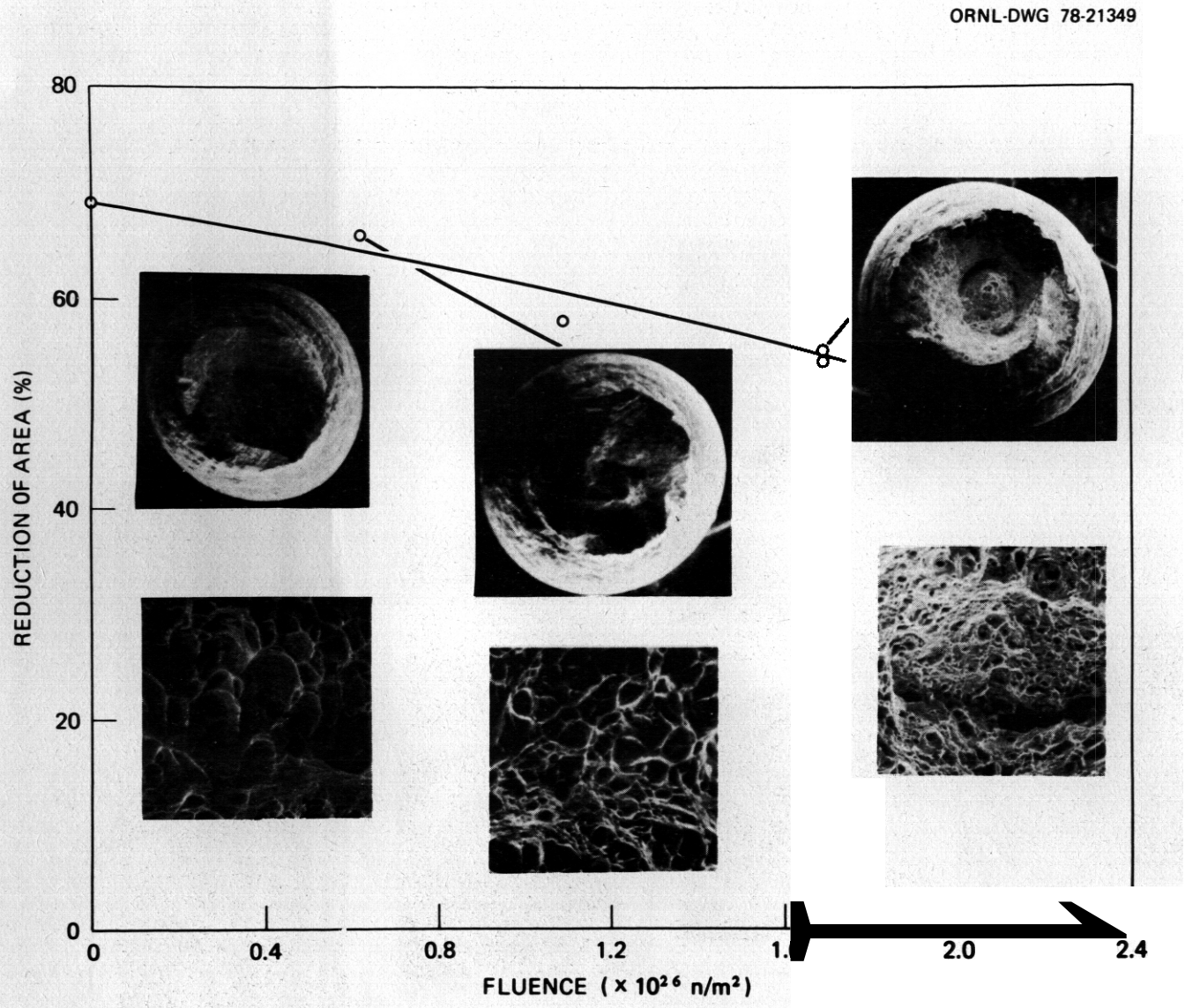

Fig. 3.1.8. Reduction of Area as a Function of Fluence Showing Fracture Surface Morphology for 20%-Cold-Worked Type TiM 316 Stainless Steel Tested at 350 C

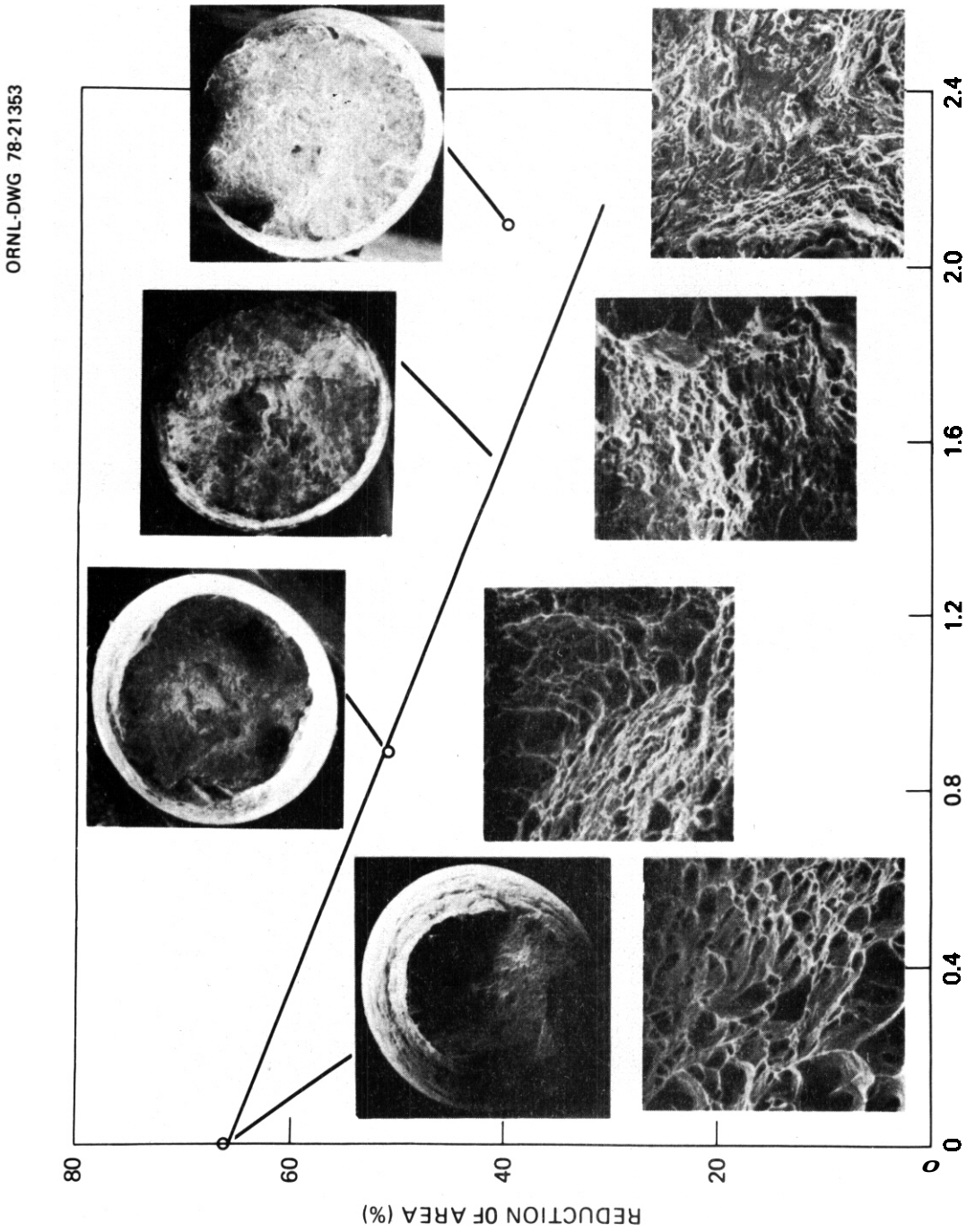

Fig. 3.1.9. Reduction of Area as a Function of Fluence Showing Fracture Surface Morphology for 20%-Cold-Worked Type TiM 316 Stainless Steel Tested at 450°C

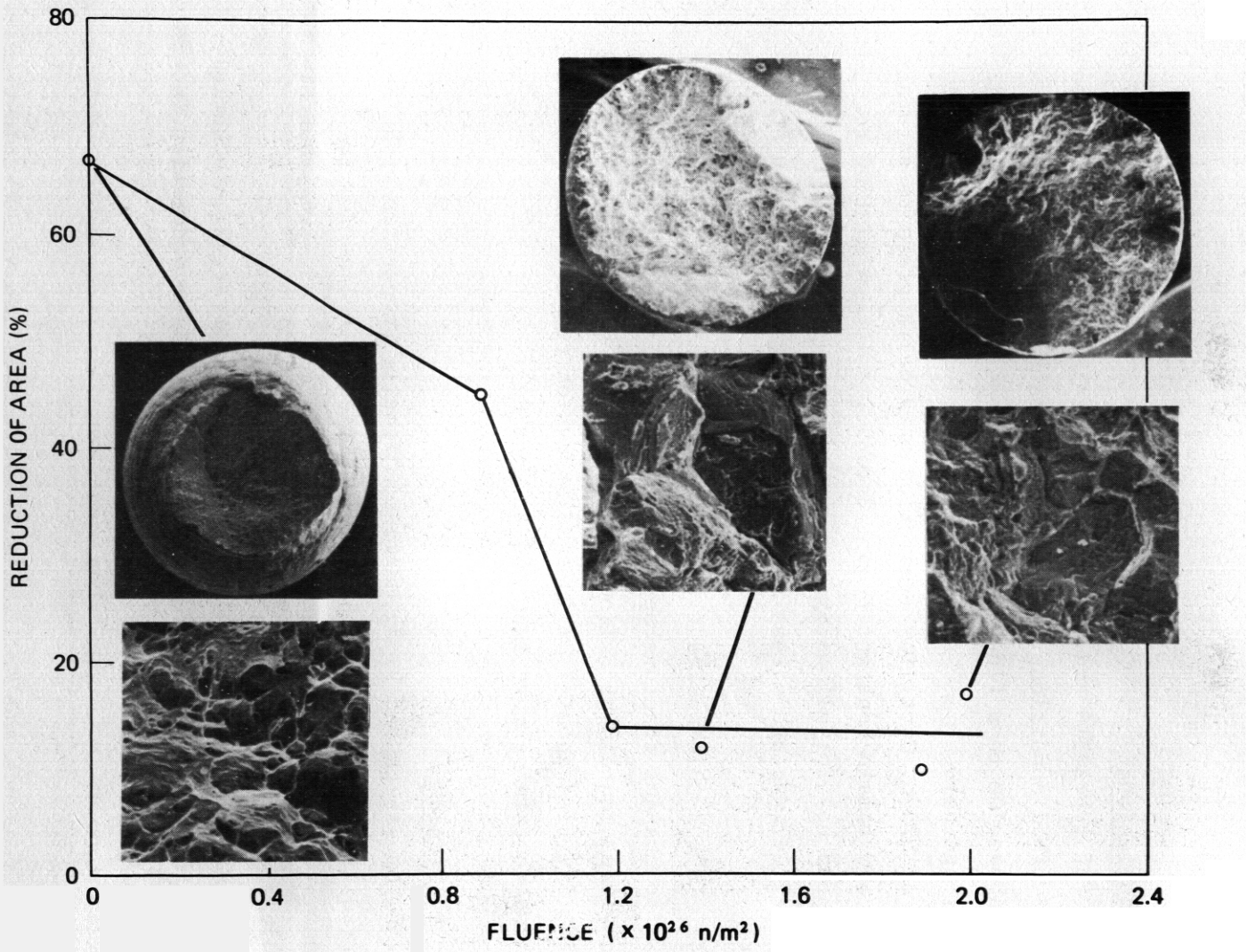

Fig. 3.1 Reduction of Area as a Function of Fluence Showing Fracture Surface Morphology for 20%-Cold-Worked Type TiM 316 Stainless Steel Tested at 575°C.

platelike particles are on the surfaces of some of the samples. These particles could be oxides formed after rupture of the specimen, and their nature will be investigated.

3.1.5 Conclusions

1. For types 316 and 316 + 0.23% Ti stainless steels in annealed and cold-worked conditions, ductility as measured by reduction of area remains above 10% to a fluence level of 2.1×10^{26} n/m^2 (>0.1 MeV) (1000 at. ppm He).

2. At 575°C, ductility (reduction of area) appears to saturate near 10% and remain constant from 1.2 to 2.1×10^{26} n/m^2 (500 to 1000 at. ppm He) for all materials tested.

3. True fracture stress appears to saturate at 1.2×10^{26} n/m^2 at 575°C.

4. In 20%-cold-worked type 316 stainless steel, a mechanism similar to channel fracture appears at 450°C. It may be associated with cavities containing helium.

5. Cavities about 1 μm in size appear on the fracture surface in specimens containing more than 500 at. ppm He.

3.1.6 References

1. M. L. Grossbeck and P. J. Maziasz, "Tensile Properties of HFIR-Irradiated Types 316 and TiM 316 Stainless Steel at 200 to 1000 at. ppm He," *ADIP Quart. Prog. Rep. Sept. 30, 1978,* DOE/ET-0058/3, pp. 32-49.

2. F. W. Wiffen, E. J. Allen, E. E. Bloom, H. Farrar, T. A. Gabriel, A. T. Kerr, and F. G. Perey, "The Rate of Helium Generation in HFIR Irradiation of Nickel," *Magnetic Fusion Energy Materials Technology Program Annu. Frog. Rep. June 30, 1977,* ORNL-5323, pp. 42-43.

3. M. L. Grossbeck and P. J. Maziasz, "The Swelling of 20%-Cold-Worked Type 316 Stainless Steel Irradiated in HFIR to Helium Levels of 200-3700 at. ppm," *ADIP Quart. Prog. Rep. March 31, 1978,* DOE/ET-0058/1, pp. 82-85.

4. C. W. Hunter, R. L. Fish, and J. J. Holmes, "Channel Fracture in Irradiated EBR-II Type *304* Stainless Steel," *Trans. Am. Nucl. Soc.* 15: *254* (1972).

5. R. L. Fish and C. W. Hunter, "Tensile Properties of Fast Reactor Irradiated Type *304* Stainless Steel," p. 119 *in Irradiation Effects on the Microstructure and Properties of Metals, ASTM Spec. Tech. Publ.* 611, American Society for Testing and Materials, Philadelphia, 1976.

3.2 STATUS OF PATH A PRIME CANDIDATE ALLOY PROCUREMENT AND FABRICATION — T. K. Roche (ORNL)

3.2.1 ADIP Task

ADIP Task I.D.1, Materials Stockpile for MFE Programs.

3.2.2 Objectives

The objective of this work is to procure a sufficient quantity of the Path A Prime Candidate Alloy (PCA) to provide for future program needs (i.e., remelt stock for composition variations as well as product forms that allow for further fabrication and microstructure control).

3.2.3 Summary

A 1.4-Mg heat of Fe–16 Ni–14 Cr–2 Mo–0.3 Ti–2 Mn–0.5 Si–0.05 C (wt %) was double vacuum melted. So far 420 kg of 100-mm bar has been received and smaller bar and 13-mm plate have been rolled.

3.2.4 Progress and Status

Teledyne Allvac has produced a 1.4-Mg (3000-lb) heat of Path A Prime Candidate Alloy of the following nominal composition (wt %): Fe–16 Ni–14 Cr-2 Mo–0.3 Ti–2 Mn–0.5 Si–0.05 C. The alloy was made by a double vacuum melting process, vacuum induction melt (VIM), followed by a consumable electrode vacuum arc remelt (VAR), from virgin materials. The 0.30-m-diam (12-in.) VAR ingot was hot rolled to a 0.13-m (5-in.) round-cornered square, then annealed 1 h at 1038°C (1900°F). Finish hot rolling was carried out to provide 13-mm-thick (1/2-in.) plate, 13-mm-diam (1/2-in.) bar, 33-mm-diam (1 5/16-in.) bar, and 100-mm-diam (4-in.) bar. All hot-working was performed in the temperature range 927 to 1150°C (1700–2100°F), and all products received a final anneal at 1050°C (1922°F). The bar products were centerless ground to size. To date, 420 kg (920 lb) of 100-mm-diam bar has been received from the vendor. The other products will be shipped after ultrasonic inspection.

4. PATH B ALLOY DEVELOPMENT — HIGHER STRENGTH Fe-Ni-Cr ALLOYS

Path B alloys are the Fe-Ni-Cr "superalloys" in which tensile, creep-rupture, and fatigue strength levels higher than attainable in the austenitic stainless steels are achieved by precipitation of one or more phases. Many alloys in this class exhibit low swelling in fast-reactor irradiations. The technology for use of path B alloys in neutron radiation environments is not as advanced as for path A alloys. A basis to select a specific alloy type for further development is lacking. Accordingly, the ADIP task group has selected five base research alloys that are representative of the basic systems of path B alloys and deserve consideration for fusion reactor applications. The systems under investigation include γ' strengthened-molybdenum modified, γ' strengthened-niobium-modified, $\gamma'\gamma''$ strengthened, and a high-nickel precipitation-strengthened alloy (2.75% Ni).

Near-term activities are focused on evaluating the effects of a fusion reactor neutron spectrum on key mechanical and physical properties. Damage created by the fusion reactor neutron spectrum is approximated by fission reactor irradiation. Data are presently being obtained on a limited number of commercial alloys on which scoping studies were initiated two to three years ago. The emphasis will shift to base research alloys as they become available. For those properties that are either inadequate or degraded to an unacceptable level, the influence of composition and microstructure on the response will be examined. The research program will be oriented toward determination of mechanisms responsible for the observed property changes and the effects of metallurgical variables on the response. The objective is to develop a basis for selection of the path B prime candidate alloy(s).

4.1 THE SWELLING OF NIMONIC PE-16 IRRADIATED IN HFIR — F. W. Wiffen (ORNL)

4.1.1 ADIP Task

ADIP Task I.C.3, Microstructures and Swelling in High Strength High Temperature Fe-Ni-Cr Alloys.

4.1.2 Objectives

Nimonic PE-16 was chosen as a representative precipitation-strengthened Path B alloy for investigation of the effect of HFIR irradiation on physical and mechanical properties. The swelling resistance of this alloy under neutron irradiation and ion bombardment has been demonstrated in a number of experiments where high displacement levels but low helium contents were produced. The HFIR experiments were initiated to investigate the response to irradiation producing helium levels more representative of fusion reactor service simultaneously with production of displacement damage. Specimens irradiated at temperatures between 55 and 700°C are being examined to determine swelling, microstructural changes, tensile properties, and fracture mode. Experiments in this series have been irradiated to neutron fluences producing 2 to 28 dpa and helium contents of 120 to 5700 at. ppm.

4.1.3 Summary

Tensile-swelling samples of Nimonic PE-16 in the solution treated and aged condition were irradiated in HFIR at design temperatures between 300 and 700°C to fluences in the range 2.2 to 3.7 × 10^{26} n/m^2 (>0.1 MeV). This fluence produced 17 to 28 dpa and helium contents of 3480 to 5700 at. ppm. The resulting swelling, determined by immersion density measurement, ranged from 0.27 to 2.9%. It increased monotonically with increasing irradiation temperature. The swelling data are not consistent with trends deduced from lower fluence irradiations, and detailed microscopy is planned to resolve the conflicting behavior.

4.1.4 Progress and Status

4.1.4.1 Experiments and Relevance to Fusion

This is a continuation of reporting on this series of experiments initiated in the previous quarterly report.' The samples of PE-16 examined for this report had been irradiated in the peripheral target position (PTP) of the HFIR for 375 equivalent full-power days.

Details of this series of experiments were given previously.[1] Experiment HFIR-CTR-18 included five tensile-swelling samples of PE-16, with the solution treated and aged microstructure, at design irradiation temperatures from 300 to 700°C.

Some uncertainty now exists in the absolute value of the nuclear heating rate in the HFIR-PTP experimental location. Some evidence indicates that this heating rate is higher than previously reported, and that in consequence the actual irradiation temperatures are higher than the reported design temperatures. Work is currently under way to resolve this question. In the interim, irradiation temperatures reported are the original design temperatures.

Irradiation for just over one year produced displacement levels of 17.5 to 27.6 dpa and helium of 3480 to 5700 at. ppm. Helium contents were calculated from the equation developed' to correlate experimentally measured values of helium production from the reaction sequence

$$^{58}\mathrm{Ni} + n \rightarrow {}^{59}\mathrm{Ni} + \gamma \ ,$$

$$^{58}\mathrm{Ni} + n \rightarrow {}^{56}\mathrm{Fe} + \alpha \ .$$

These values were further normalized to two measured values on specimens from this experiment.

Reported swelling values were determined by immersion density measurements. Postirradiation length measurements also gave an approximate measure of the swelling. Densities were measured in ethyl phthalate, with the temperature controlled to ±0.05°C. The

liquid density was calibrated against a quartz standard, and density differences were computed relative to a control sample measured in the same series of weighings.

The relationship between the irradiation parameters achieved in these experiments and fusion reactor operation is given in Table 4.1.1. The equivalence is given for fusion service time to produce the displacement level and to produce the helium level for several of the HFIR irradiation conditions.

Table 4.1.1. The Correspondence Between HFIR Irradiation Parameters and Fusion Reactor Service for Nimonic PE-16

Parameters of HFIR Experiments			Fusion Reactor Service to Achieve Same Parameters, MWyr/m^2	
Displacement Level (dpa)	Helium Content (at. ppm)	Ratio,[a] (at. ppm He/dpa)	dpa Level	Helium Level
17.5	3480	199	1.5	14.5
27.6	5700	207	2.4	23.8

[a]This ratio is 20.5 for a tokamak fusion reactor with a lithium blanket and a first wall of PE-16. Operation for 1 MWyr/m^2 produces 12 dpa and 240 at. ppm He.

4.1.4.2 Results

The swelling results on the five high-helium-content specimens are given in Table 4.1.2 with their irradiation conditions. The swelling data are also plotted in Fig. 4.1.1. The swelling values from length measurement were approximately consistent with the density results. Only the more accurate density data are reported here.

The swelling measured in these specimens is lower than would be predicted by extrapolation of the previously reported lower fluence results. In fact, the swelling measured after irradiation at 300, 400, and 500°C was lower than measured in the lower fluence experiments. At 600 and 700°C the swelling did exceed the values found in the previous experiments.

Table 4.1.2. Swelling in Nimonic PE-16[a] Irradiated in HFIR

Irradiation Conditions				Density Decrease (%)
Temperature (°C)	Fluence >0.1 MeV (n/m^2)	Displacement Level	Helium Content (at. ppm)	
300	2.23×10^{26}	17.5	3480	0.27
400	2.36	17.7	3540	0.49
500	2.94	23.2	4660	0.92
600	3.14	23.1	4650	1.49
700	3.69	27.6	5700	2.90

[a]All material heat-treated 4 h at 1080°C plus 16 h at 700°C before irradiation.

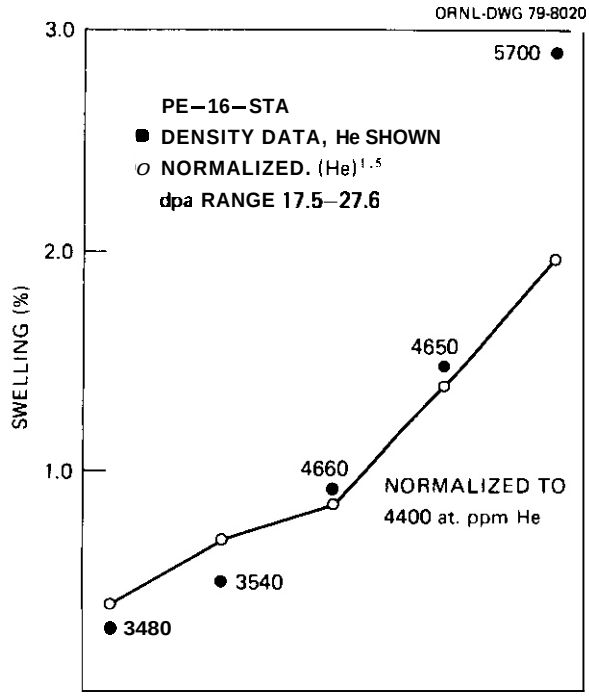

The swelling data were normalized to the mean helium content of this data set to better evaluate the temperature dependence of the swelling. The normalization was accomplished by making three assumptions: (1) that the concentration of cavities would be constant at each temperature over the range of helium of concern, (2) that swelling is controlled by ideal gas behavior of helium-filled equilibrium bubbles, and (3) that there is no incubation stage. Within these assumptions, swelling is proportional to helium content to the 1.5 power.

The swelling data normalized in this manner shows a constantly increasing swelling with increasing temperature in the range 300 to 700°C. At this helium content, 4400 at. ppm, there are no local swelling maxima in this temperature range. The normalized data are also plotted in Fig. 4.1.1.

The temperature dependence of swelling deduced from these data is quite different from the results reported previously[1] for lower helium levels. The local maximum at 500°C for about 2400 at. ppm He was not reproduced by the higher fluence data, and in fact at all temperatures below about 560°C the swelling at 4400 at. ppm He was less than that reported for 2400 at. ppm He, for the solution treated and aged material condition.

4.1.4.3 Comparison of PE-16 with Other Alloys

When comparison is made on the basis of helium content, Nimonic PE-16 continues to be more resistant to swelling than either alloy 600 or type 316 stainless steel. The most recent results show a temperature dependence more similar to that observed[3] in alloy 600 and type 316 stainless steel than reported previously,[1] but the swelling at 700°C is still not a "breakaway" compared with the results at lower temperatures.

4.1.5 Conclusions and Future Work

The available results on swelling of Nimonic PE-16 irradiated in HFIR in the temperature range 55 to 700°C show that the swelling must depend strongly on one or more material or irradiation variables. The

density data do not allow identification of the dominant variable responsible for the conflicting trends deduced from'the data at different helium contents.

Microstructural characterization of these specimens is planned to help establish the mechanism controlling .,welling, to sort out the dependence of swelling in material and irradiation variables, and to guide future modification of alloys similar to Nimonic PE-16.

4.1.6 References

1. F. W. Wiffen, "The Swelling of Nimonic PE-16 Irradiated in HFIR," *ADIP Quart. Prog. Rep. Sept. 30,* 1978, DOE/ET-0058/3, pp. 52-61.
2. F. W. Wiffen, E. J. Allen, H. Farrar, E. E. Bloom, T. A. Gabriel, H. T. Kerr, and F. G. Perey, "The Production Rate of Helium During Irradiation of Nickel in Thermal Spectrum Fission Reactors," paper in preparation for First Topical Meeting on Fusion Reactor Materials, Miami Beach, Florida, January 1979.
3. F. W. Wiffen, "The Response of Inconel 600 to Simulated Fusion Reactor Irradiation," *ADIP Quart.* Prog. *Rep. June 30,* 1978, DOE/ET-0058/2, pp. 62-81.

4.2 MECHANICAL PROPERTIES OF NIMONIC PE-16 FOLLOWING IRRADIATION IN HFIR — F. W. Wiffen (ORNL)

4.2.1 ADIP Task

ADIP Task I.B.14, Tensile Properties of High Strength-High Temperature Fe-Ni-Cr Alloys.

4.2.2 Objectives

Nimonic PE-16 was chosen as a representative precipitation-strengthened Path B alloy for investigation of the effect of HFIR irradiation on physical and mechanical properties. The HFIR experiments were initiated to investigate the response to irradiation producing helium levels representative of fusion reactor service simultaneously with production of displacement damage. Experiments in this series have been irradiated to neutron fluences producing 2 to 28 dpa and helium contents of 120 to 5700 at. ppm. Specimens irradiated at temperatures between 55 and 700°C are being examined to determine tensile properties and fracture mode. The results will be correlated with transmission electron microscopy of the microstructures produced by the irradiation.

4.2.3 Summary

Irradiation of solution treated and aged Nimonic PE-16 to produce 3 to 24 dpa and 180 to 4660 at. ppm He produced little or no change in the ultimate tensile strength of samples irradiated and tested near 55 or 500°C. In contrast, the yield stress was raised well above the control value by irradiation at either temperature. Samples irradiated at 55°C and then tested at higher temperatures showed a local minimum in strength change relative to control values and a local maximum in ductility at 600°C. At 600°C test temperature the failure mode was still transgranular. Tests at 650 or 700°C following the 55°C irradiation resulted in low elongation to failure. The fracture mode at 700°C was predominantly intergranular separation. In samples irradiated and

tested at 500°C the elongation remained above 5% for irradiation producing up to 8 dpa and 1000 at. ppm He but dropped below 2% for 11.5 dpa and 1700 at. ppm He or greater.

4.2.4 Progress and Status

4.2.4.1 Experiments

The composition of PE-16 (heat NNW-2282) used in this investigation is:

Element:	Ni	Cr	Fe	Mo	Al	Ti	Si	C	Mn
wt %:	43.1	16.5	bal	3.2	1.24	1.18	0.21	0.05	0.04

This composition produces an austenitic alloy that can be hardened by the precipitation of γ' phase, $Ni_3(Al,Ti)$. Rod specimens of this alloy were machined with a gage section 2 mm in diameter and 18 mm long. Machined samples were solution annealed in argon, either 2 h at 1120°C or 4 h at 1080°C, and then furnace cooled. The aged microstructure was developed by a further 16 h at 700°C.

Descriptions of the reactor experiments in this series have been given previously,[1,2] and the range of irradiation parameters and their relationship to fusion reactor conditions were reported last quarter.[3]

Displacement damage levels were calculated and helium contents calculated and correlated with measured values. These calculational procedures are discussed in Sect. 4.1 and in the previous quarterly report.[3]

Tensile tests were run on an Instron Universal Testing Machine, in a resistance-heated furnace operating in air. The samples were held for a 15-min equilibrium period at the test temperature before application of the load. All tests were run at a crosshead speed of 0.85 μm/s (0.002 in./min), for a nominal strain rate of 4.6×10^{-5}/s (0.0028/min). All stresses reported are based on the pretest specimen dimensions. Fracture diameters were measured after test with a micrometer, but the difficulties in hot cell measurement of diameters and in identifying the correct location to be measured on the sample

limit the usefulness of these results. The generally low ductilities also contribute to the difficulty in determining the reduction of area. More accurate measurements can be obtained by scanning electron microscope (SEM) techniques, but these samples have not yet been measured in that way.

Selected fracture surfaces were examined in an SEM to characterize the fracture mode.

4.2.4.2 Tensile Properties Following 55°C Irradiation

The results of tensile tests run at various temperatures following irradiation at 55°C are given in Table 4.2.1 and plotted as a function of temperature in Fig. 4.2.1. Also plotted in this figure are the tensile properties of solution treated and aged (STA) material and of material cold-worked approximately 50%, with no further heat treatment (CW). All the relevant irradiation and test parameters are included in Table 4.2.1.

Tensile tests at 35°C, near the irradiation temperature, resulted in near-equal yield and ultimate stresses. The yield stress (YS) after irradiation was about twice the value in the unirradiated STA material at the same test temperature. The ultimate tensile stress (UTS), however, was slightly lower than that of the control material. Both elongation values were lower than in the control sample, the uniform elongation near zero and the total elongation near 9%.

For tests at temperatures above the irradiation temperature, the UTS decreased with increasing test temperature and fell below the UTS of control specimens. The greatest difference between the UTS of control and irradiated material was found at 600°C, where the irradiated material was only 70% as strong as the control sample. The peak in postirradiation ductility as a function of test temperature also occurred at 600°C. At this temperature, following irradiation at 55°C, the uniform elongation was 20.9% and the total elongation to failure, in an 18.3-mm (0.72-in.) gage length, was 23.4%. At test temperatures of 650 and 700°C the ductility dropped to much lower values, presumably due to the dominance of the high helium content over the fracture mode.

Table 4.2.1. Irradiation Conditions and Tensile Properties of Nimonic PE-16 Irradiated in HFIR

Irradiation Parameters				Test Temperature (°C)	Strength,[a] MPa (ksi)		Ductility,[a] %		
Temperature (°C)	Fluence >0.1 MeV (n/m^2)	Displacement Level (dpa)	Helium Content (at. ppm)		0.2% Yield	Ultimate Tensile	Uniform Elongation	Total Elongation	Reduction of Area
				Solution Treated and Aged[b] Before Irradiation					
55	9.05×10^{25}	7.2	820	35	969 (140.6)	969 (140.6)	0.23	8.6	26
55	9.7	7.2	820	300	785 (113.8)	786 (114.0)	0.15	8.0	15
55	13.2	9.9	1400	300	751 (108.9)	761 (110.4)	5.9	11.9	37
55	11.2	8.4	1050	600	480 (69.6)	563 (81.7)	20.9	23.4	29
55	10.7	8.4	1040	650	503 (73.0)	521 (75.5)	1.7	2.8	15
55	5.4	3.9	355	700	477 (69.2)	477 (69.2)	0.24	0.79	2.5
	Control			35	450 (65.3)	996 (144.4)	28.2	32.3	40
	Control			300	395 (57.3)	911 (132.2)	33.7	37.0	
	Control			500	411 (59.6)	836 (121.2)	30.4	33.5	32
	Control			600	406 (58.9)	805 (116.7)	25.1	29.5	
	Control			650	429 (62.2)	721 (104.6)	16.4	20.9	
	Control			700	401 (58.1)	545 (79.0)	8.7	12.8	
500	3.77	3.0	184	500	590 (85.5)	839 (121.7)	13.9	14.4	23
500	5.59	4.2	349	500	572 (83.0)	701 (101.6)	5.0	5.6	12
500	10.4	7.9	978	500	678[c] (98.3)	884 (128.2)	10.6	11.0	18
500	14.6	11.5	1720	500	803 (116.5)	823 (119.3)	0.35	0.37	12
500	21.6	16.4	2860	500	642 (93.1)	725 (105.2)	1.28	1.34	17
500	29.4	23.2	4660	500	854 (123.9)	866 (125.6)	0.35	0.37	2.5
				~50% Cold Worked					
	Control			400	1176 (170.6)	1176 (170.6)	0.23	3.36	
	Control			600	945 (137.0)	967 (140.3)	0.80	17.4	
	Control			700	558 (81.0)	573 (83.1)	0.40	33.2	

[a] All tests at a strain rate of 4.6×10^{-5}/s (0.0028/min).

[b] 4 h at 1080°C plus 16 h at 700°C.

[c] This sample only, solution treatment was 2 h at 1120°C before aging 16 h at 700°C.

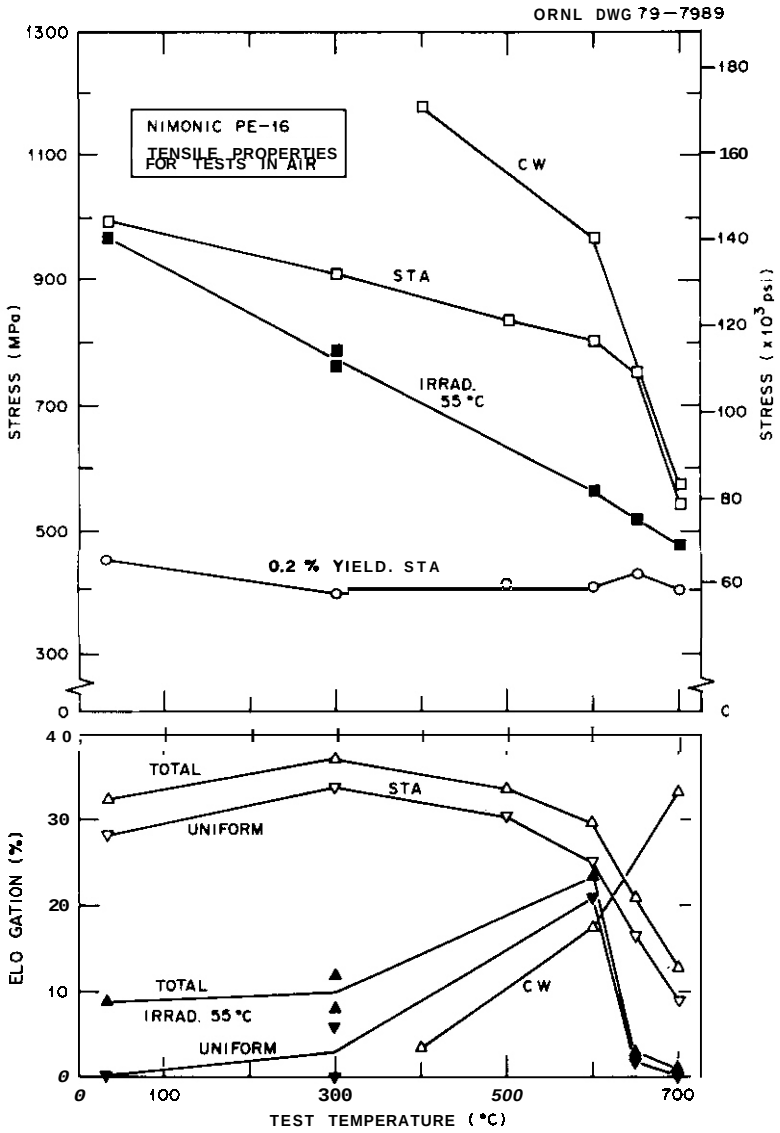

Fig. 4.2.1. The Tensile Properties of Nimonic PE-16 Irradiated, in the Solution Treated and Aged (STA) Condition, at 55°C and then Tested at Various Temperatures. The irradiation produced 4 to 10 dpa and helium contents from 350 to 1400 at. ppm. (Exact values are given in Table 4.2.1.) The properties of control STA material and 50%-cold-worked material are plotted for comparison.

A few results of tests on approximately 50%-cold-worked (CW) material are included in Fig. 4.2.1 for comparison. They show much greater strength than either the irradiated or STA material for tests at 400 and 600°C and about equal strength to the STA condition at 700°C. The uniform elongation of CW material was less than 1% for all three test temperatures. The total elongation was lower than that of irradiated or STA material at 400 and 600°C, but was highest of all three material conditions at the 700°C test temperature.

4.2.4.3 Fracture Mode Following 55°C Irradiation

Examination of the fracture surface of the sample irradiated at 55°C and then tested at 600°C showed the surface to be covered with the dimples characteristic of a ductile shear failure model. A typical segment of this surface is shown in Fig. 4.2.2(a). Only isolated zones (less than 5% of the surface) showed features possibly indicative of a small component of intergranular separation. The surface appearance was consistent with the high ductility measured in the tensile test.

The fracture surface on the sample tested at 700°C, Fig. 4.2.2(b), showed predominantly intergranular separation, with some zones of ductile tearing joining the exposed grain boundaries. The zones of tearing occupied approximately 20 to 30% of the fracture surface and are judged to show a secondary failure mode through grains not favorably oriented for grain boundary separation.

4.2.4.4 The 500°C Tensile Properties Following 500°C Irradiation

A series of specimens in the STA condition before irradiation at 500°C were irradiated to dpa levels in the range 3.0 to 13.2 and helium contents from 184 to 4660 at. ppm. The tensile properties of these specimens in tests at 500°C are listed in Table 4.2.1 and shown graphically in Fig. 4.2.3.

For the range of fluences examined, the UTS was relatively little affected by the irradiation. The average of all UTS values was 96% of the UTS of a control sample, and the irradiated UTS values fell between 87 and 110% of this range. The 0.2% yield stress increased with

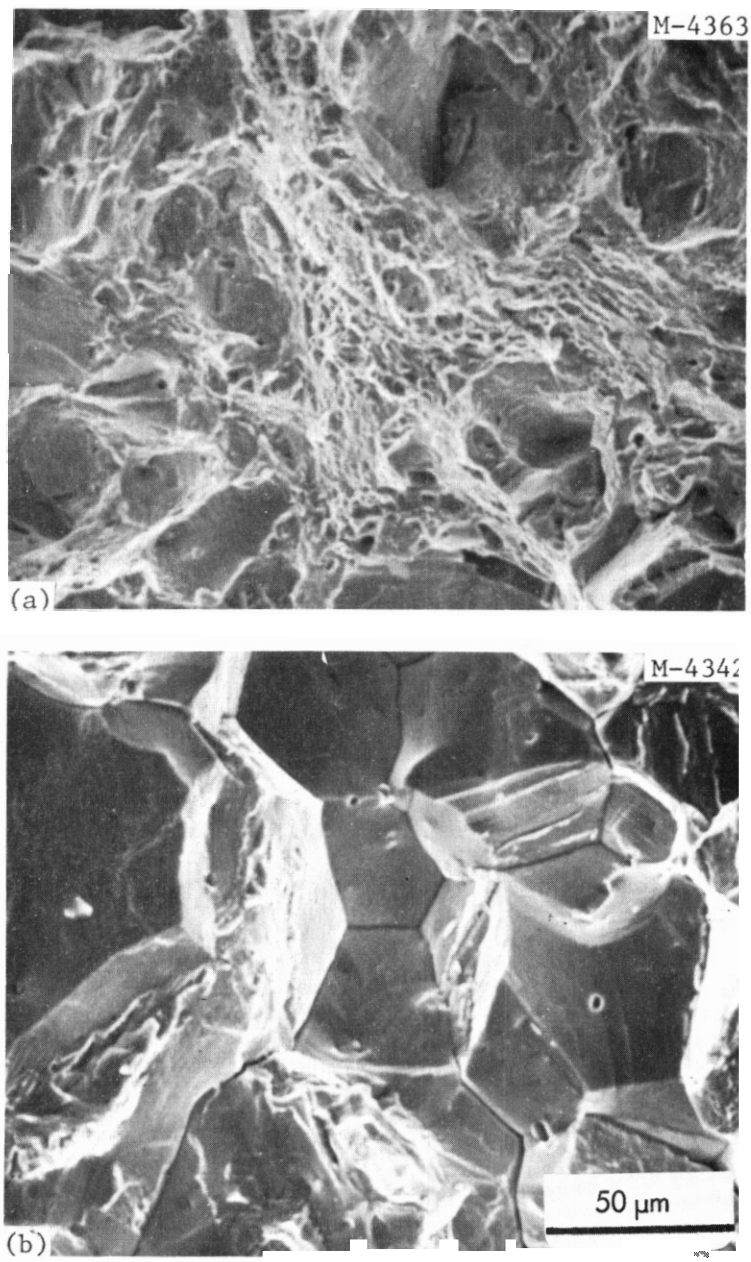

Fig. 4.2.2. **Typical Fracture Surfaces of Nimonic** PE-16 **Solution Treated and Aged, then Irradiated at** 55°C. **These samples were tensile tested (a) at** 600°C **and (b) at** 700°C.

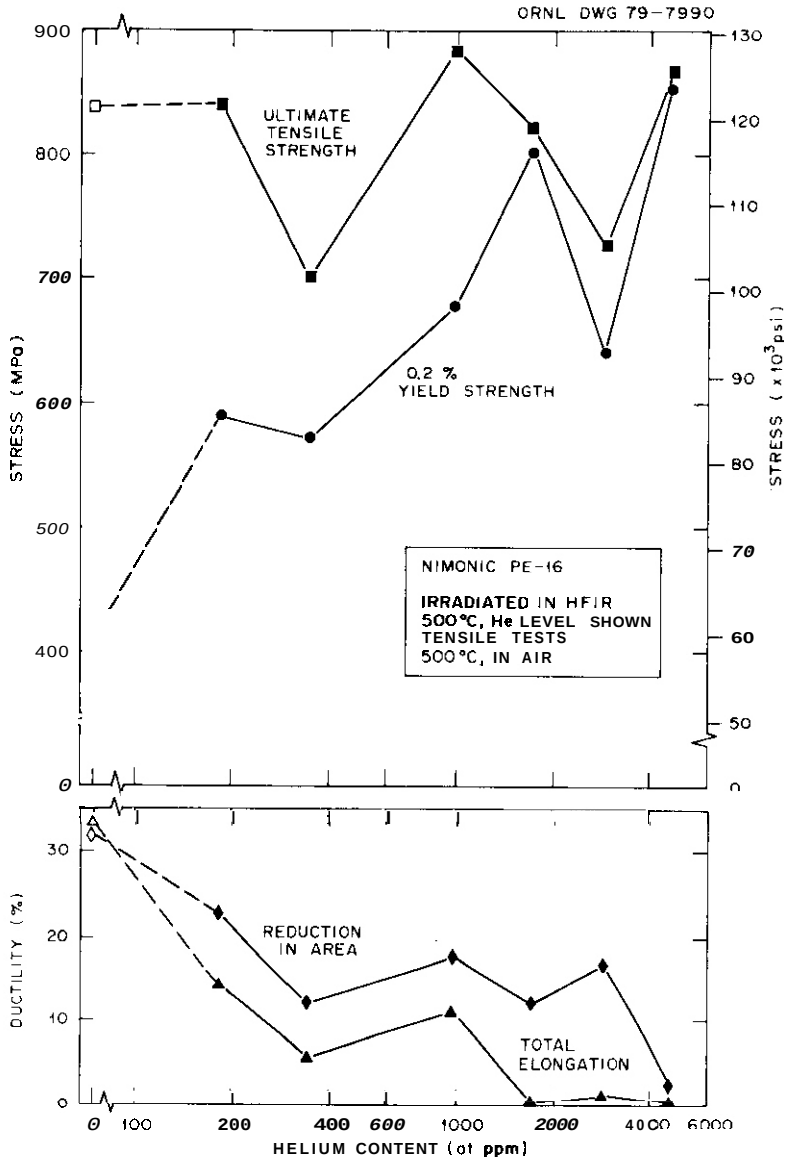

Fig. *4.2.3*. The Tensile Properties of Nimonic PE-16 Irradiated at 500°C in the STA Condition and Tested at 500°C. The data are plotted against logarithmic helium content; fluence or dpa do not scale linearly with helium content.

increasing fluence, and was within about 90% of the UTS for fluences producing more than 10 dpa. Elongation values decreased with increasing fluence: total elongation was below 2% for fluences producing more than 10 dpa. Reduction of area values remained above 10% for all but the highest fluence irradiation.

4.2.5 Future Work

Additional tensile test results, fractography to define the fracture mode, and more detailed analysis of the results will be reported in future quarterly reports.

4.2.6 References

1. F. W. Wiffen, "The Effects of Irradiation at About 55°C on Type 316 Stainless Steel," *ADIP Quart. Prog. Rep. March 31, 1978*, DOE/ET-0058/1, pp. 89–93.
2. F. W. Wiffen, "The Response of Inconel 600 to Simulated Fusion Reactor Irradiation," ADIP *Quart. Prog. Rep. June 30*, 1978, DOE/ET-0058/2, pp. 62–81.
3. F. W. Wiffen, "The Swelling of Nimonic PE-16 Irradiated in HFIR," *ADIP Quart. Prog. Rep. Sept. 30*, 1978, DOE/ET-0058/3, pp. 52–61.

4.3 STATUS OF PATH B BASE RESEARCH ALLOY PROCUREMENT AND FABRICATION — T. K. Roche (ORNL)

4.3.1 ADIP Task

ADIP Task I.D.1, Materials Stockpile for MFE Programs.

4.3.2 Objectives

The objective of this activity is to procure the five Path B Base Research Alloys, which will provide a starting point for development of high-strength precipitation strengthened alloys with properties specifically tailored for fusion applications.

4.3.3 Summary

Two 140-kg heats of each of five high-nickel alloys were double vacuum melted and hot rolled into bar stock. Some of each alloy has been received and extruded into round and sheet bar. The alloy containing 75% nickel shows some cracking and tearing on fabrication.

4.3.4 Progress and Status

Two 140-kg (300-lb) heats of each of the five Path B Base Research Alloys of nominal composition given in Table 4.3.1 have been made by Teledyne Allvac. As with the Path A Prime Candidate Alloy (Sect. 3.2), these alloys were prepared by double vacuum melting, vacuum induction melt (VIM) followed by comsumable-electrode vacuum arc remelt (VAR) from virgin materials. Each of the two 140-kg (300-lb) VIM heats per alloy was cast into two 108-mm-diam (4 1/4-in.) VAR electrodes. The four resulting electrodes per alloy were each vacuum arc remelted into a 0.15-m-diam (6-in.) ingot. The ingots were homogenized for 16 h at 1150°C (2100°F), then hot rolled to 100-mm (4-in.) round-cornered square bars in the temperature range 871 to 1038°C (1600–1900°F). After rolling, the bars were annealed for 0.5 h at 1038°C (1900°F) and water quenched. The bars were finally surface conditioned by grinding. Approximately 180 kg (400 lb) of bar stock of each alloy

Table 4.3.1. Nominal Composition of Path B Base Research Alloys

Alloy	Composition,[a] wt %							
	Ni	Cr	Mo	Nb	Ti	Al	Mn	C
B-1	25	10	1		3	1.5	1	0.03
B-2	40	12	3		1.5	1.5	0.2	0.03
E 3	30	12		2 '	2	0.5	1	0.03
B-4	40	12		3	1.8	0.3	0.2	0.03
B-6	75	15		1	2.5	1.5	0.2	0.03

[a] Balance iron.

has been received. Visual inspection of the product showed alloys B-1 through B-4 to have fabricated quite well. The nickel-base alloy, B-6, showed some scattered surface cracks.

Since receipt of the Path B alloys at ORNL, two 0.10-m-diam by 0.15-m-long (4 by 6-in.) billets of each alloy were machined and extruded to 32-mm-diam (1 1/4-in.) round bar and 22-nun-thick (7/8-in.) sheet bar. These extrusions were carried out at 1150°C (2100°F) at ratios of 10.2 to 1 and 4.6 to 1. Visually, the extrusions of alloys B-1 through B-4 were of high quality. Both extrusions of alloy B-6 showed a limited amount of hot tearing at the nose end, which required conditioning. The extrusions recently completed will provide the starting stock for fabrication of sheet and/or rod required for irradiation experiments. Material had been provided to Hanford Engineering Development Laboratory for microstructural studies and recommendation of heat treatments (i.e., microstructures) to be evaluated 'for irradiation performance.

5. PATH C ALLOY DEVELOPMENT — REACTIVE AND REFRACTORY ALLOYS

Two distinct and separate subgroups fall under the broad classification of path C alloys. These subgroups are conveniently classified as "reactive metal alloys" and "refractory metal alloys." Analyses of the properties required for performance of materials in high-flux regions of fusion reactors and assessments of the known and extrapolated properties have identified titanium alloys of the reactive metal alloys and vanadium and niobium alloys of the refractory metal alloys as having the most promise for fusion reactor applications. For both the reactive and refractory alloys, there is an extreme lack of data that are relevant and necessary for selection of specific alloy types for development (i.e., solid solution, precipitation strengthened, single or multiphase). In the case of titanium alloys, the most critical deficiency is the lack of data on the response of these alloys to high-fluence neutron radiation. For vanadium and niobium alloys, while the effects of radiation on mechanical behavior are not adequately known, perhaps the most alarming deficiency is the near total lack of base-line information on the effects of cyclic (fatigue) loading on mechanical performance. Precisely because of these deficiencies in the data base and overall metallurgical experience, these alloys are still in a "scoping study" phase of their evaluation as candidates for fusion reactor first-wall materials.

The ADIP task group has selected four titanium alloys, three vanadium alloys, and two niobium alloys for the scoping phase of the development program. Titanium alloys are generally classified according to the relative amounts of α (hcp) and β (bcc) phases that they contain. The titanium alloys selected represent the three alloys (types α plus β, α rich, and β rich). Vanadium and niobium alloys are not in commercial use as are the other alloy systems in the program. Selection of the scoping alloys was based primarily on results of previous programs on vanadium cladding development for LMFBRs and high-temperature alloys for space power systems. The three vanadium alloys are V–20% Ti, V–15% Cr–5% Ti, and Vanstar 7. The binary has relatively good fabricability, and appears to be swelling resistant in fast-reactor irradiations but

is rather weak. The ternary V–15% Cr–5% Ti and precipitation-strengthened Vanstar 7 alloys are significantly stronger. The Nb–1% Zr binary alloy is included as a reference material, since a significant amount of data exists for this alloy irradiated in fast reactors. The alloy Nb–5% Mo–1% Zr is much stronger than the binary and can be developed for applications near 800°C.

Near-term activities on path C alloys will focus on obtaining data on the unirradiated mechanical properties, corrosion, and compatibility, and the effects of irradiation on physical and mechanical properties. Fission reactor irradiation with and without helium preinjection, high-energy neutron sources, and charged-particle irradiations will be used in the development of techniques to approximate the effects of the fusion reactor neutron spectrum (He/dpa production). The objective is to develop sufficient understanding of the behavior of path C alloy systems (Ti, V, and Nb alloys) to allow selection of path C base research alloys. The effects of composition and microstructure on alloy performance will then be investigated in the base research alloys.

5.1 PREPARATION OF VANADIUM AND NIOBIUM PATH C SCOPING ALLOYS —

R. E. Gold, R. L. Ammon, and R. W. Buckman, Jr. (Westinghouse Electric Corporation)

5.1.1 ADIP Task

I.D.l. Materials Stockpile for MFE Programs (Path C)

5.1.2 Objective

The purpose of this effort is to provide sufficient quantities of the vanadium and niobium Path c Scoping Alloys to permit initial evaluation of the potential these types of alloys might offer for fusion reactor applications. Final product forms, which are to be delivered to the Oak Ridge National Laboratory Fusion Materials Stockpile[1], include 2.5 mm (0.10 in.) plate, 1.5 mm (0.06 in.) and 0.76 mm (0.03 in.) sheet, and 6.4 mm (0.25 in.) diameter rod.

5.1.3 Summary

Three vanadium alloy and two niobium alloy compositions are being prepared for consumable arc melting and processing to plate, sheet, and rod for the Fusion Materials Stockpile. These are the Path C (V, Nb) Scoping Alloys selected for initial evaluations as candidate fusion reactor structural materials. First-melt electrodes of the niobium alloys have been prepared and are ready for melting. Preparation of the vanadium alloy electrodes has been delayed due to difficulties associated with breakdown of the as-received 3.8 cm (1.5 inch) diameter vanadium rods. The nitrogen level of the vanadium is much higher than reported by the vendor; this has made it impossible to cold-roll the rod to electrode strip as was originally planned. The vanadium rods are being cold-swaged to a size where they can be further processed to thin strip for preparation of the consumable arc-melt electrodes.

5.1.4 Progress and Status

The vanadium and niobium scoping alloy compositions which are being prepared include:

- V-20 Ti
- V-15 Cr-5 Ti
- VANSTAR-7 (V-9 Cr-3.3 Fe-1.3 Zr-0.054 C)
- Nb-1 Zr
- Nb-5 Mo-1 Zr

(All compositions in weight percent)

The melting and processing schedules for producing the target plate, sheet, and rod material are outlined in Figures 5.1.1 and 5.1.2.

Some delay was encountered in getting the full vanadium order from the Materials Research Coroporation and the niobium starting melt stock from Kawecki-Berylco but all material required for electrode fabrication has now been received. Interstitial chemical analyses of the major alloy ingredients are shown on Table 5.1.1. Included are check analyses performed at the Westinghouse Research and Development Center. Notice the large discrepancy between the vendor-reported analyses for the vanadium rod stock and the Westinghouse check analyses.

The vanadium was supplied as approximately 3.8 cm (1.5 in.) diameter rod stock. First attempts to reduce this to flat electrode stock by rolling indicated the material to be much stronger than the vendor chemistry implied. The reason for this became apparent when the interstitial check chemical analyses were completed; note the very high nitrogen content of the vanadium. Inquiries have been directed to the supplier (MRC) regarding this very large discrepancy; vendor response has not been received. Vanadium procured directly by ORNL from MRC at about the same time has also been found to have interstitial levels well above those reported by the vendor.'

Vanadium having 700-800 wppm interstitials can be processed; much of the early development efforts utilized less pure metal. It does, however, impose certain limitations on processing. As mentioned above, it is very difficult to cold-roll material containing this level of nitrogen or oxygen. Swaging provides a much better primary reduction

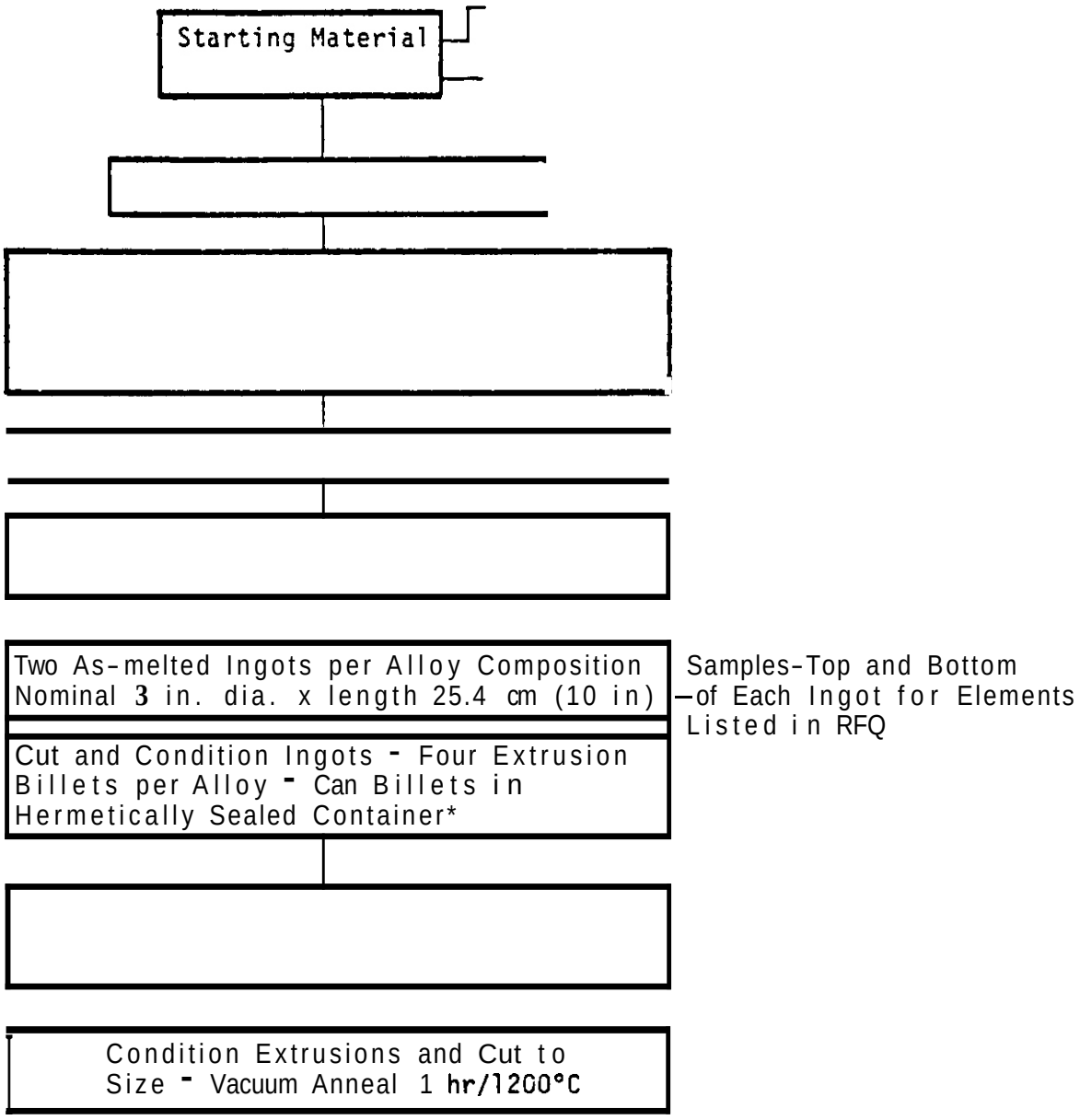

* All encapsulations in hermetically sealed 300 series stainless steel or degassed mild steel containers.

Figure 5.1.1. Melting and Primary Breakdown Schedule for Experimental Vanadium and Niobium Scoping Alloys.

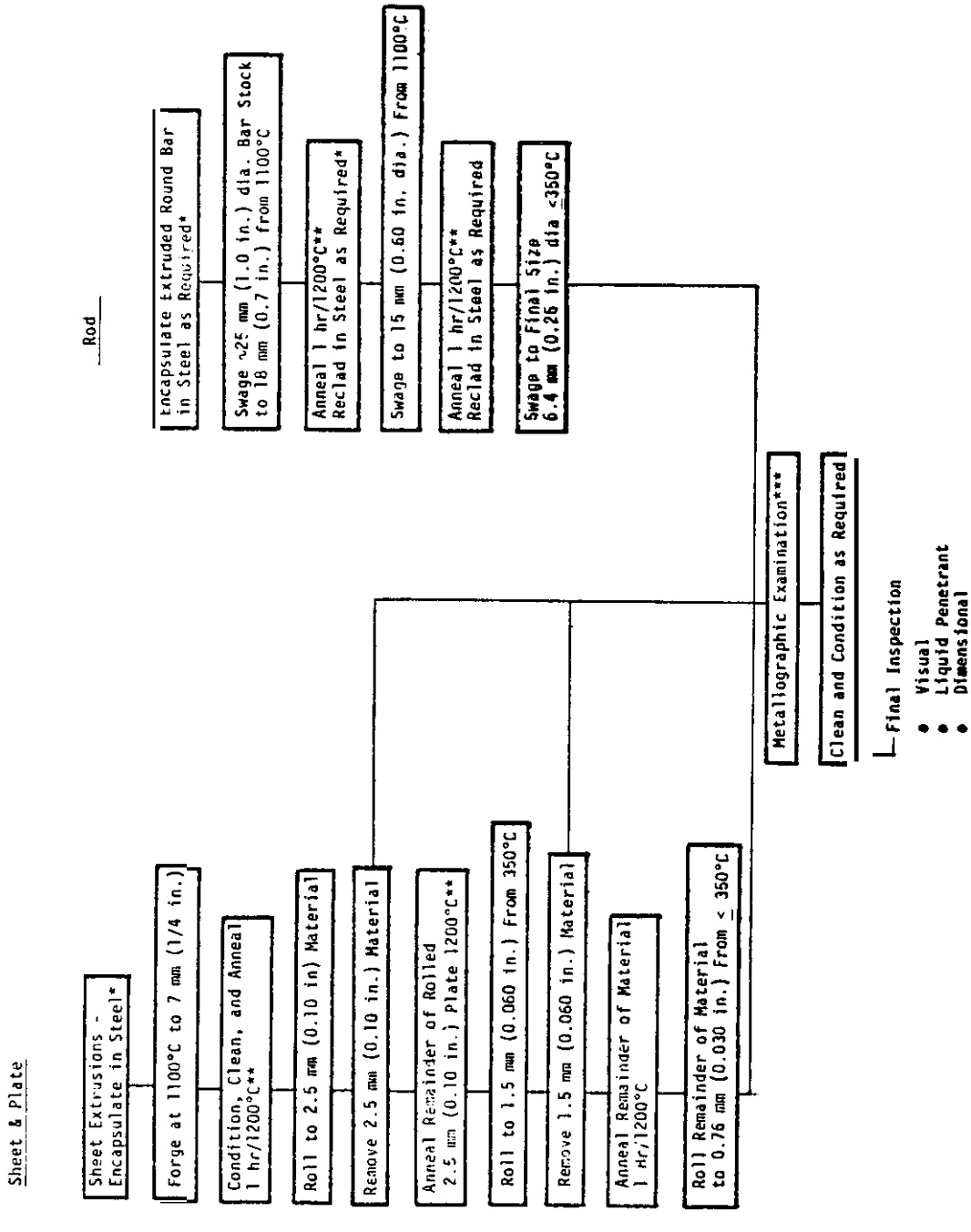

Figure 5.1.2. Plate, Sheet, and Rod Fabrication Schedules for Experimental Vanadium and Niobium Scoping Alloys.

Table 5.1.1 Interstitial Chemical Analyses of Starting Material for Vanadium and Niobium Scoping Alloys

METAL	LOT NUMBER	VENDOR ANALYSIS C	O	N	(W) CHECK ANALYSIS C	O	N
V	1				97	210	750
	2				200	52	560
	9	15	220	35	210	67	620
	13				400	42	530
	17				150	32	610
Nb	—	—	—	—	5	90	65
Mo	—	—	—	—	13	52	17

option. Material at ORNL has been cold-reduced by swaging from the 3.8 cm (1.5 in.) diameter starting stock without difficulty.* The Advanced Energy Systems Division of Westinghouse does not have swage die inventory at that size; hence the vanadium has been shipped to ORNL for swaging to a diameter below about 3.1 cm (about 1.25 in.) fron which it can be further reduced by Westinghouse to strip for electrode fabrication.

After melting, and at each of the final product yield forms, chemical analyses for both metallic solutes and interstitials will be performed. The vanadium alloys, in particular, will require close scrutiny and careful processing procedures.

The Nb-1 Zr and Nb-5 Mo-1 Zr first-melt electrodes have been prepared and are ready for melting. Eight (8) first-melt electrodes of each composition have been prepared. These will be melted and combined for remelting to yield two ingots of each composition.

5.1.5 References

1. Contract No. 77X-85932V, "Program to Melt and Fabricate Experimental Vanadium and Niobium Alloys for Scoping Evaluations as Fusion Reactor Structural Material Applications," contract between Union Carbide Corporation, Nuclear Division and Westinghouse Electric Corporation.

2. T. K. Roche, Oak Ridge National Laboratory, personal communication, December 1978.

5.2 THE MICROSTRUCTURE OF Ti-6242s FOLLOWING LOW-FLUENCE NEUTRON IRRADIATION AT 400°C - J.A. Sprague and F.A. Smidt, Jr., (Naval Research Laboratory)

5.2.1 ADIP Task

Task Number I.C.4 - Microstructures and Swelling in Reactive/Refractory Alloys (Path C)

5.2.2 Objective

The objective of this study was to examine the microstructure of the titanium scoping alloy Ti-6242s following low-fluence neutron irradiation to obtain a preliminary indication of the stability of this alloy in an irradiation environment.

5.3.3 Summary

The microstructure of Ti-6242s was studied by transmission electron microscopy (TEM) after irradiation in EBR-II to a fluence of 3.7×10^{21} neutrons/cm^2 ($E > 0.1$ MeV) at 400°C. The overall phase distribution in the alloy, equiaxed primary alpha with a small amount of transformed beta, was unaffected by this irradiation exposure. Electron diffraction patterns indicated the probable presence of the alpha-2, Ti_3 (Al, Sn), but it could not be determined if this phase precipitated during heat treatment or during irradiation. The principal irradiation-induced microstructural feature was a dense distribution of small dislocation loops in the primary alpha grains. The individual alpha plates in the transformed beta were very fine, as before irradiation, but they appeared to be somewhat irregularly shaped, possibly due to interference from the contrast of irradiation-induced lattice defects.

5.2.4 Progress and Status

Titanium alloys have many qualities, including high strength-to-weight ratios and potentially low long-term radioactivity, that make them appear attractive for fusion reactor first-wall and blanket applications. The responses of the microstructures and properties of

these alloys to high-fluence irradiation at elevated temperatures, however, are largely unknown. The first opportunity to examine the microstructures of the ADIP titanium scoping alloys following neutron irradiation has been provided by the stess-relaxation irradiation creep experiment, which was described by R.E. Nygren in a previous report[1]. The microstructures of unstressed control specimens are being examined in a joint effort among McDonnell Douglas, HEDL and NRL to provide a preliminary indication of the phase stability and general irradiation response of these alloys. In the NRL portion of this work during the past quarter, Ti-624% (Ti-6% A1-2% Sn-4% Zr-2% Mo-0.09% Si) was examined by TEM after irradiation in EBR-II to a fluence of 3.7 x 10^{21} n/cm^2 ($E > 0.1$ MeV) at a temperature of 400°C[2]. Although this low neutron fluence corresponds to only approximately 1.4 dpa, damage levels of this order can often provide useful insights regarding the stability of an alloy during irradiaton.

As discussed by J.W. Davis, et al[3], the pre-irradiation annealing cycle for Ti-6242s was 30 minutes at 900°C, a rapid cool to room temperature, and a reanneal for 15 minutes at 790°C. This treatment produced a phase distribution consisting principally of equiaxed primary alpha with a small amount of transformed beta. As shown in Fig. 5.2.1(a), this general structure was not significantly affected by the irradiation. When imaged at higher magnification, as in Fig. 5.2.1(b), the transformed beta grains appeared to have a very fine and irregular platelet structure. The contrast from these grains was too complex to interpret readily, but it probably resulted from a combination of the pre-irradiation alpha-beta structure and some irradiation-induced lattice defects. The primary alpha grains had a somewhat simpler internal structure, as illustrated in Fig. 5.2.2(a). The main feature which could be observed here was a high density of small dislocation loops, some of which appeared to be clustered together. While there was no evidence of precipitation in the diffraction contrast images of the alpha grains, the electron diffraction patterns of these grains contained weak reflections that could be identified as the alpha-2 phase, as shown in Fig 5.2.2(b). This phase, which is

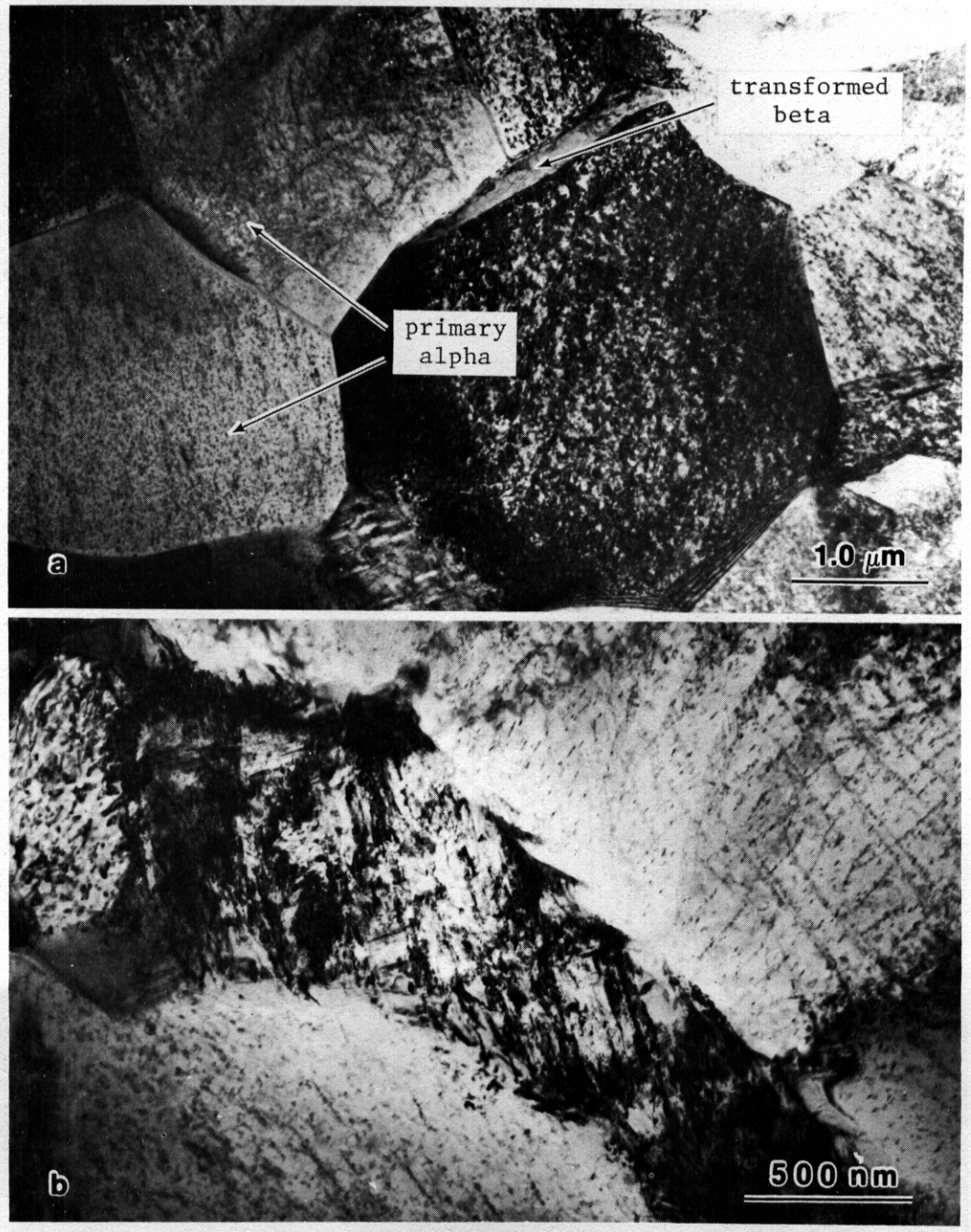

5.2.1. Phase distributions observed in neutron irradiated Ti-6242S: (a) general microstructure, showing equiaxed primary alpha an transformed beta grains; (b) internal structure of a transformed bet grain.

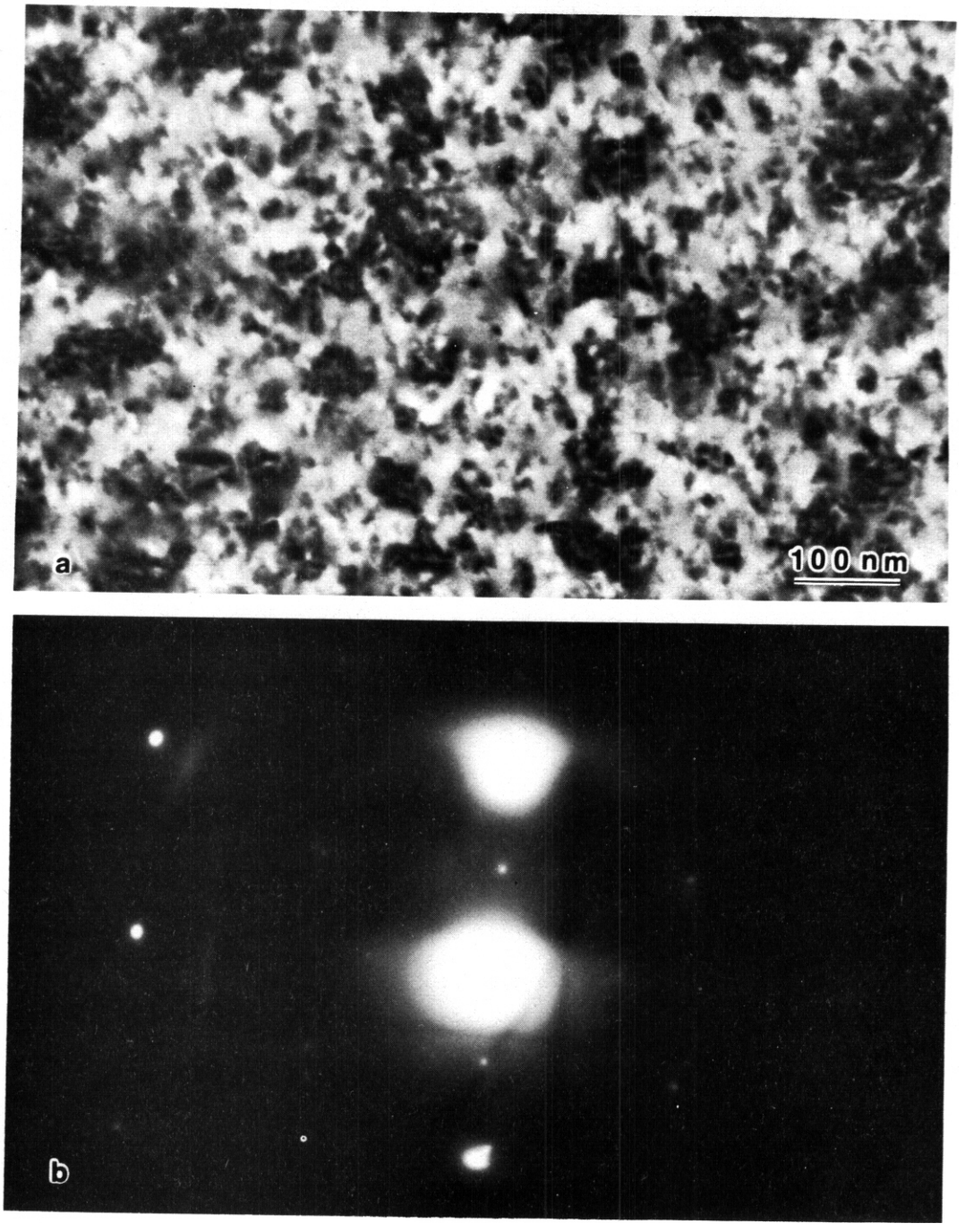

5.2.2. (a) Dislocation loops in primary alpha grain of neutron irradiated Ti-6242s; (b) selected-area diffraction pattern of (a), showing $[11\bar{2}0]$ primary reflection and superlattice spots identified as $[11\bar{2}0]$ Ti (Al, Sn) reflections.

$Ti_3(Al, Sn)$ with the DO_{19} hexagonal superlattice structure, would produce $[1\bar{1}20]$ reflections approximately halfway between the $[11\bar{2}0]$ reflections of the primary alpha, as seen in the figure. Attempts to image the alpha-2 in darkfield to check for association of this phase with the irradiation-induced dislocation loops were not successful, due to the weakness of the reflections. Although alpha-2 was not reported in the pre-irradiation microstructure microstructure of Ti-6242S[3], this may not be an irradiation-induced phase, since it is often observed in this class of alloys following normal heat treatment or long-term thermal aging.

In summary, the initial indications are that Ti-6242s is a fairly stable alloy under neutron irradiation at 400°C. Higher fluence irradiations will obviously be required to extend this observation to conditions of interest for fusion reactor applications.

5.2.5 Future Work

During the next quarter, specimens of Ti-5621S, Ti-15333, and Ti-38644 will be studied by TEM following irradiation in the same stress-relaxation experiment. In addition, a further effort will be made to determine the site of the Ti (Al, Sn) precipitation and whether it is occurring during annealing or irradiation.

5.2.6 References

1. R.E. Nygren, "Irradiation Induced Stress Relaxation in Titanium Alloys," Alloy Development for Irradiation Performance Quarterly Progress Report for Period Ending June 30, 1978, p. 106.

2. R.W. Powell, Hanford Engineering Development Laboratory, private communication.

3. J.W. Davis, S.M.L. Sastry, and L.J. Pionke, "Microstructure of Titanium Scoping Alloys Prior to Irradiation," Alloy Development for Irradiation Performance Quarterly Progress Report for Period Ending June 30, 1978, p. 85.

Acknowledgment

We wish to thank J.C. Williams of Carnegie Mellon University and C.G. Rhodes of Rockwell International for helpful discussions regarding the microstructures of titanium alloys.

5.3 COMPARISON OF TITANIUM ALLOY Ti-6Al-4V AND Ti-5621s MICROSTRUCTURES AFTER EBR-II IRRADIATION - S. M. L. Sastry, J. E. O'Neal and J. W. Davis (McDonnell Douglas)

5.3.1 ADIP Tasks

Task Number 1.C.4 - Microstructure and Swelling in Reactive and Refractory Alloys (Path C)

5.3.2 Objective

To determine the response of titanium microstructures to neutron irradiation.

5.3.3 Summary

Microstructural analysis was performed on two types of titanium alloys, the $\alpha + \beta$ alloy Ti-6Al-4V in the mill anneal and duplex anneal condition and the near alpha alloy Ti-5621s in the duplex anneal condition after neutron irradiation. The irradiations were made in Row VII of EBR-II to a fluence of 3.4 x 10^{21} n/cm^2 (E_n > 0.1 MeV) at 450°C. This fluence results in roughly 1.5 dpa's of damage. Analysis of the Ti-6Al-4V revealed that both conditions of Ti-6A1-4V contained a fine precipitate of what is believed to be beta phase and a high density of dislocation loops and debris. The precipitates are essentially ellipsoidal in shape and are roughly 100-200A° in size. The precipitates appear to follow the Burgers relationships and were found to occur at low angle grain boundaries and along dislocations which were produced during the heat treatment. These precipitates appear to be unique to irradiated titanium and have not been observed as a result of long term thermal exposure. The Ti-5621s alloy showed no evidence of this precipitate. The primary defect structure of the Ti-5621s was extensive dislocation loops and c + a type of dislocations.

5.3.4 Progress and Status

Titanium alloys are one group of materials currently under consideration for use as the first wall and blanket structure of a fusion reactor. However, the effect of neutron irradiation on the microstructure and mechanical properties of titanium is largely unknown. In an effort to develop a better understanding of the response of titanium to neutron irradiation, a series of experiments are currently in progress using the fission reactors EBR-II and O.R.R. The first of these experiments was an irradiation creep study performed by HEDL.(1) In this study six titanium alloy/conditions were evaluated. These alloys were the alpha plus beta alloy Ti-6Al-4V, which was evaluated in the mill, duplex, and beta anneal condition; the near alpha alloys Ti-5621s and Ti6242S, which were evaluated in the duplex condition; and the beta alloy Ti-15-3, which was in the solution treat and aged condition. All samples were irradiated in Row VII of EBR-II to a fluence of 3.4×10^{21} n/cm^2 (E_n > 0.1 MeV) and a temperature of ∿ 450°C. Preliminary analysis indicate that this fluence results in ∿ 1.5 dpa's of damage in the titanium.

After irradiation, microstructural samples were obtained from the unstressed specimens and divided among HEDL, NRL, and MDAC for subsequent analysis. The work reported in this section was performed on these samples which were received from HEDL. The samples were in the form of 3 mm discs which were punched from 0.3 mm sheet. The 0.3 mm sheet was obtained by chem-milling 1 mm sheet in a nitric-hydrochloric acid solution.

5.3.4.1 Experimental Technique

In the current reporting period the post irradiated microstructures of mill annealed and duplex annealed Ti-6Al-4V and duplex annealed Ti-5621s were examined using optical and transmission electron microscopy techniques and the results compared with an unirradated microstructure. The optical samples were prepared by polishing with a 3 µm diamond abrasive while the TEM samples were thinned by the electrolytic jet technique using a cooled solution of methanol-butanol-perchloric acid. The temperature of the electrolyte during thinning was always maintained

below -15°C to prevent hydrogen pick-up and hydride formation. To quantify the irradiation induced defect microstructure, grains of several different orientations were examined using bright field, conventional orientations, and weak beam dark field methods. In addition to metallography the microhardness of both irradiated and unirradiated samples was determined on the 3 mm diameter discs using a LEITZ microhardness tests and a 50 g load.

5.3.4.2 Results and Discussion

Optical examination of the samples revealed that there were no significant differences between the unirradiated and irradiated alloys. However, profound differences were noted by TEM. The most significant differences were those observed between the alpha-beta alloy (Ti-6Al-4V) and the near alpha alloy Ti-5621s.

- Post-Irradiation Microstructures of Mill Annealed and Duplex Annealed Ti-6Al-4V

  Figures 5.3.1 and 5.3.2 are the electron micrographs of duplex and mill annealed Ti-6Al-4V in the irradiated and unirradiated condition. The microstructures of the irradiated specimens consist of a high density of very fine dislocation loops and dislocation debris along with a fine ellipsoidal shaped precipitate about 100-200Å in size. The fine precipitates are shown in Figure 5.3.3 which is a high magnification dark field micrograph taken with a precipitate reflection. The precipitates were analyzed by selected area diffraction (SAD) and were identified as beta phase . The SAD patterns shown in Figures 5.3.4a and 5.3.4b are consistent with the b.c.c. beta phase and the orientation relationships conform to the Burgers orientation relationships viz $(0001)_\alpha \,||\, (110)_\beta$ and as $< 11\bar{2}0 > \,||\, < 111 >_\beta$. The beta precipitates were found preferentially along dislocation lines, low angle boundaries and grain boundaries, as seen in Figure 5.3.5 The extent of beta precipitation is higher in the duplex annealed Ti-6Al-4V than in the mill annealed Ti-6Al-4V.

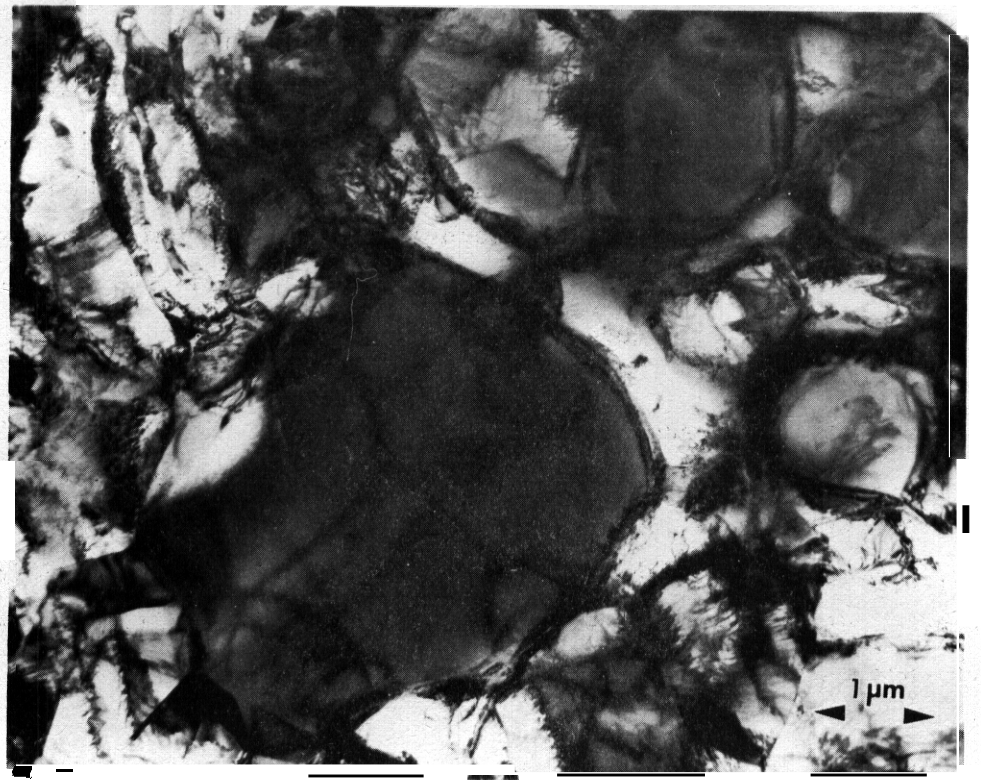

(a) unirradiated

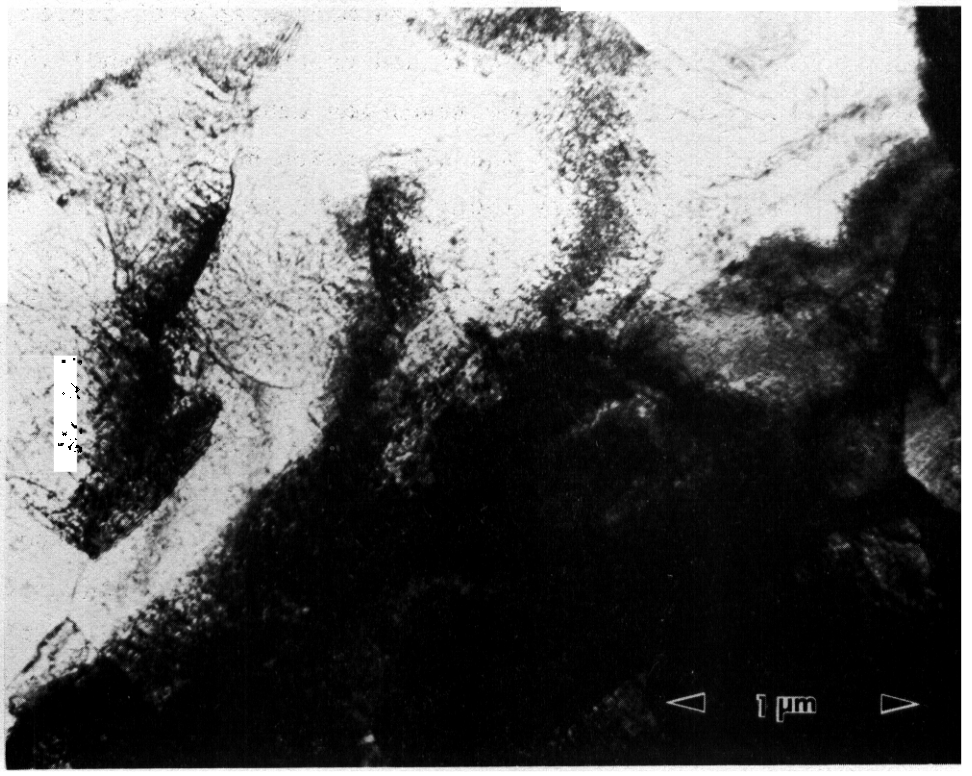

(b) irradiated

Fig. 5.3.1 Microstructures of Mill Annealed Ti-6Al-4V

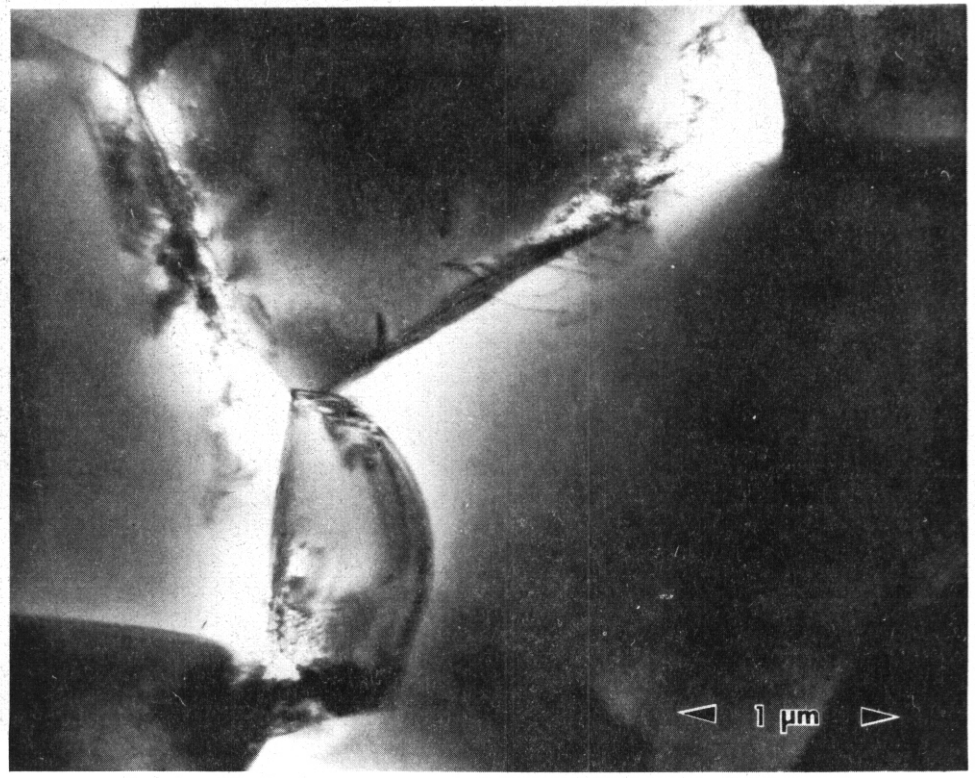

(a) unirradiated

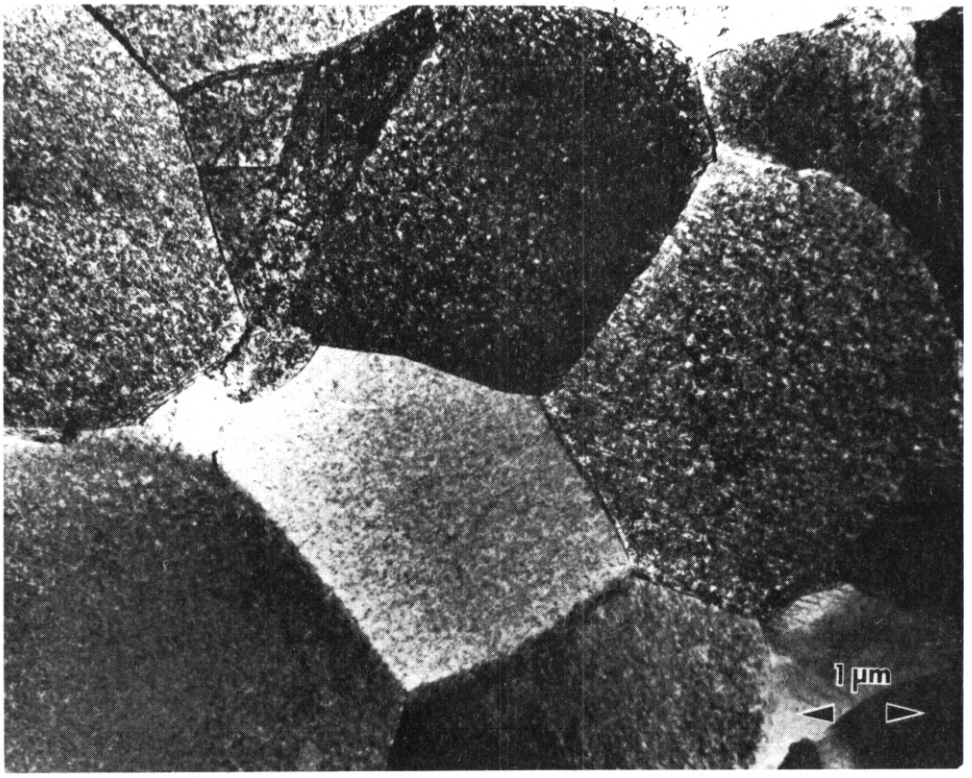

(b) irradiated

Fig. 5.3.2 Microstructures of Duplex Annealed Ti-6Al-4V

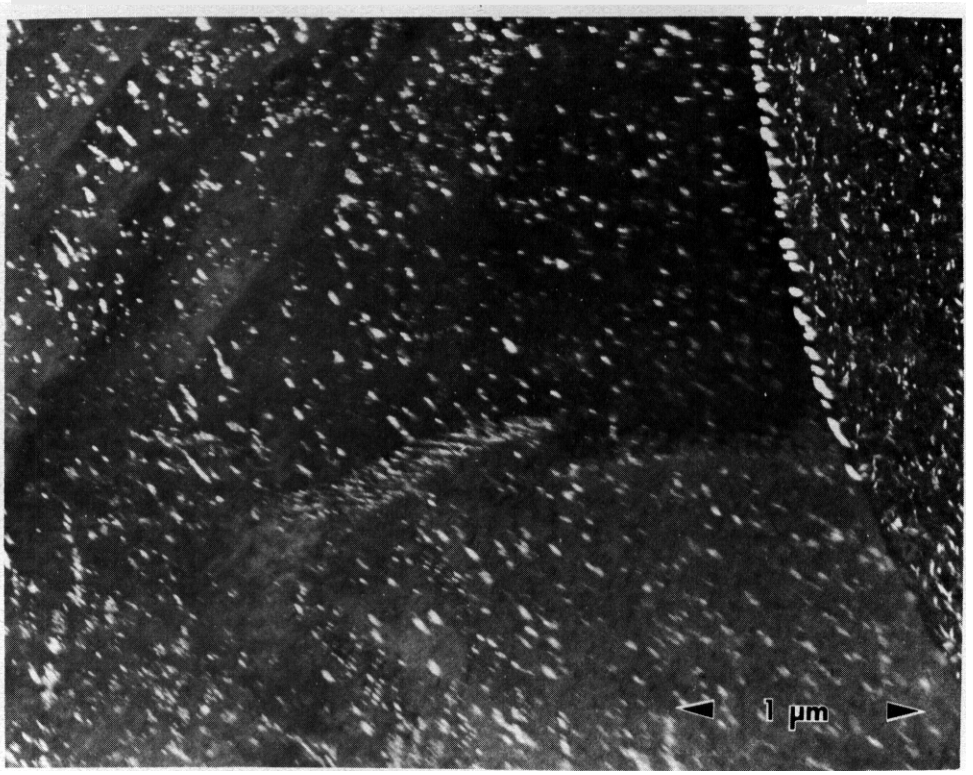

Fig. 5.3.3 Darkfield Electron Micrograph Showing Beta Precipitates in Irradiated Duplex Annealed Ti-6Al-4V.

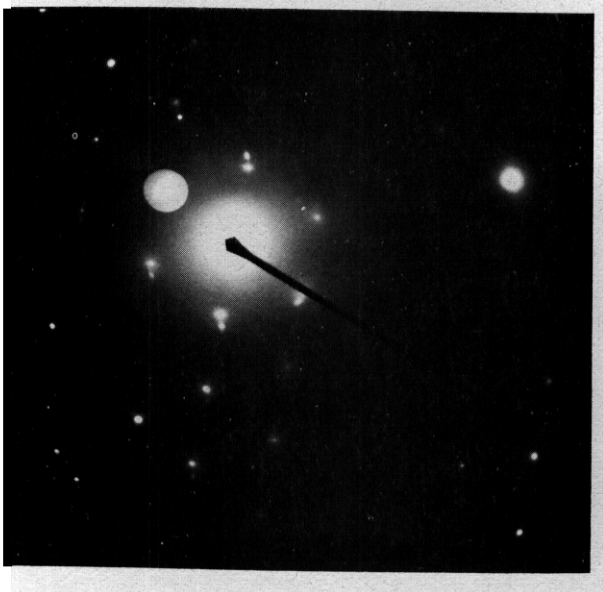

(a) SAD pattern

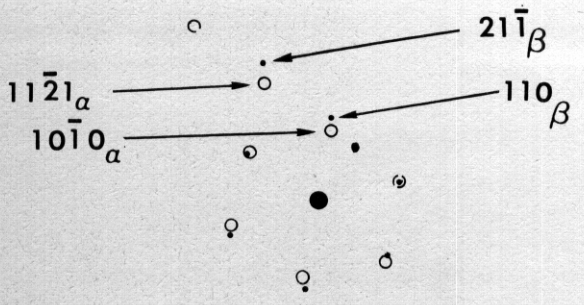

(b) schematic of indexed pattern

Fig. 5.3.4 Selected Area Diffraction (SAD) Pattern of Matrix and Beta Precipitates in Irradiated Duplex Annealed Ti-6Al-4V.

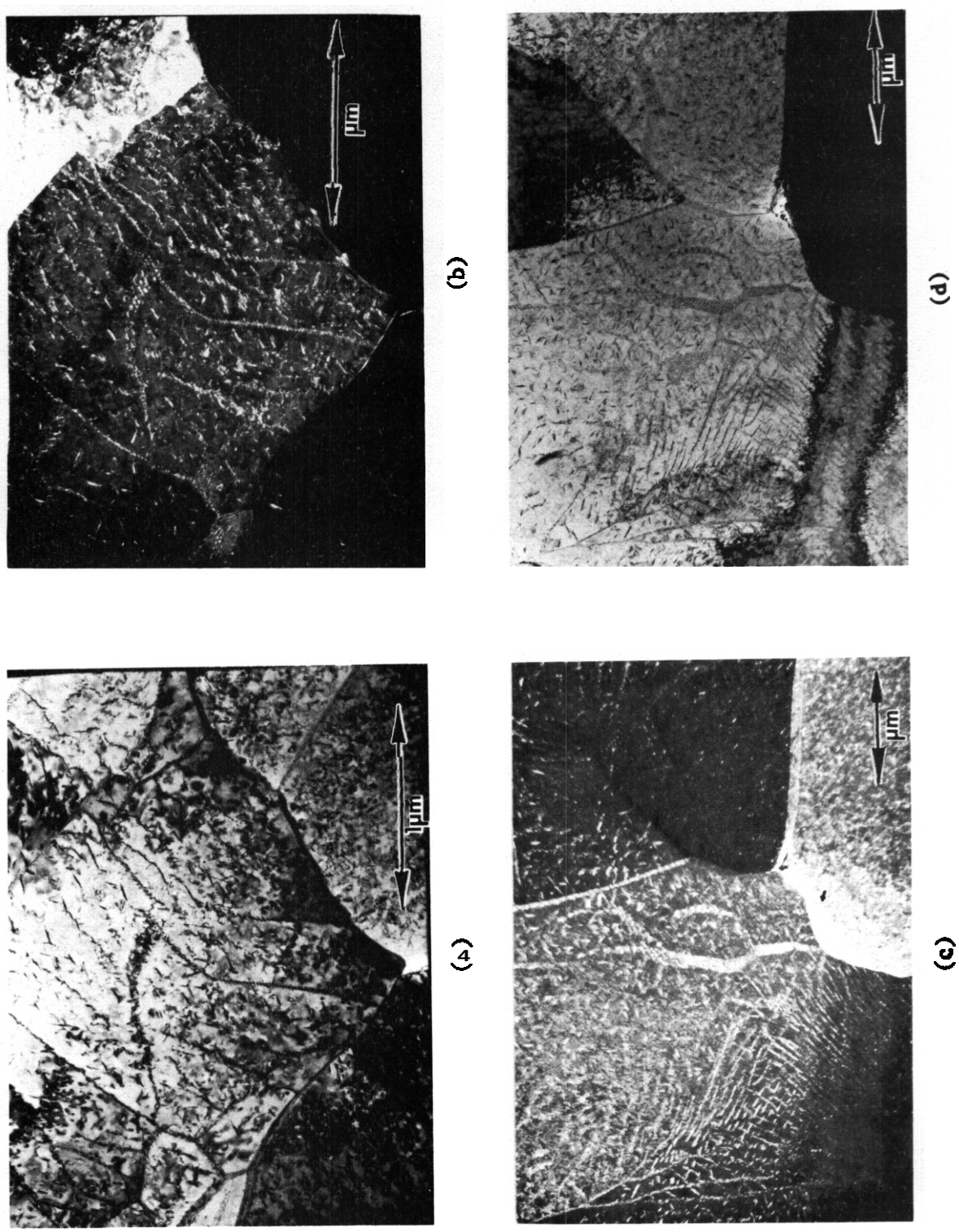

Fig. 5.3.6 Preferential Precipitation of Beta on Dislocations. Low Angle Boundaries, and Grain Boundaries. Figures (a) and (c) are bright field images and (b) and (d) are dark field images.

o Post-Irradiation Microstructures in Duplex Annealed Ti-5621s

The main features of defect structure in irradiated Ti-5621s alloy are a high density of dislocation loops and c + a dislocations. In contrast to the extensive beta precipitation in Ti-6Al-4V, there was no indication of beta-precipitation in the near alpha Ti-5621s alloy. Figures 5.3.6a and 5.3.6b are the electron micrographs of unirradiated and irradiated Ti-56215 alloy. The high magnification micrograph in Figure 5.3.7 shows the details of dislocation loops and grown in dislocation networks. The nature of the dislocation loops is currently being investigated by standard contrast experiments under 'two-beams' conditions. Contrast experiments coupled with the 'line of contrast criterion' of Thomas and Bell[2] and the 'black and white vector orientation criterion' of Wilkens[3] and Ruhle[4] are used to characterize and identify small defect configurations. Preliminary results from contrast experiments indicate that majority of the loops have $a/3 < 1120 >$ Burgers vector. Figure 5.3.8 taken with $g = (0002)$ (this rending all the $a/3 < 1130 >$ dislocation out of contrast) show nonbasal c + a type dislocations held up at small dislocation loops.

o Microhardness of Irradiated Alloys

The microhardness values of Ti-6Al-4V and Ti-5621s alloys in the unirradiated and irradiated conditions are shown in Table 5.3.1. The irradiation has resulted in significant increase in the hardness of the alloys. The increase in hardness as a result of irradiation is slightly higher in Ti-6Al-4V than in Ti-5621s probably due to the presence of fine beta precipitates in Ti-6Al-4V.

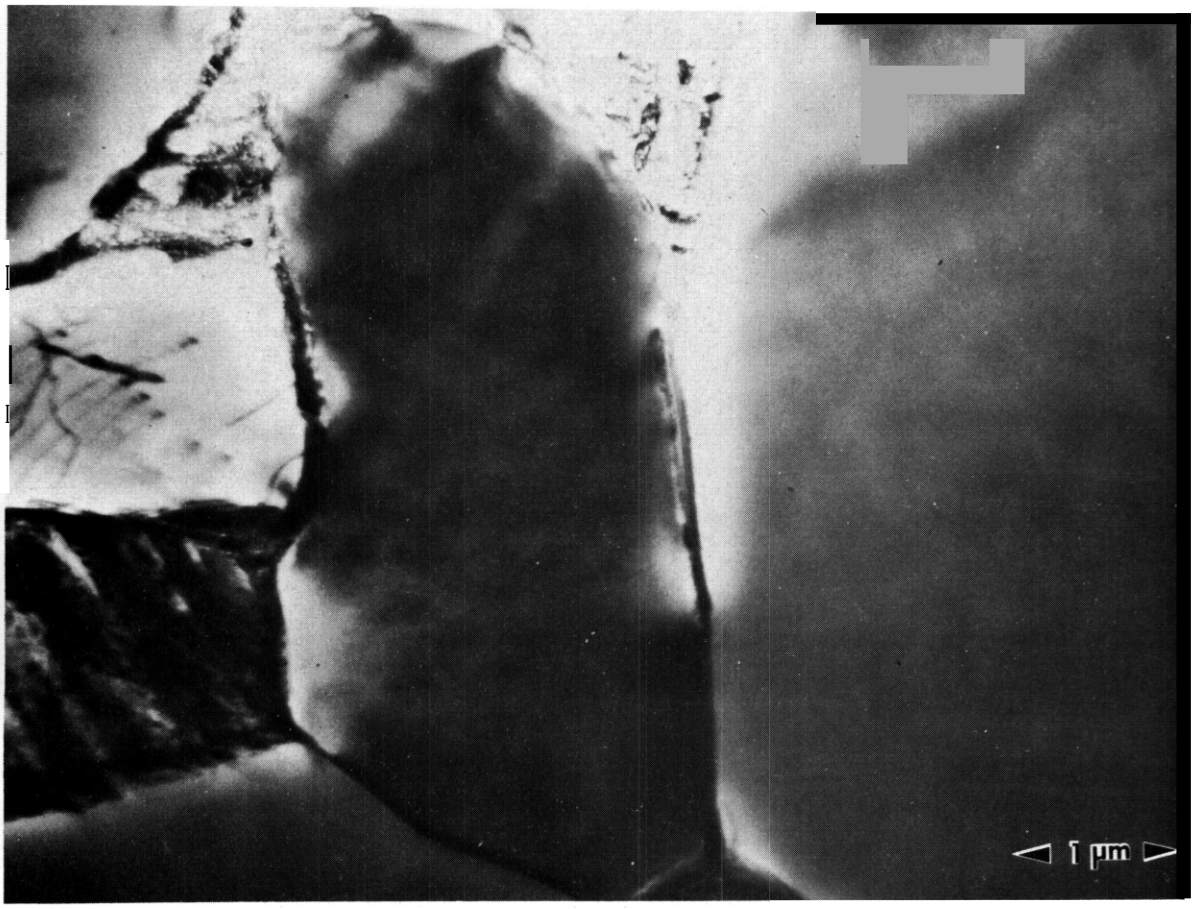

(a) Unirradiated

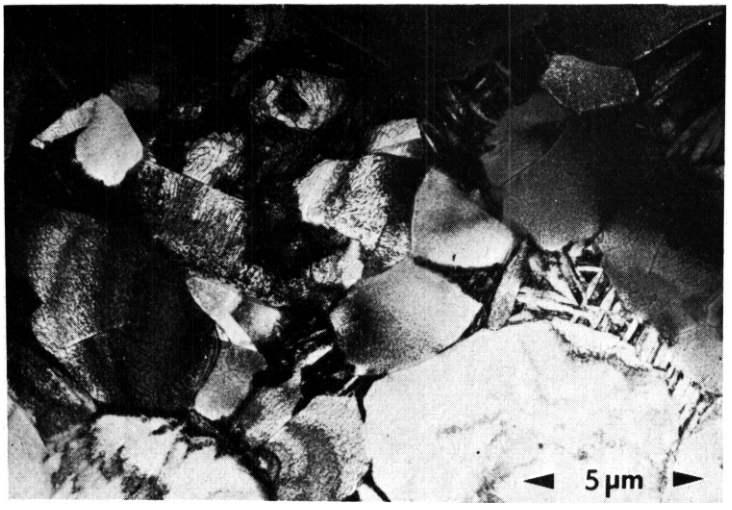

(b) Irradiated

Fig. 5.3.6 Microstructures of Ti-5621s

5.3.7 Dislocation Loops in Irradiated Ti-5621S

Fig. 5.3.8 Defect Microstructure in Irradiated Ti-5621S Imaged with g = *(0002)*.

TABLE 5.3.1

Microhardness of Unirradiated and Irradiated Titanium

Alloy	Microhardness (VHN)	
	Unirradiated	Irradiated
Ti-6A1-4V (mill annealed)	377	485
Ti-6A1-4V (duplex annealed)	320	435
Ti-5621s (duplex annealed)	380	446

5.3.5 Future Work

During the next reporting period the TEM studies of the irradiated Ti-6A1-4V in the duplex annealed condition and Ti-5621s allow will be completed. The effect of thermal treatments on the changes in microhardness and radiation damage microstructures in the two alloys will also be studied. Work will also be initiated on the remaining titanium alloys in this experiment, Ti-6A1-4V (beta anneal), Ti-62425, and Ti-15-3.

5.3.6 References

1. R. E. Nygren, Irradiation Induced Stress Relaxation in Titanium Alloys, Alloy Development for Irradiation Performance, Second Quarterly Progress Report, June 1978, Oak Ridge National Laboratory, pp 106–116.
2. G. Thomas and W. L. Bell, in Lattice Defects and Their Interaction (edited by R. R. Hasiguti), p. 478. Gordon and Breach, New York (1967).
3. M. Wilkens, in Modern Diffraction and Imaging Techniques in Materials Science (edited by S. Amelincky, R. Grevers, G. Remant and J. Van Landuyt), p. 233, North Holland, Amsterdam (1970).
4. M. Rühle, Phys. Status Solidi, 19, 263, 279 (1967).

ACKNOWLEDGEMENT

The authors would like to thank R. E. Nygren and R. W. Powell of HEDL for providing the specimens for this study.

5.4 EFFECT OF REACTOR CHAMBER ENVIRONMENT ON NIOBIUM ALLOYS - J. W. Davis (McDonnell Douglas Astronautics Company-St. Louis)

5.4.1 ADIP Task

Task Number I.A.3 - Perform Chemical and Metallurgical Compatibility Analysis.

5.4.2 Objective

Determine the reactor building environment necessary to protect niobium alloys from contamination.

5.4.3 Summary

Niobium, like the other group Vb refractory metals is sensitive to contamination from interstitial elements such as oxygen, nitrogen, carbon, and hydrogen. These elements, if present in sufficient quantities can significantly alter the tensile properties, reduce ductility, and raise the ductile-to-brittle transition temperature to well above room temperature. Therefore, particular attention must he paid to the operating environment of the refractory metals and the effects of that environment on mechanical properties.

Postulated reactor chamber atmospheres of inert gas or low quality vacuum appear to be unacceptable for niobium unless the residual gas pressures are extremely low. For example, for operating temperatures up to 600°C, the solubility of carbon and nitrogen is low, that of oxygen moderate and hydrogen very large. With the exception of hydrogen, increasing temperature raises the solid solubility of these elements. For the typical operating temperatures and pressures likely to he experienced by the refractory metal piping (i.e., ∿600°C and a chamber pressure of 10^{-3} torr) the equilibrium oxygen content of the niobium would be roughly 0.1 w/o which can cause embrittlement. In order to minimize this embrittlement, the oxygen level should be maintained below 0.04 w/o, which would require a vacuum on the order of 10^{-9} torr and a low leak rate.

5.4.4 Progress and Status

The properties, fabrication characteristics, and the serviceability

of the niobium base alloys and the refractory metals are greatly affected by the concentration of interstitial elements, i.e., carbon, oxygen, hydrogen, and nitrogen. Since niobium and its alloys have the ability to absorb interstitials at elevated temperatures, particular attention must be paid to their operating environment. For the plasma chamber side of the first wall and blanket structure of a fusion reactor this environment will likely be a hydrogen partial pressure of 10^{-3} to 10^{-6} torr. However, outside of this region the operating environment is less clear. For example, many of the designs that have proposed using refractory metals use an inert atmosphere, normally argon in the containment building. However, the presence of trace impurities in the argon, over a period of time can embrittle the niobium either by reducing ductility or altering the ductile-to-brittle transition temperature.

The solid solubility of the various interstitials in niobium varies considerably with temperature. This trend is seen in Figure *5.4.1*. Over the temperature range of 200-600°C, both carbon and nitrogen have very limited solubility <0.1 a/o (0.014 w/o), oxygen has slightly more <0.6 a/o (0.1 w/o), while hydrogen has very large solubility ~10 a/o (0.1 w/o). The equilibrium concentration, however, is affected by temperature and pressure. For hydrogen pressures of 10^{-3} torr or less, the equilibrium concentration at 600°C would be 0.01 a/o (<0.0001 w/o). Hydrogen concentrations of this level or even an order of magnitude higher is not enough to embrittle niobium alloys. This is not the case for the other interstitials, especially oxygen. For oxygen and pure niobium there are essentially no thermodynamic equilibrium states that can be attained even under high vacuum conditions. This can be seen in Figure *5.4.2* which indicates that the gas pressure would have to be kept below 10^{-22} torr to prevent oxide formation. As a result oxygen will be absorbed in a fusion reactor vacuum of $<10^{-6}$ torr and the amount of oxygen taken up will be equal to the solubility limit. For pure niobium at 600°C an an oxygen partial pressure of 10^{-6} torr, the equilibrium oxygen concentration would be approximately 600 wppm. This amount of oxygen is enough to alter the properties of pure niobium.

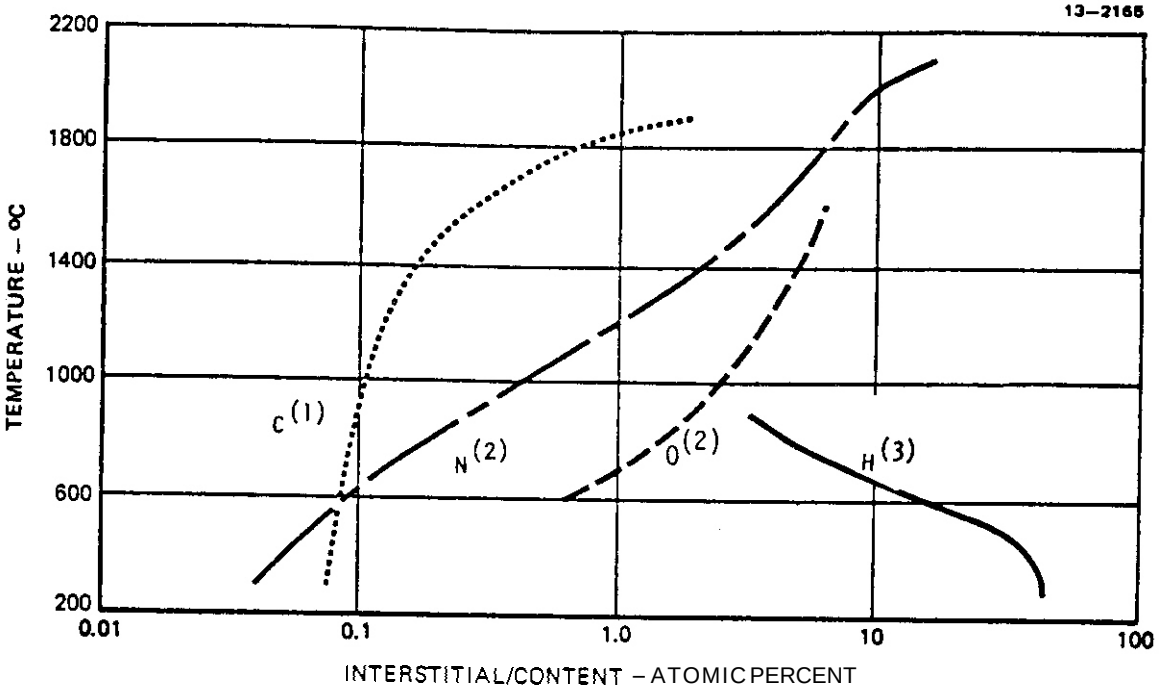

Fig. 5.4.1 Solubility of Interstitials in Niobium as a Function of Temperature (Gases at Atmospheric Pressure).

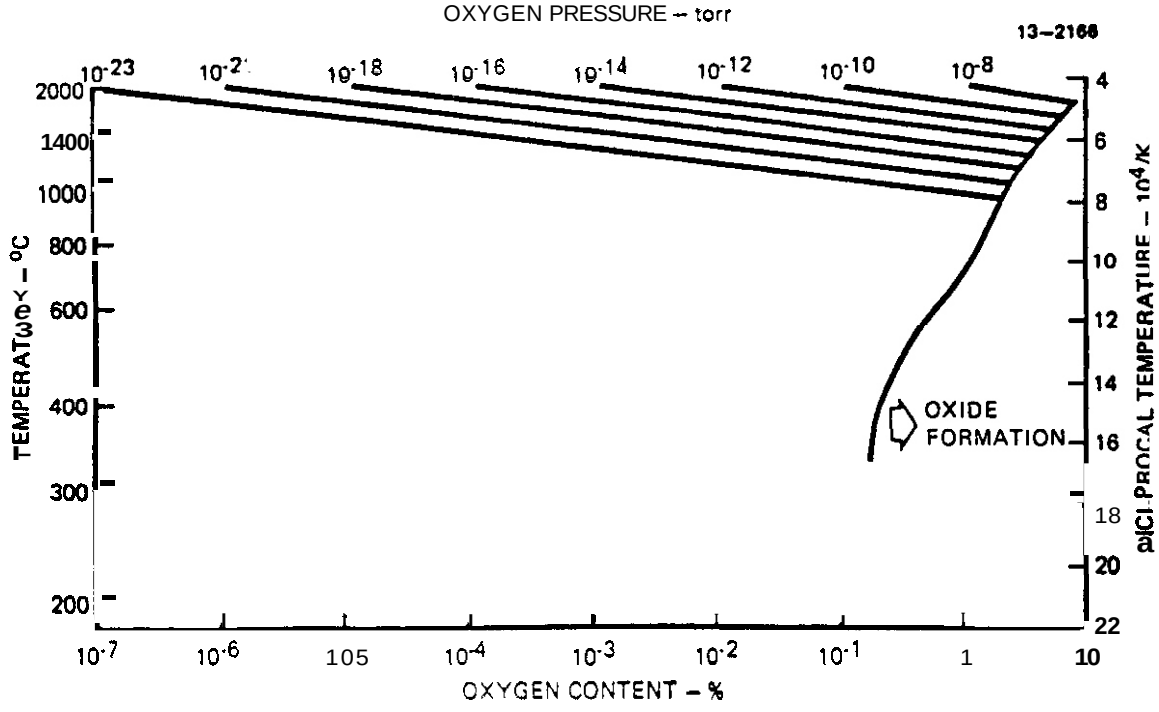

Fig. 5.4.2 Equilibrium Pressure, Temperature, and Concentration Relations for the Niobium-Oxygen System.

The use of reactive alloying elements (Hf, Ti, and Zr), in niobium tends to lower the oxygen solubility since their free energies of formation are much higher than those of niobium. The reactions with zirconium are of particular interest because zirconium is an effective strengthener of niobium. Zirconium additions to niobium have the effect of lowering the apparent oxygen solubility limit but increasing the nitrogen solubility limit. This increase is roughly a factor of 4 for a given temperature and pressure. Since zirconium additions lower the apparent solubility limit for oxygen in niobium it is likely that the gas metal interaction for a given temperature and pressure will result in the precipitation of a second phase. Therefore, it is likely that the precipitation of zirconium oxide within niobium will be at a rate equal to the rate of oxygen pick-up.

5.4.5 Conclusions

Because of the high reactivity of niobium alloys, it will be necessary to maintain very low oxygen and nitrogen pressures to minimize contamination. Operation of pure niobium in a vacuum of 10^{-8} torr, even with a low leak rate, appears to be marginally acceptable with respect to oxygen or nitrogen contamination and as a result the vacuum may have to be lowered to 10^{-9} torr. The use of alloys particularly those containing large amounts of reactive metal additions will be more tolerant of oxygen than pure niobium. However, they will still have a high vacuum requirement which will be a function of temperature, pressure and time. This limit remains to be determined.

5.4.6 References

1. Elliot, R. P.: "Constitution of Binary Alloys, First Supplement," McGraw-Hill, 1965.
2. Shunk, F. A.: "Constitution of Binary Alloys, Second Supplement, McGraw-Hill, 1969.
3. Mueller, W. M.; Blackledge, J. P.; and Libowitz, G. C.: Metal Hydrides, Academic Press, 1968.

5.5 THE DUCTILITY IN BENDING OF MOLYBDENUM ALLOYS IRRADIATED BETWEEN 425 AND 1000°C — B. L. Cox and F. W. Wiffen (ORNL)

5.5.1 ADIP Task

ADIP Task I.B.15, Tensile Properties of Reactive/Refractory Alloys.

5.5.2 Objectives

This work was directed at obtaining some measurement of the effect of elevated-temperature irradiation on the postirradiation mechanical properties of molybdenum and molybdenum-base alloys. Bend tests of small tab specimens were conducted over a range of test temperatures. Ductile-to-brittle transition temperatures (DBTT) were defined by the break or bend behavior in the test. Further refinement was provided by scanning electron microscopy of fracture surfaces on broken or cracked specimens.

5.5.3 Summary

Samples of Mo, Mo—0.5% Ti, and TZM (Mo—0.5% Ti—0.09% Zr), initially fully recrystallized, were irradiated in the EBR-II to fluences of 2.5×10^{26} n/m^2 (>0.1 MeV) in the range 425 to 1000°C. Rectangular coupons 3 × 2.8 × 0.4 mm were electropolished and then tested in vacuum in slow three-point bending from 22 to 650°C. The DBTT was bracketed by establishing the shift from failure in bending to full 45° bend under load.

Major findings were: (1) The three materials show similar behavior. (2) The DBTT is a strong function of the irradiation temperature, with the greatest degradation of behavior produced at 585°C. (3) Brittle failures in molybdenum contain a large surface fraction of exposed grain boundaries, from grain boundary separation. The balance of the surface is covered by cleavage facets. In the two alloys, the cleavage facets are the predominant surface feature, but a component of grain boundary separation is still present. (4) The fraction of grain boundary separation increases as the test temperature approaches the DBTT, but ductile tearing is observed above the DBTT.

5.5.4 Progress and Status

A recent review of the available literature on the effects of irradiation on the properties of molybdenum alloys[1] highlighted the scarcity of data on the effects of elevated-temperature, high-fluence irradiation. In the particular case of the UWMAK-III design, data were insufficient to predict the service behavior of TZM alloy in the temperature range 600 to 1000°C, for neutron fluences of 2×10^{26} n/m^2 and higher. A major concern was the ductility and the DBTT after service under these conditions.

Extra material from a set of samples previously used for microstructural characterization[2] was available. Techniques were developed to test these specimens in bending at elevated temperatures to obtain a fracture-appearance measure of the DBTT in slow bends.

5.5.4.1 Experiments

Fully annealed sheet specimens of Mo, Mo—0.5% Ti, and TZM, 0.38 mm (0.015 in.) thick, were irradiated in the EBR-II. Limited composition and final heat treatment conditions are given in Table 5.5.1, and irradiation parameters for the experiment are in Table 5.5.2. The samples had previously been cut to produce rectangular tabs suitable for electron microscopy, with a size of 2.8 by 3.1 mm (0.11 by 0.12 in.), so tests had to be developed that would utilize this material.

Table 5.5.1. Materials Parameters for Molybdenum-Base Alloys

Material	Alloy Additions (wt %)	Content, wt ppm			Annealing[a] Temperature (°C)
		C	O	N	
Mo		30	20	<5	1200
Mo—0.5% Ti	0.5% Ti	230	12	<5	1400
TZM	0.5% Ti, 0.09% Zr	230	20	<5	1500

[a] 1 h in vacuum.

Table 5.5.2. Irradiation Parameters for the Row 2 EBR-II Reactor Exposure[a]

Irradiation Temperature				Fluence, >0.1 MeV (n/m^2)	Displacement Damage Level (dpa)
Nominal		Uncertainty[b] (°C)	Range During Irradiation (°C)		
(°C)	T/T_m				
425	0.24	±10		2.5×10^{26}	11
585	0.30	±20		2.5	11
790	0.37	±25		2.5	11
1000	0.44	+30	950–1050	4.4	19

[a]Irradiation in reactor experiment X-034.

[b]Due to uncertainty in nuclear heating rate at experiment location in the reactor.

Ductility was determined in three-point bending, to a maximum of 45". The contact points were 0.51-mm-diam (0.020 in.) tungsten wire with a span of 2.03 mm (0.080 in.). The experimental setup is shown schematically in Fig. 5.5.1. This equipment was mounted on an Instron

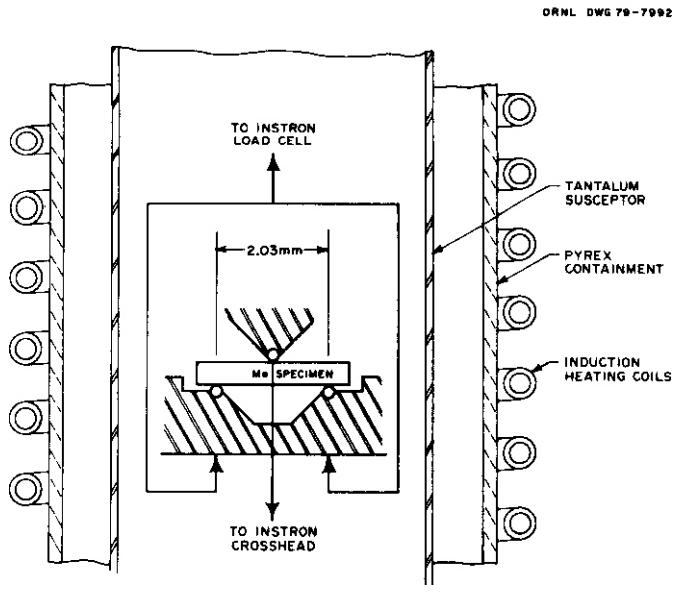

Fig. 5.5.1. Schematic Representation of the Elevated-Temperature Three-Point Bend Test Fixture. Tungsten wire segments were used for the bearing points.

tensile test machine, and most tests were made at *8.5* μm/s *(0.02* in./min). Thermocouple-controlled induction heating was used to achieve specimen temperatures in the range from *22* to 700°C, in a vacuum of **3** mPa (2×10^{-5} torr). Load-elongation curves were also recorded.

The DBTT was determined as the temperature boundary between tests in which specimens broke or cracked, and tests in which the specimens bent without cracking.

The failure mode was determined by scanning electron microscopy of the fracture surface. This also helped refine the location of the DBTT.

5.5.4.3 Results

Bend specimens break or crack when brittle, but may crack and finally bend 45° if they are tested at or above the DBTT. However, cracking is not conclusive evidence of the DBTT, so scanning electron microscopy (SEM) of the fracture surface is used to confirm the failure mode. In some of these cases, the SEM showed regions of ductile dimple fracture. This is intepreted as evidence that the sample had some very limited ductility, with the limited ductile tearing preceding the final brittle fracture propagation.

The bend test results, with indication of the SEM findings, are summarized in Fig. *5.5.2.* Several important observations can be drawn from these results:

1. Differences in the behavior of the three materials are small.
2. The DBTT is a strong function of the irradiation temperature.
3. For the available irradiation temperatures, the greatest degradation of properties was produced by the *585°C* irradiation.
4. For all four irradiation temperatures, and for all three materials, the DBTT is above room temperature.

Also, a number of observations were drawn from the SEM of the fracture surfaces. The fracture appearance changes from cleavage to grain boundary separation and finally to ductile tearing as the temperature is increased from below to above the DBTT. Figure *5.5.3* demonstrates this change from cleavage to ductile tearing in Mo—0.5% Ti. The failure

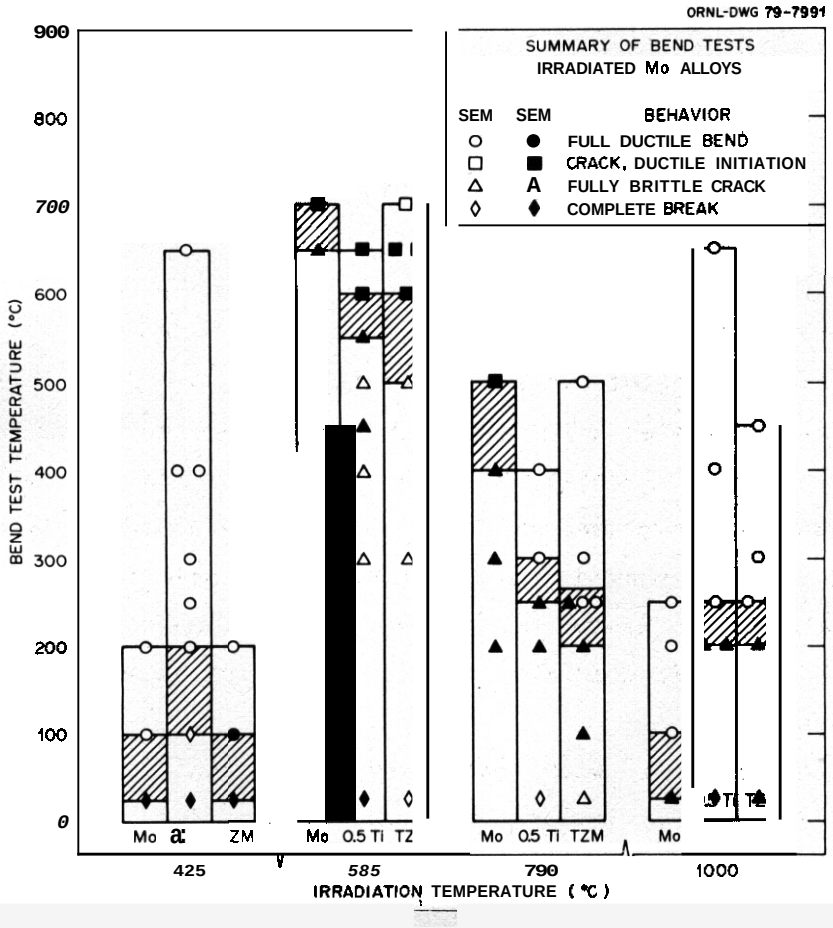

Fig. 5.5.2. Summary Compilation of all the Bend Test Results for Three Molybdenum Alloys Irradiated at Four Irradiation Temperatures. Open symbols indicate behavior determined by macroexamination only; filled symbols indicate SEM of the fracture surface. The shaded zone contains the DBTT.

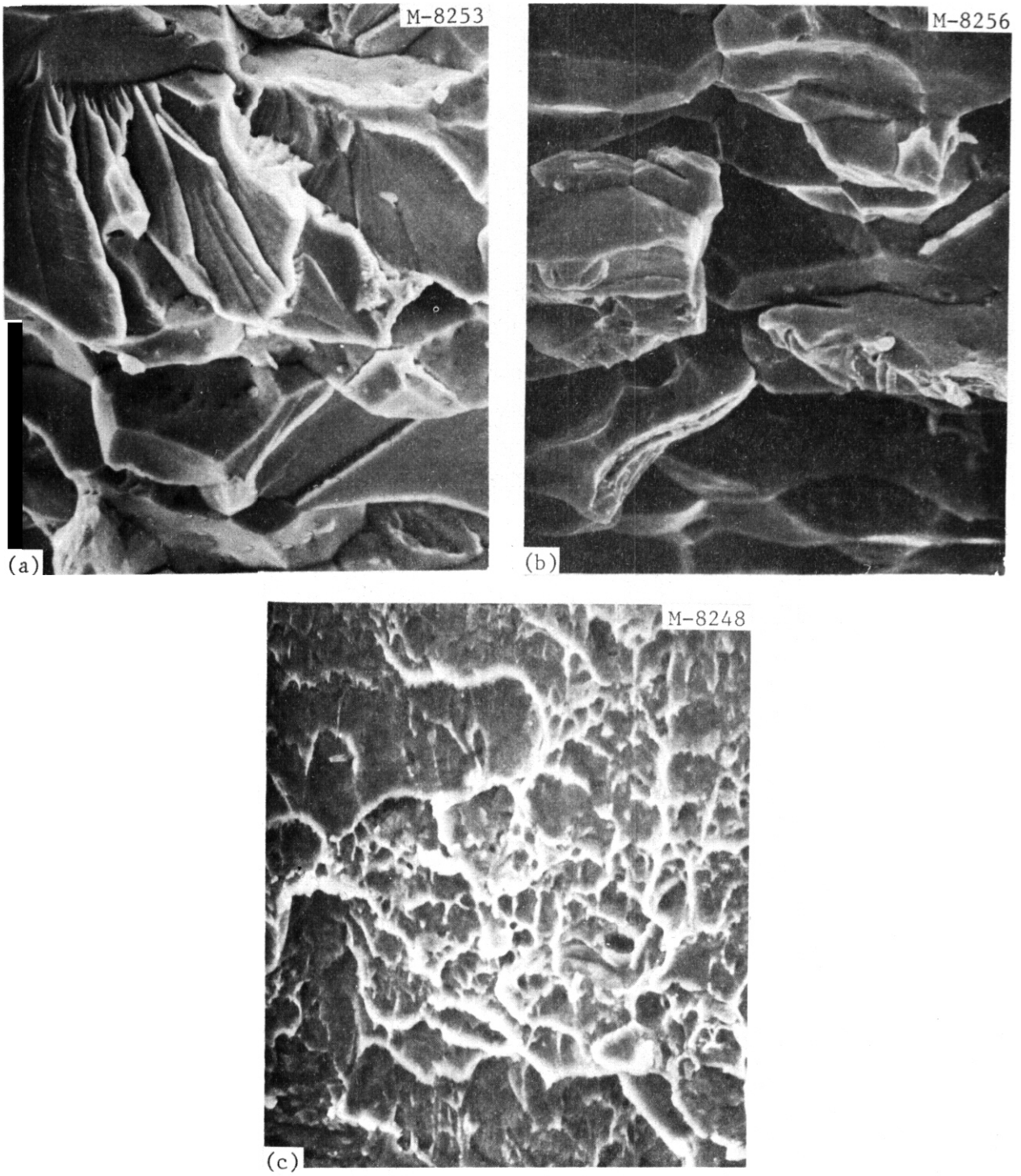

Fig. 5.5.3. Scanning Electron Microscope Fracture Surface Images for Specimens of Mo–0.5% Ti, Irradiated to 2.5 × 10^{26} n/m^2 (>0.1 MeV) at 585°C and Bend Tested to Failure at (a) 450, (b) 550, and (c) 650°C. 1000×.

mode can also change across the thickness of a specimen. For instance, ductile tearing near the tensile surface but cleavage facets deep in the crack are observed in Fig. 5.5.4, a TZM sample irradiated at 585°C and tested at 650°C.

Molybdenum generally shows more grain boundary separation than Mo–0.5% Ti or TZM when tested at the same temperature. Two examples illustrating this are given. In Fig. 5.5.5, fracture surfaces for the three alloys irradiated at 790°C and then tested at 200°C are shown. The sample set in Fig. 5.5.6 was irradiated at 1000°C and tested at 22°C.

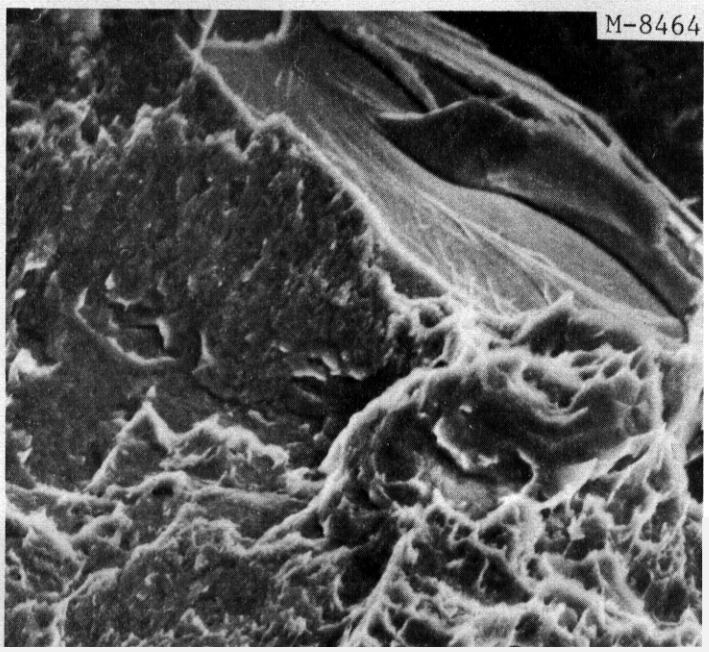

Fig. 5.5.4. Fracture Surface on a Sample of TZM Irradiated at 585°C and Bend Tested at 650°C. The tensile edge of the crack shows ductile dimple rupture, with a transition to cleavage fracture deep within the crack. 1000×.

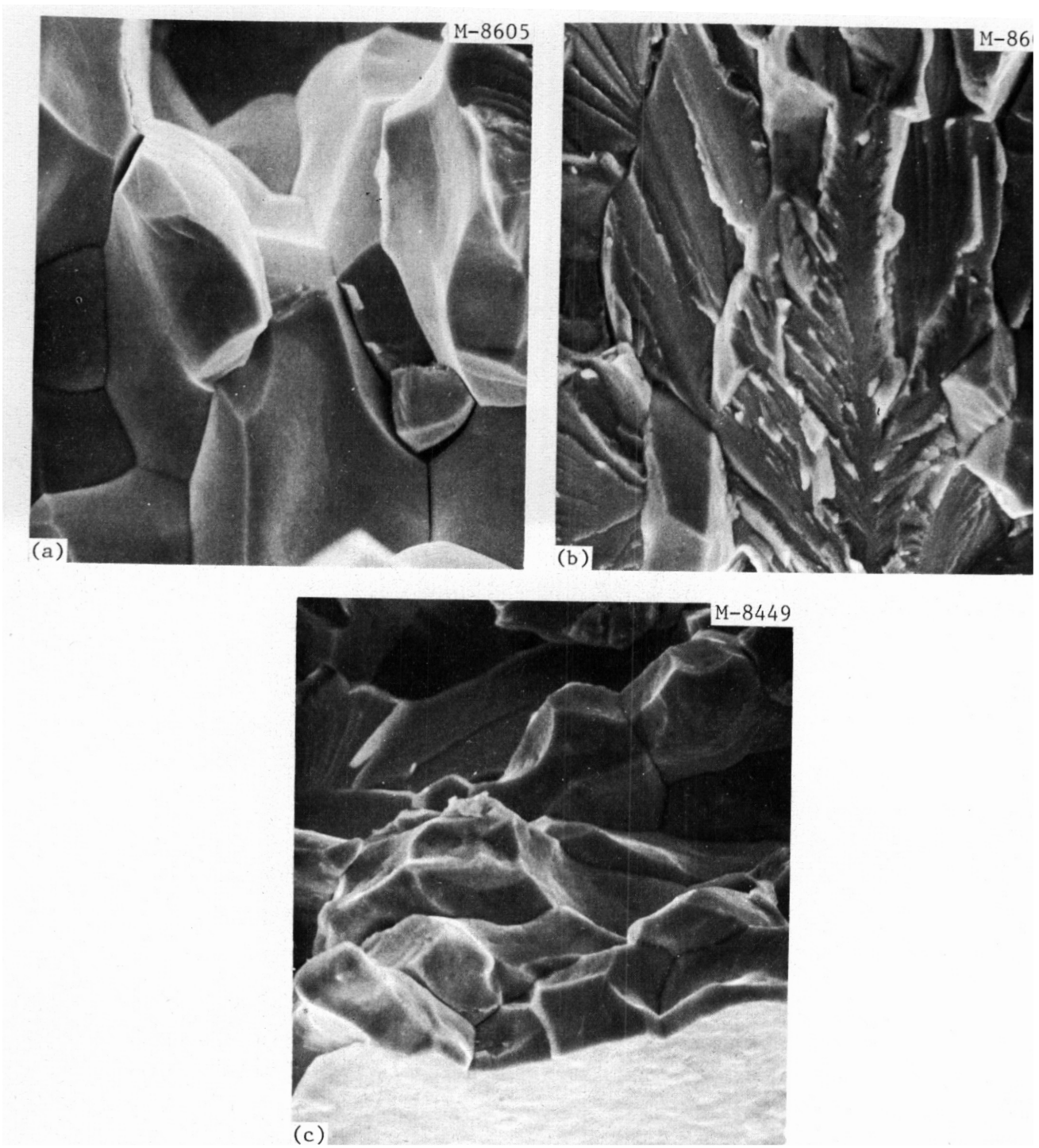

Fig. 5.5.5. The Fracture Mode Below the DBTT Depends Somewhat on Alloy. For samples irradiated at 790°C and tested at 200°C, Mo (a) shows much more grain boundary separation than does Mo—0.5% Ti (b) or TZM (c). The two alloys show mainly cleavage facets on the fracture surface, with less than 50% area coverage by grain boundaries. 1000×.

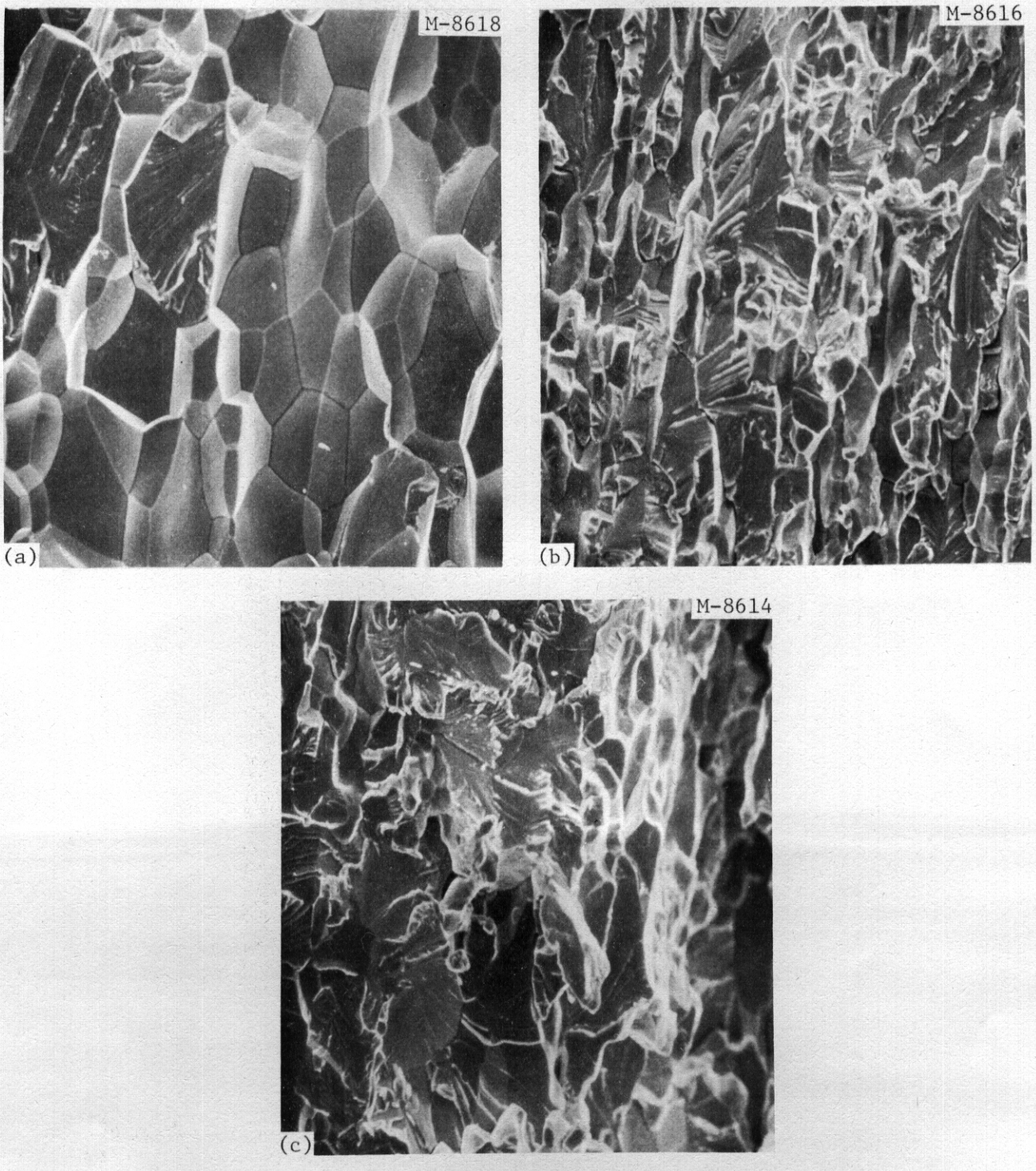

Fig. 5.5.6. Fracture Surfaces of (a) Mo, (b) Mo—0.5% Ti, and (c) TZM, Bend Tested at 22°C After Irradiation at 1000°C. 300×.

5.5.5 Future Work

This work will be concluded with an attempt to reduce the Instron output data to fracture stress values, and with a correlation of the observed mechanical properties and the previously reported microstructural characterization.' Comparison of these results with the small amount of literature data will also be deferred until the concluding report on this work.

5.5.6 References

1. B. Badger et al., *UWMAK-III, A Noncircular Tokamak Parer Reactor*, UWFDM-150, University of Wisconsin (July 1976), Chap. IX, Radiation Damage and Materials.
2. J. Bentley and F. W. Wiffen, "Neutron-Irradiation Effects on Molybdenum and Molybdenum Alloys," pp. 209-18 in *Proc. 2nd Top. Meet. Technol. Controlled Nucl. Fusion* (Sept. 21–23, 1976, Richland, Wash.), Vol. I, ed. by G. L. Kulcinski and N. M. Burleigh, CONF-760935 – Part 1.

6. PATH D ALLOY DEVELOPMENT — INNOVATIVE MATERIAL CONCEPTS

Innovative material concepts are included as a path in the alloy development program because the fusion reactor environment is extremely demanding on materials in the high-flux region and the more conventional materials and metallurgical concepts may not he adequate. Novel approaches to alloy design, nonconventional material processing to tailor properties, or alternate materials such as structural ceramics and fiber composites will he considered.

7. STATUS OF IRRADIATION EXPERIMENTS

Irradiation experiments are presently being conducted in the ORR and HFIR, which are mixed-spectrum fission reactors, and in the EBR-II, which is fast-spectrum reactor. Experiments are generally cooperative between several program participants. Experiment plans, test matrices, etc., are reviewed by the Alloy Development for Irradiation Performance Task Group.

7.1 IRKADIATION EXPERIMENT STATUS AND SCHEDULE

The following charts show the irradiation experiment schedule, including experiments completed, in progress, and planned. Experiments are presently under way in the ORR and HFIR, which are mixed-spectrum reactors, and the EBR-II, a fast reactor.

During this quarter irradiation of EBR-II subassembly X 287 was completed. The experiment has been received at ORNL and will be disassembled in the next quarter.

ORR-MFE-II was removed from the reactor on November 27 because a small pinhole leak developed in a weld in the experiment containment. Hardware necessary for remote repair of the weld was developed during December. Test welds and the actual weld repair should be accomplished in January 1979. While MFE-II is out of the reactor the planned dosimetry experiment will be conducted. This subassembly was previously assembled and was awaiting a convenient time for irradiation.

Irradiation started on HFIR-CTR-23 containing hourglass specimens of Nimonic PE-16.

Experiment HFIR-CTR-24 was removed from the reactor in December. Disassembly is complete. This experiment was basically a temperature calibration experiment, containing passive temperature monitors (melt wires, SiC, Mo for postirradiation recovery experiments). Evaluation is in progress.

Experiment Designation	Major Objective
A. Oak Ridge Research Reactor	
ORR-MFE-1	Experiments to scope the effects of composition and microstructure on the tensile, fatigue, and irradiation creep of representative path A, B, and C alloys.
ORR-MFE-2	
ORR-MFE-3	Effects of irradiation on postirradiation fatigue crack growth in representative path A, B, and C alloys.
ORR-MFE-4	Effect of irradiation on tensile, fatigue, and irradiation creep of path A PCA (Prime Candidate Alloy) and path B base research alloys. Spectral tailoring to maintain correct He/dpa ratio. Irradiation on continuing basis.

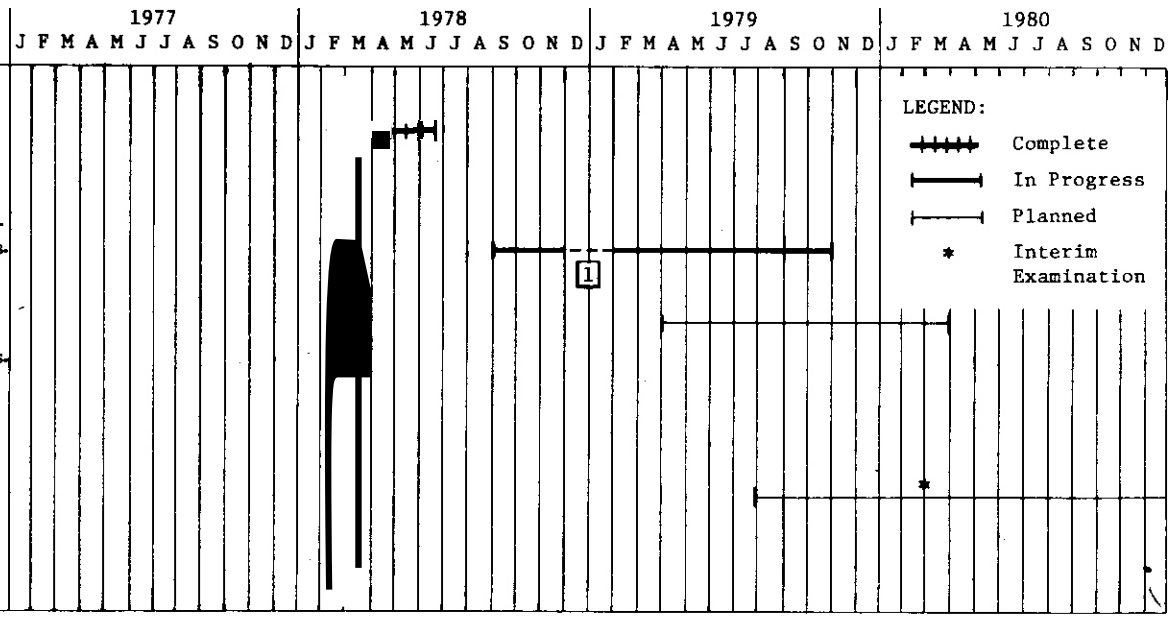

[1] MFE-2 was removed from the ORR on Nov. 29, 1978, to repair a small helium leak in the experiment containment. It is anticipated that the experiment will be reinstalled in the reactor during the latter part of February 1979. While the experiment is out of the reactor the dosimetry experiment will be performed with core configuration as with MFE-2.

Experiment Designation	Major Objective
ORR-MFE-5	In-reactor fatigue crack growth experiment
B. Experimental Breeder Reactor II	
Subassembly X 264	Effect of preinjected helium (2–200 at. ppm) on microstructure and tensile properties of 316 SS, PE-16, V and Nb alloys. Fluence $\leq 2.3 \times 10^{26}$ n/m^2, 500–825°C.
Subassembly X 287	Effect of preinjected helium (2–200 at. ppm He) on microstructure and tensile properties of 316 SS, PE-16, V and Nb alloys. Fluence $\leq 4 \times 10^{26}$ n/m^2, 400–700°C.
Subassembly X 217D	Stress relaxation Ti Alloys
See footnotes [1] [2] and [3]	Effect of irradiation on swelling, tensile, fatigue, and crack growth properties of Ti scoping alloys. 370, 450, and 550°C, position in reactor not finalized, therefore no fluence estimate.

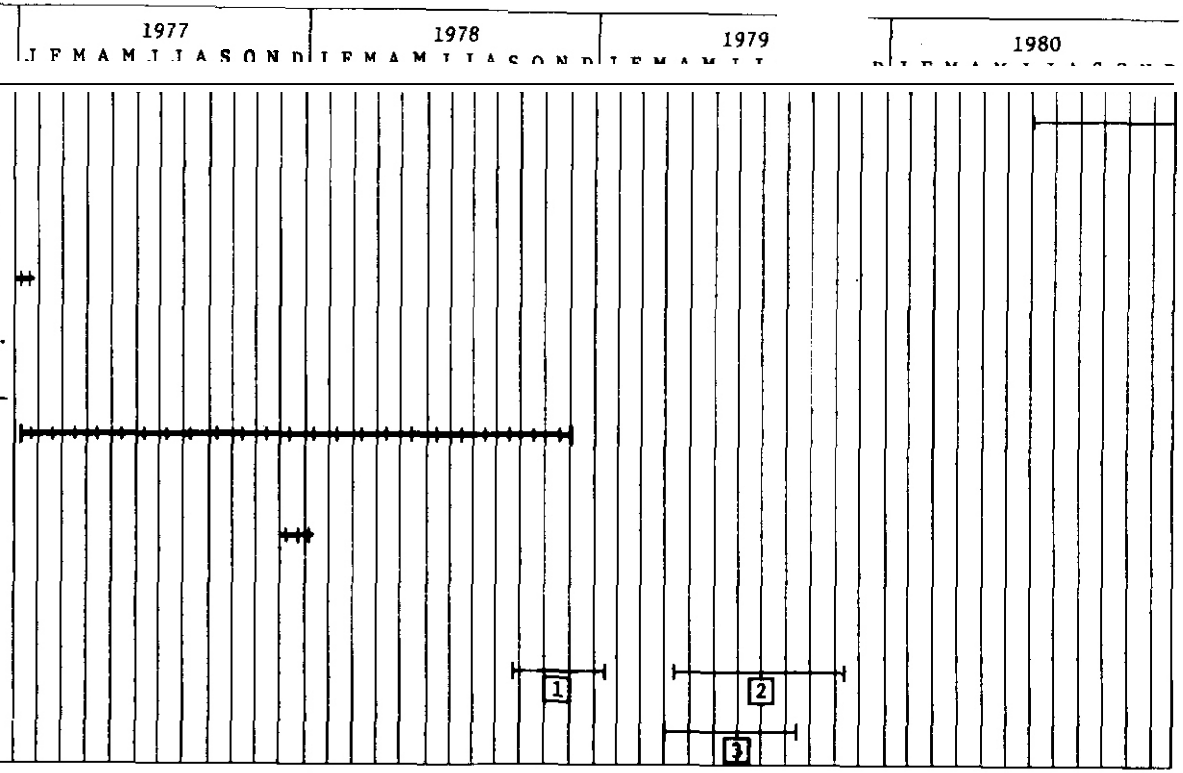

[1] EBR-II, row 2, pins 284, 285, and 286.

[2] EBR-II, row 2, pins 285 and 286.

[3] EBR-II, row 4, pin 284 reconstituted and irradiation continued in row 4.

Experiment Designation	Major Objective
Experiment plan depends on alloy availability. EBR-II space not yet identified.	Effect of Irradiation on swelling, tensile, fatigue, and crack growth properties of V and Nb scoping alloys. 370, 450, 550, and 650°C. Position in reactor not finalized, therefore no fluence estimate.
C. High Flux Isotope Reactor (HFIR)	
HFIR-CTR-4	PE-16 for swelling and tensile properties, 300–700°C 2.2–4.5 dpa, 100–350 at. ppm He
HFIR-CTR-7	PE-16 for swelling and tensile properties, 300–700°C 9–18 dpa, 1250–3000 at. ppm He
HFIR-CTR-8	duplicate of -7
HFIR-CTR-9	316 and 316 + Ti for swelling and tensile properties, 280–680°C, 9–18 dpa, 400–1000 at. ppm He

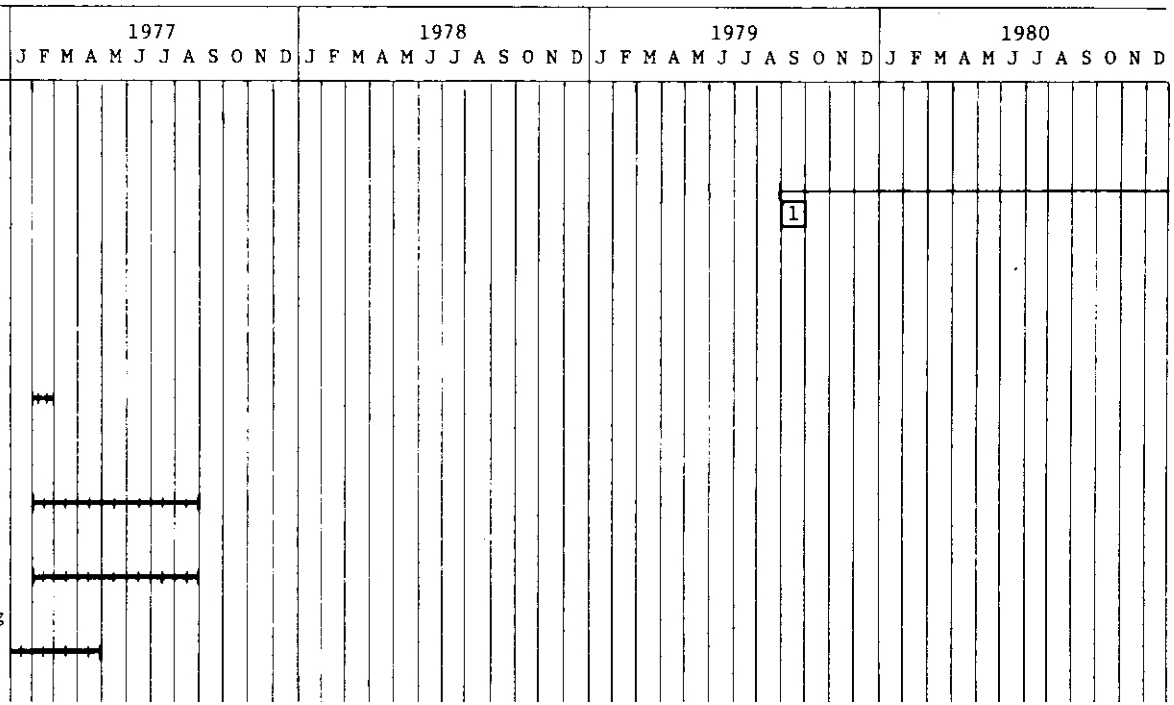

[1] Earliest date irradiations can begin on present alloy development schedule.

Experiment Designation	Major Objective
HFIR-CTR-10	duplicate of -9
HFIR-CTR-11	
HFIR-CTR-12	316 and 316 + Ti for swelling and tensile properties, 280–680°C, 5.5–11 dpa, 200–500 at. ppm He
HFIR-CTR-13	duplicate of -12
HFIR-CTR-14	20%-CW 316 for fatigue testing 300°C. 9–18 dpa, 400–1000 at. ppm He
HFIR-CTR-15	20%-CW 316 for fatigue testing 500°C, 5.5–11 dpa, 200–500 at. ppm He
HFIR-CTR-16	316, welds, PE-16, and Inconel 600 for swelling and tensile properties, ~55°C, 5.5–11 dpa, 150–2700 at. ppm He (depending on alloy)
HFIR-CTR-17	Type 316 welded with 16-8-2 filler metal for tensile properties and failure analysis, 280–620°C, 6.7–13 dpa, 180–460 at. ppm He in weld metal

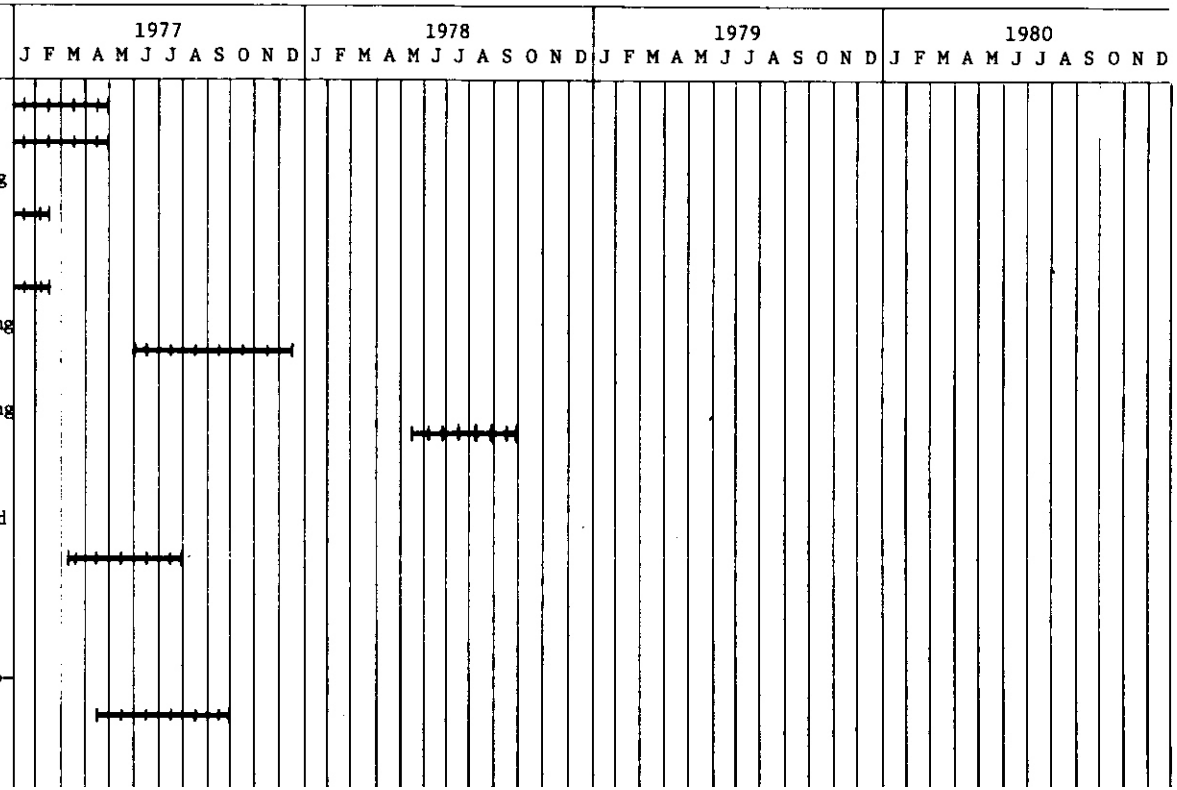

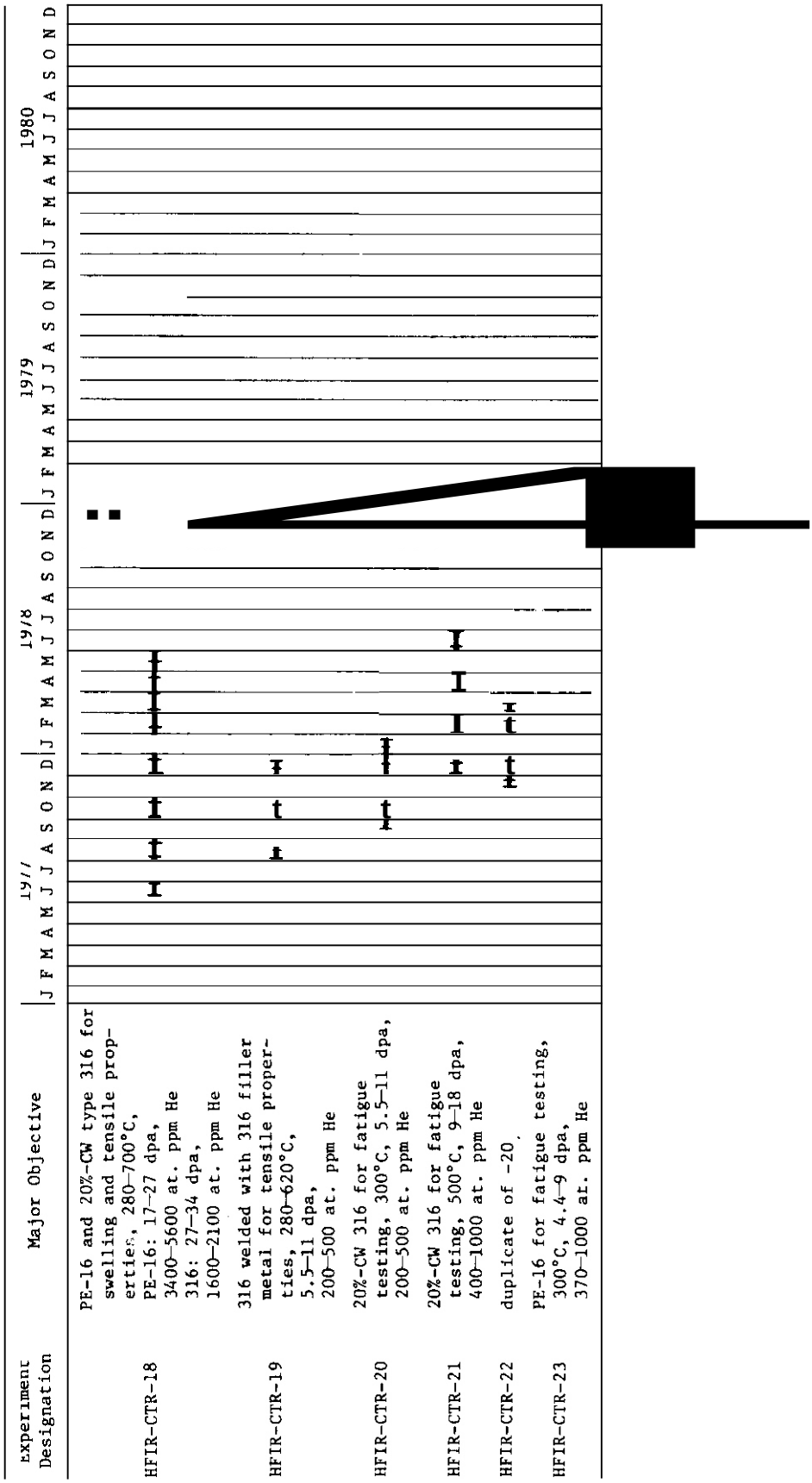
Experiment Designation
Major Objective
J F M A M J J A S O N D
1977
J F M A M J J A S O N D
1978
J F M A M J J A S O N D
1979
J F M A M J J A S O N D
1980
HFIR-CTR-18
PE-16 and 20%-CW type 316 for swelling and tensile properties, 280–700°C,
PE-16: 17–27 dpa, 3400–5600 at. ppm He
316: 27–34 dpa, 1600–2100 at. ppm He
HFIR-CTR-19
316 welded with 316 filler metal for tensile properties, 280–620°C, 5.5–11 dpa, 200–500 at. ppm He
HFIR-CTR-20
20%-CW 316 for fatigue testing, 300°C, 5.5–11 dpa, 200–500 at. ppm He
HFIR-CTR-21
20%-CW 316 for fatigue testing, 500°C, 9–18 dpa, 400–1000 at. ppm He
HFIR-CTR-22
duplicate of -20
HFIR-CTR-23
PE-16 for fatigue testing, 300°C, 4.4–9 dpa, 370–1000 at. ppm He

Experiment Designation	Major Objective
HFIR-CTR-24	Temperature calibration, tensile properties of MFE Ref. 316, 2.25 dpa, 30 at. ppm He
HFIR-CTR-25	Temperature calibration, tensile properties of MFE Ref. 316, 2.25 dpa, 30 at. ppm He
HFIR-CTR-26	Swelling and tensile properties of MFE Ref. 316, 32 dpa, 1900 at. ppm He
HFIR-CTR-27	Swelling and tensile properties of MFE Ref. 316, 56 dpa, 3450 at. ppm He
HFIR-CTR-28	Swelling and tensile properties of MFE Ref. 316, 32 dpa, 1900 at. ppm He
HFIR-CTR-29	Swelling and tensile properties of MFE Ref. 316, 56 dpa, 3450 at. ppm He
HFIR-CTR-30[a]	Swelling and tensile properties, Path A PCA microstructural variations, 40 dpa, 2500 at. ppm He
HFIR-CTR-31[b]	Swelling and tensile properties, Path B PCA microstructural variations

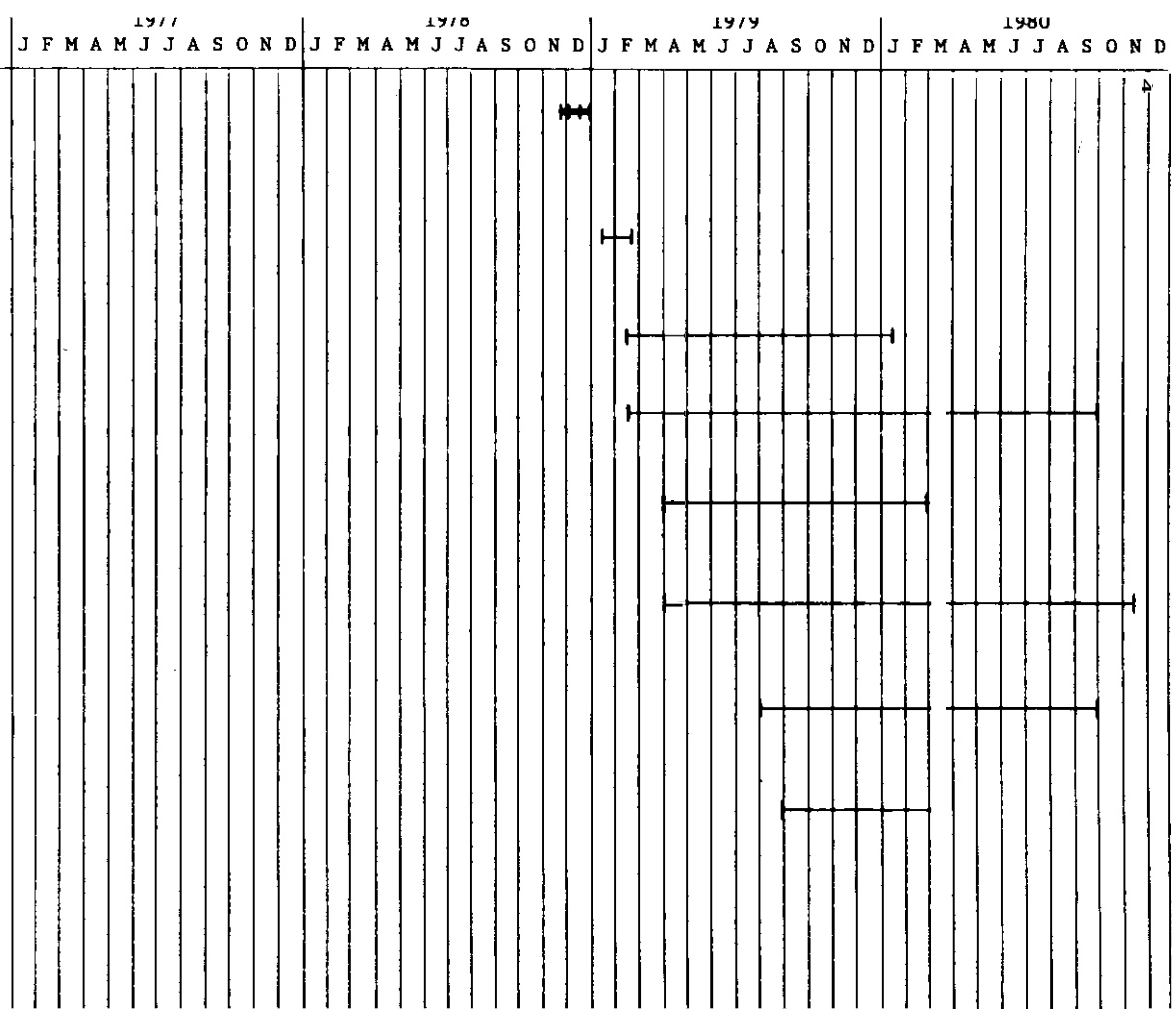

[a]Assumed 18 cycles for planning.

[b]Assumed 8 cycles for planning.

7.2 ETM RESEARCH MATERIALS INVENTORY — F. W. Wiffen, T. K. Roche, E. E. Bloom (ORNL), and J. W. Davis (McDonnell Douglas)

7.2.1 ADIP Task

ADIP Task I.D.1, Materials Stockpile for MFE Programs.

7.2.2 Purpose and Scope

The Office of Fusion Energy (ETM) of the Department of Energy has assigned program responsibility to ORNL for the establishment and operation of a central inventory of research materials to be used in the Fusion Reactor Materials research and development programs of the DOE. The primary objective is to provide a common supply of materials for use in the nationally coordinated Fusion Reactor Materials Program. This will minimize unintended materials variables, and provide for economy in procurement and for centralized recordkeeping. Initially this inventory is to focus on materials related to first wall and structural applications and related research, but various special-purpose materials may be added in the future. It is recognized that materials supplementary to this inventory will be introduced to the ETM programs from time to time, and records of those materials shall be made available to ORNL and incorporated in the records of the ETM Research Materials Inventory.

The use of materials from this inventory for research that is coordinated with or otherwise related technically to the Fusion Reactor Materials Program of DOE but which is not an integral or directly funded part of it is encouraged, with the understanding that the results of such research be made available to the Fusion Reactor Materials Program.

7.2.3 Materials Requests and Release

Materials requests must provide a statement of the programmatic end use and agreement that characterization information developed by the user shall be supplied to the inventory records. Requests for materials shall be directed to ETM Research Materials Inventory at ORNL (Attention: F. W. Wiffen). Materials will be released directly if:

(a) The material is to be used for programs funded by ETM, with goals consistent with the approved Materials Program Plans of the Materials and Radiation Effects Branch.

(b) The requested amount of material is available, without compromising other intended uses.

Materials requests that do not satisfy both (a) and (b) will be discussed with the staff of the Materials and Radiation Effects Branch, Office of Fusion Energy, for agreement on action.

7.2.4 Records

Chemistry and materials preparation records are maintained for all inventory material. All materials supplied to program users will be accompanied by summary characterization information.

7.2.5 *Summary* of Current Inventory (December 1978)

7.2.5.1 Path A Alloys

1. Reference alloy — 20%-cold-worked type 316 stainless steel. Sheet and rod are at ORNL now. 49 m (160 ft) of tubing, 4.57 mm OD by 0.25 mm wall (0.180 by 0.010 in.) was delivered to ORNL during the reporting period. Rework will be scheduled as required.
2. Prime Candidate Alloy (PCA) (Fe—16 Ni— 14 Cr—2 Mo—Mn, Ti, Si, C). An order for 1360 kg (3000 lb) of this alloy is being processed by the vendor. ORNL has received 420 kg (920 lb) of 100-mm-diam (4-in.) bar. Plate and sheet are to be delivered in February 1979.
3. PCA tube production and remelt for composition variation is planned for late FY 1979.

7.2.5.2 Path B Alloys

4. A reference heat of PE-16 is in stock at ORNL. Sheet and rod are available. During the reporting period, 24 m (80 ft) of tubing, 4.57 mm OD by 0.25 mm wall (0.180 by 0.010 in.), was delivered to ORNL. Rework will be scheduled as required.

5. Base Research Alloys

Alloy	Ni	Cr	Mo	Nb	Ti	Al	Si
B-1	25	10	1		3	1.5	0.3
B-2	40	12	3		1.5	1.5	0.3
B-3	30	12		2	2	0.5	0.3
B-4	40	12		3	1.8	0.3	0.3
B-6	75	15		1	2.5	1.5	0.3

An order was placed for two 140-kg (300-lb) heats of each alloy in 0.1 by 0.1-m (4 by 4-in.) bars. This material was delivered to ORNL in September 1978, and the yield was approximately 180 kg (400 lb) per alloy.

Secondary breakdown has been initiated. A single sheet bar and a rod have been extruded from each of the five alloys. These primary extrusions weigh approximately 7 kg (15 lb) each.

HEDL and ORNL are cooperating to determine the final fabrication and heat treatments to use in preparing these alloys for inclusion in the experimental program. These investigations are scheduled to be completed by March 1979.

7.2.5.3 Path C Alloys (Refractory Alloys)

6. Small amounts of several niobium- and vanadium-base alloys are currently available at ORNL. Quantity and product forms are limited.

7. An order has been placed for the purchase of approximately 6 kg each of five alloys. Only sheet and rod will be produced.

Alloys: Nb–1% Zr
Nb–5% Mo–1% Zr
V–20% Ti
V–15% Cr–5% Ti
V–9% Cr–3.3% Fe–1.3% Zr–0.05% C (Vanstar 7)

Delivery of material is expected in the late summer of 1979. As a preliminary step in preparation of the vanadium alloys, ORNL will size approximately 60 kg (130 lb) of vanadium melt stock by cold swaging to 25-mm-diam (1-in.) rod. The rod will be returned to the vendor in February 1979 for further treatment in preparation of electrodes for vacuum arc remelting.

7.2.5.4 Path C Alloys (Reactive Alloys)

8. The titanium-base scoping alloys have the following compositions, Wt %:

Alloy	Al	V	Mo	Zr	Sn	Cr	Si
Ti-64	6	4					
Ti-6242s	6		2	4	2		0.09
Ti-5621s	5		1	2	6		0.25
Ti-38644	3	8	4	4		6	

At least 0.75 m^2 (1200 $in.^2$) of each of these alloys is currently available in 0.76-mm (0.030-in.) thickness. This sheet is from the same heat as material currently in reactor experiments. Larger section sheet of alloy Ti-5621s is also available.

Orders are now being developed to purchase new stocks of each of these alloys, to provide all needed product forms from a single heat. Delivery dates have not yet been determined.

The titanium-base alloys are stored at McDonnell Douglas. However, inventory control and materials release are handled by ORNL, and requests should be addressed to ORNL.

8. CORROSION TESTING AND HYDROGEN PERMEATION STUDIES

Corrosion, erosion, and mass transfer are processes that may degrade mechanical properties, alter heat transfer characteristics of heat transport systems, and present maintenance problems when radioactive nuclides are involved. The importance of hydrogen permeation and the behavior of hydrogen in the alloy systems under development is clear from consideration of tritium inventory, containment, etc. In the early stages of the development program, base-line information is required to define compatible or noncompatible alloy systems and coolants. As optimized alloys are developed, more detailed data on effects of adjustments in alloy composition or structure may be required. Extensive engineering compatibility data will be required on the final optimized alloys.

8.1 CAPSULE TESTS OF TYPES 316 AND 316L STAINLESS STEEL IN NITROGEN-CONTAMINATED LITHIUM — P. F. Tortorelli and J. H. DeVan (ORNL)

8.1.1 ADIP Task

ADIP Task I.A.3, Perform Chemical and Metallurgical Compability Analyses.

8.1.2 Objective

The purpose of this program is to determine the chemical compatibility of iron-base alloys with metallic lithium. Structural steel specimens are exposed to static lithium containing selected solute additions to identify the kinetics and mechanisms that govern the corrosion of steels by lithium. Specific program objectives are (1) to determine the effects of N, C, H, and O on apparent solubilities of stainless steel components in lithium; (2) to determine the C and N partitioning coefficients between stainless steels and lithium; (3) to determine the effects of soluble (Ca, Al) and solid (Y, Zr, Ti) active metal additions on corrosion of stainless steels by lithium; and (4) to determine the tendencies for dissimilar-metal mass transfer between stainless steel and Mo, Nb, and Co.

8.1.3 Summary

The weight loss and surface attack of as-rolled and fully annealed type 316L stainless steel exposed to Li—2 wt % N differ little from previous data for fully annealed type 316 stainless steel. At 700°C, the as-rolled type 316L lost significantly more weight than similarly tested coupons of fully annealed type 316L stainless steel. Additionally, the time dependence of grain boundary penetration of type 316 stainless steel exposed to nitrogen-contaminated lithium at 600 and 700°C is related to the decreasing nitrogen concentration during testing.

8.1.4 Progress and Status

Previously we reported[1] that the rate of corrosion of as-rolled type 316L stainless steel in nitrogen-contaminated lithium was higher than that of fully annealed type 316. Additional experiments were

performed at 500, 600, and 700°C to determine whether the decreased corrosion resistance was due to differences in microstructure or alloy composition. The resulting weight loss data from fully annealed and as-rolled type 316L stainless steel, tested for 100 h, are given in Table 8.1.1, which also includes earlier data for fully annealed type 316 stainless steel. Unfortunately, there is considerable scatter in the weight loss data, which we now attribute to nonuniform distribution of the Li_3N in the lithium. Despite the scatter, there is still an apparent trend in the weight losses, which indicates a slightly higher corrosion rate for fully annealed type 316L than for annealed type 316 stainless steel with normal carbon concentration. The effect of cold work on weight loss can be seen by comparing the second and third columns in Table 8.1.1. There is no significant difference at 500°C, but at 700°C the weight losses of the as-rolled specimens are greater than those of the fully annealed type 316 stainless steel.

Table 8.1.1. Weight Losses of Types 316 and 316L Stainless Steel Exposed to Li–2 wt % N

Temperature (°C)	Weight Loss (g/m^2)		
	316 Fully Annealed[a]	316L Fully Annealed	316L As-Rolled
500	−20.7 ±18.2	−34.9	−37.0
600	−19.5 ±23.0	−0.8	−43.8
700	−22.4 ±12.8	−35.9 −31.8	−70.4 −52.3

[a]Average of three tests at both 500 and 600°C and four at 700°C.

Metallographic examination of the fully annealed type 316L specimens revealed the same types of attack previously reported for type 316 stainless steel; that is, a uniform reaction layer at 500°C

and intergranular attack at 600 and 700°C. The attack depths measured on the type 316L specimens were within the scatter of the reported[1] depths of exposed type 316 stainless steel. The structure of the as-rolled specimens was like that described in the last progress report[1] and is shown again in Fig. 8.1.1. The severity of the attack leads to heavy surface porosity and delamination, which give rise to the larger weight loss (see Table 8.1.1).

Y-156830

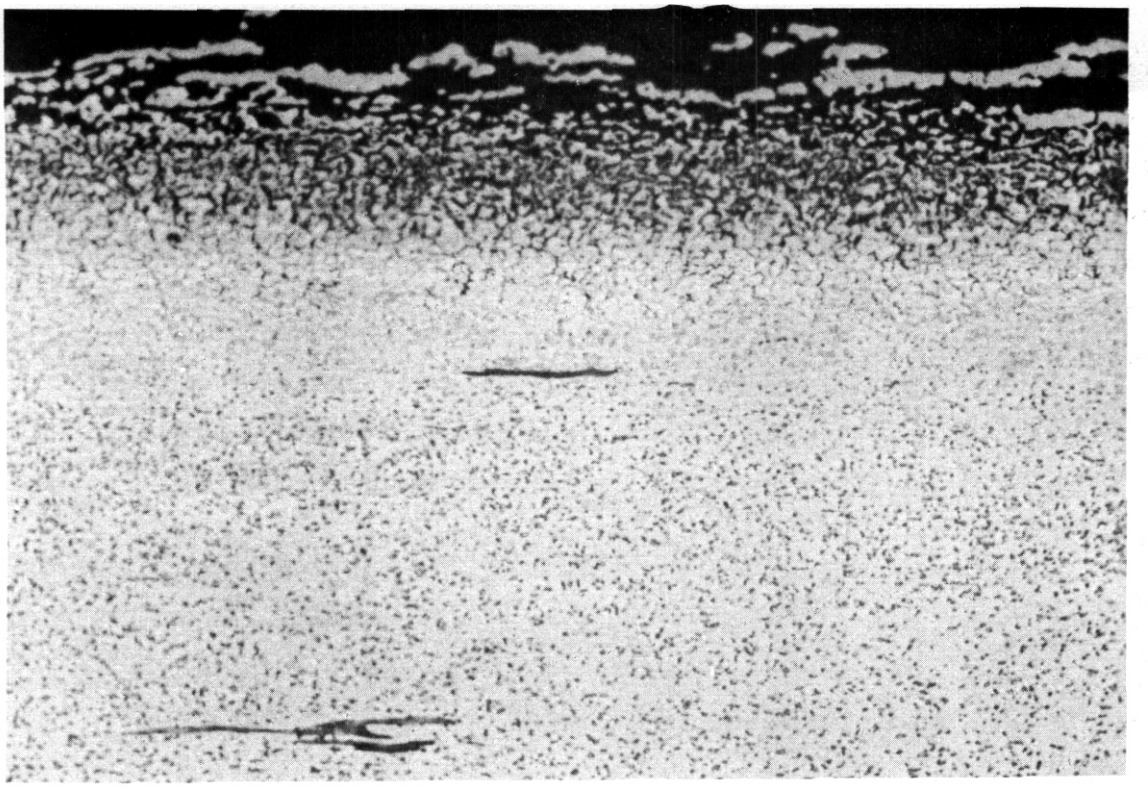

Fig. 8.1.1. As-Rolled Type 316L Stainless Steel Exposed to Li—2 wt % N for 100 h at 700°C. 500×.

The preceding progress report' showed that the weight losses and corrosion depths of type 316 stainless steel exposed to Li—2 wt % N decreased more rapidly with time than predicted by a $t^{1/2}$ law. This was qualitatively attributed to the decreasing nitrogen concentration of the lithium during a test. A model to describe these data has now been developed. It is based on the uptake of solute from solution.

The details of the calculations can be found in ref. 2. Briefly, existing empirical equations for weight loss and grain boundary penetration[3] were modified to account for the decrease in nitrogen concentration during testing due to its reaction with the stainless steel. Our grain boundary penetration measurements agreed well with the predictions of the derived equation for a test of time t (h) and temperature T (K):

$$X_g = [4 \times 10^3 A_0 t \exp(-15{,}600/T) \exp(-at)]^{1/2} , \qquad (1)$$

where A_0 is initial nitrogen concentration, a is a geometrical constant, and X_g is the depth of attack in micrometers,[2] respectively. However, this type of equation did not correlate with the measured weight changes. Equation (1) predicts that a plot of $\ln(X_g/t^{1/2})$ versus exposure time should be a straight line. Figure 8.1.2 is such a plot for our data and shows good straight-line fits at 600 and 700°C. However, the uniform attack distance observed at 500°C did not follow this behavior.

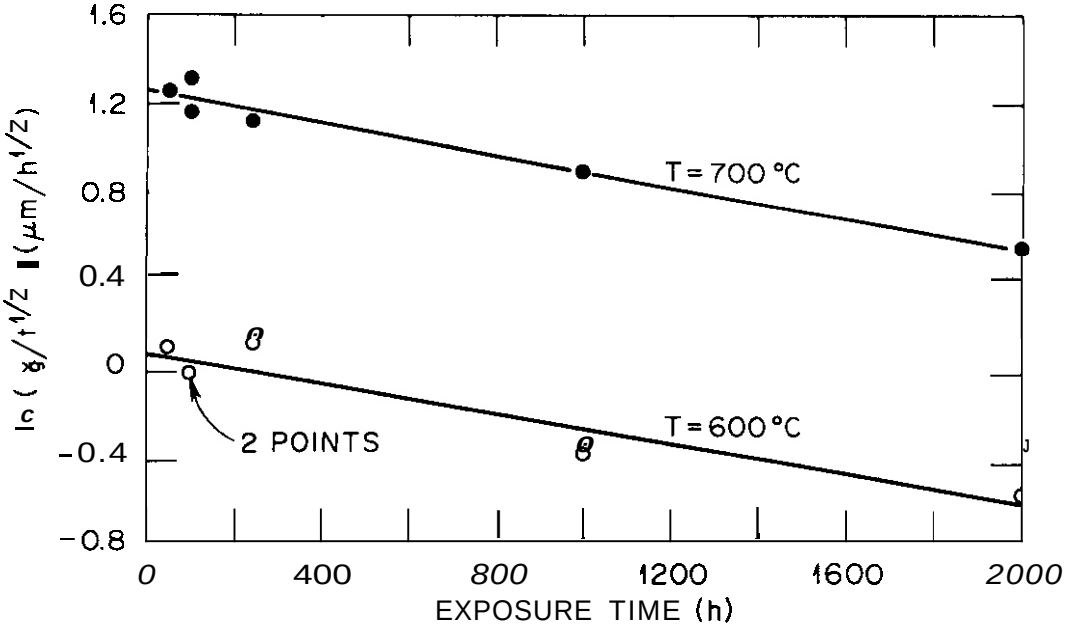

Fig. 8.1.2. Penetration Parameter versus Exposure Time for Type 316 Stainless Steel in Nitrogen-Contaminated Lithium.

We believe that the disagreement between this analysis and the uniform attack depth and the weight losses may indicate that instead of these two quantities being rate limited by a simple diffusion-controlled first-order reaction, they may depend on a solution parameter. In addition, the probable nonuniformity of the solution (stirred was assumed in the model) may partly account for the present discrepancies.

Two sets of capsule experiments are now in progress. One is a study of the corrosion of type 316 stainless steel exposed to lithium at 500, 600, and 700°C as a function of the lithium's nitrogen concentration. The second series is a study of the compatibility of alloys 600 and 800 with static, as-purified lithium. The results from these experiments will be reported in the next progress report.

8.1.5 Conclusions

1. Types 316 and 316L stainless steel are similar in their corrosion rates and the type and extent of surface attack when they are exposed to nitrogen-contaminated lithium.

2. As-rolled type 316L stainless steel showed significantly greater weight losses in Li—2 wt % N at 700°C than fully annealed type 316L exposed under similar conditions.

3. The grain boundary attack of type 316 stainless steel exposed to nitrogen-contaminated lithium at 600 and 700°C can be described by an empirical equation[3] modified by a time-dependent nitrogen concentration of the lithium.

8.1.6 References

1. P. F. Tortorelli and J. H. DeVan, "Capsule Tests of Type 316 Stainless Steel in Nitrogen-Contaminated Lithium," *ADIP Quart. Prog. Rep. Sept. 30, 1978*, DOE/ET-0058/3, pp. 84—91.
2. P. F. Tortorelli, J. H. DeVan, and J. E. Selle, "Effects of Nitrogen and Nitrogen Getters in Lithium on the Corrosion of Type 316 Stainless Steel," NACE preprint 115, to be presented at Corrosion/79, March 1979, Atlanta, Georgia.

3. G. N. Reser, D. L. Olson, and D. K. Matlock, "Liquid Lithium Rate Expressions for Type 304L Stainless Steel," paper to be presented at Corrosion/79, March 1979, Atlanta, Georgia.

8.2 THERMAL-CONVECTION LOOP TESTS OF STAINLESS STEEL IN LITHIUM

P. F. Tortorelli and J. H. DeVan (ORNL)

8.2.1 ADIP Task

ADIP Task I.A.3, Perform Chemical and Metallurgical Compatibility Analyses.

8.2.2 Objective

The purpose of this task is to evaluate the corrosion resistance of possible first-wall materials to flowing lithium in the presence of a temperature gradient. Corrosion rates (in terms of both dissolution and deposition) are measured as functions of time, temperature, additions to the lithium, and flow conditions. These measurements are combined with chemical and metallographic examinations of specimen surfaces in order to establish the mechanisms and rate-controlling processes for dissolution and deposition reactions.

8.2.3 Summary

Weight loss data for a type 316 stainless steel loop that circulated lithium with *500* wt ppm N showed no major difference from a similar loop with purer lithium when differences in flow velocity were taken into account. Further data on weight loss versus exposure time to flowing lithium are reported. Steady-state corrosion rates generally range from 7 to 21 mg/m^2 h between *540* and *600°C*. A simplified analysis of the steady-state corrosion rate as a function of temperature indicates that the corrosion process is controlled by liquid-phase diffusion.

8.2.4 Progress and Status

As described previously,' two types of thermal-convection loops (TCLs) are being used to evaluate the compatibility of austenitic stainless steels with lithium. The first type is in the form of a 0.46-m by 0.64-m parallelogram that contains interlocking tab specimens of the same material as the loop. The loop is operated without interruption for *3000* to *10,000* h and is then cut open to remove tab

specimens for analysis. The second type of TCL is larger (0.48 m by 0.76 m) and is designed so that tab specimens can be withdrawn and inserted without altering the loop operating conditions. In this way, corrosion rates can be monitored at selected time intervals for a given set of test specimens. The present status of the operating loops is given in Table 8.2.1. An additional TCL of the smaller design has been fabricated from alloy 800H (31% Ni, 41% Fe, 22% Cr) and will be tested at 500°C to determine the behavior of higher nickel alloys in flowing lithium.

Table 8.2.1. Present Status[a] of Operating Loops

Loop	T_{max} (°C)	ΔT (°C)	Operating Time (h)	Test Variable
2	600	150	9000	Long-exposure baseline data
3	600	150	3700[b]	Time effect baseline data
4	600	150	2200	Effect of Al additions to the Li

[a] As of Dec. 18, 1978; loops 2, 3, and 4 are large loops with accessible specimens.

[b] Samples removed after 3700 h; lithium flow restricted by plugging.

A small type 316 stainless steel TCL was recently operated for 3000 h with a maximum temperature of 590°C and a temperature difference of 170°C. The lithium that was used in this loop had been purposely contaminated with Li_3N to investigate the effect of 500 wt ppm N in a flowing lithium system. (In static tests,[1,2] 2 wt % N in lithium had adversely affected the corrosion of type 316 stainless steel, while McKee[3] observed a significant increase in mass transfer when the nitrogen content of lithium was increased from 125 to 370 ppm.) The maximum weight loss for this loop is given in Table 8.2.2, which also contains similar data for two other type 316 stainless steel

Table 8.2.2. Comparison of Maximum Corrosion Rates for Three 3000-h Type 316 Stainless Steel Thermal Convection Loops

Lithium Additive (wt ppm)	T_{max} (°C)	ΔT (°C)	Flow Velocity (mm/s)	Max. Weight Loss (g/m^2)
0	600	200	22	33.6
500	590	170	7	23.4
1700[a]	600	200	16	20.5

[a]Lithium was contaminated by exposure to air.

loops. Note that, in view of the lower flow velocity for the test with 500 wt ppm N, no major distinction between the maximum weight losses can be made. While this finding is contrary to McKee's results,[3] it is consistent with the tentative conclusion of Hoffman[4] that nitrogen additions to flowing lithium had no effect on the mass transfer rate. Hoffman noted, however, that grain boundary penetration was more severe in materials exposed to lithium found after test to contain more than 500 wt ppm N. The extent of grain boundary attack in the 500-wt-ppm loop is now being measured.

In the preceding quarterly report,' weight losses versus exposure time were presented for several specimen positions in each of loops 2, 3, and 4. Since then, more data have been recorded from all three loops, and revised plots for specimen positions H3 and H4 (see Fig. 8.2.1) are shown in Fig. 8.2.2. Note that after a transient period the weight losses increase linearly with exposure time. The steady-state corrosion rates are thereby obtained from the slopes of the lines fitted to the data. For loop 2, the acquistion of data points at 8000 and 9000 h has not changed the average hot-leg steady-state corrosion rate reported' earlier. Data points at longer exposure times in loops 3 and 4 have now allowed their corrosion rates to be measured also. The average hot-leg rates for all three loops are given in Table 8.2.3. They are taken as the average of the rates of specimens H2, H3, H4, and H5 (see Fig. 8.2.1), the only positions at

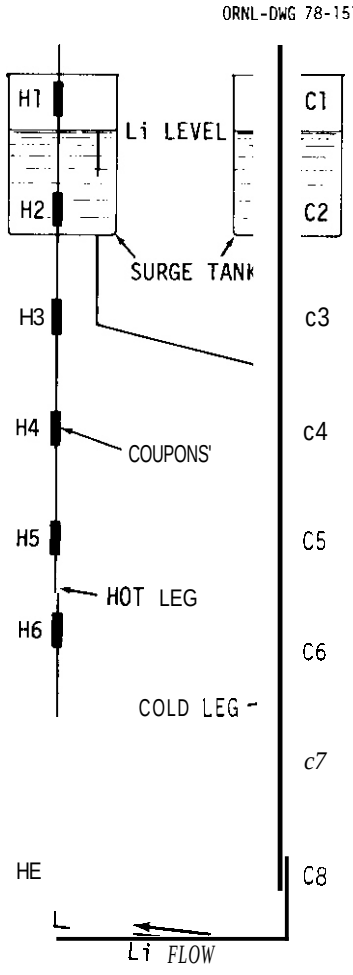

Fig. 8.2.1. Schematic Diagram of Coupons in Positions in a Large Loop.

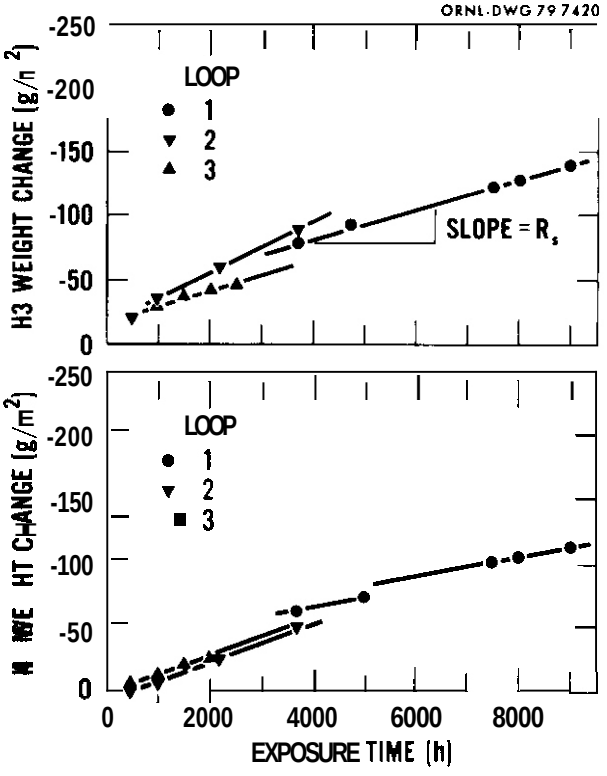

Fig. 8.2.2. Weight Changes as a Function of Exposure Time.

Table 8.2.3. Average Steady-State Corrosion Rates

Loop	Steady-State Corrosion Rate[a]			
	(mg/m² h)	(μg/m² s)	(m/year)	(pm/s)
2	10	2.8	9.0×10^{-6}	0.29
3	14	3.9	1.3×10^{-5}	0.41
4	13	3.6	1.2×10^{-5}	0.38

[a]For the sake of simplicity, these rates are the overall averages of the four coupons in each loop that showed the greatest weight losses.

which significant weight losses are observed. Because of the initial decreasing rate, only the data points for exposure times of at least 1000 h are used to calculate these steady-state corrosion rates. To convert these measurements into surface recession rates the corrosion needs to be uniform. Otherwise, intergranular penetration would render such a value meaningless since the corrosive attack would be significantly greater than the rate of material loss that is calculated from the measured rate. Metallographic examination of several specimens from the hot leg of loop 2 after 9000 h has revealed very little evidence of grain boundary attack (see Fig. 8.2.3). Therefore, the measured corrosion rates can be reported in terms of surface recession and are also listed in Table 8.2.3.

As seen from the data of Fig. 8.2.2 and Table 8.2.3, the corrosion rates in loops 3 and 4 are higher than that of loop 2. As discussed previously,' this may be due to differences in the frequency of sampling. Additionally, the rates in loops 3 and 4 might decrease if

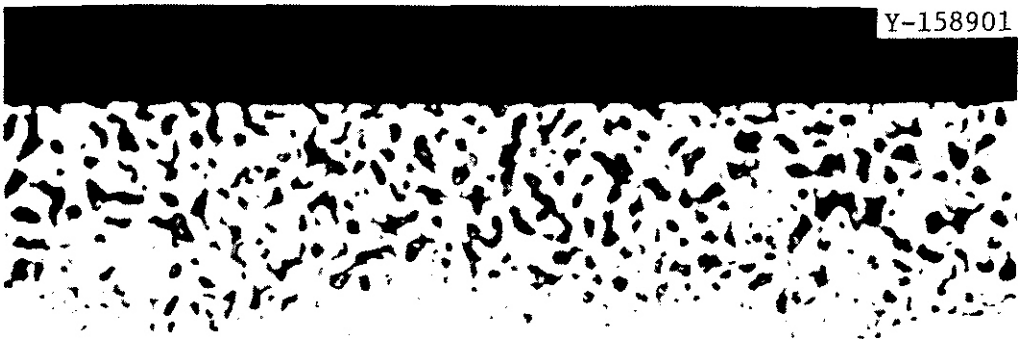

Fig. 8.2.3. Type 316 Stainless Steel after 9000-h Exposure to Flowing Lithium at about 596°C. 500×.

longer term data were added. This would decrease the weighting of the 1000-h data since the latter may reflect some of the initial transient behavior.

Since each specimen in a thermal-convection loop is at a different temperature, we undertook to develop a suitable method for the analysis of the corrosion rates in the hot leg as a function of lithium temperature. Holman[5] found that the corrosion rate, R, (g/m^2 h), in stainless steel sodium thermal-convection loops could be expressed as

$$R = -k \frac{dC_{sat}}{dT} \Delta T \quad , \tag{1}$$

when the rate constant k is small. Here C_{sat} is the equilibrium concentration of solute in lithium and AT is the difference between the temperature, T, of the specimen where R, is measured and that at the point in the hot leg where R, = 0 (529°C in these loops). In general, k and C_{sat} can be assumed to be experimentally dependent on temperature:

$$k = k_0 \exp(-Q/RT) \quad , \tag{2}$$

$$C_{sat} = A \exp(-\Delta H/RT) \quad , \tag{3}$$

where the magnitude of Q depends on the rate-controlling process and AH is the heat of solution of the material in the lithium. Combining Eqs. (1), (2), and (3):

$$R = k_0 A \frac{\Delta H}{T^2} \Delta T \exp[-(Q + \Delta H)/RT] \quad , \tag{4}$$

which upon rearrangement yields:

$$\ln\left(\frac{T^2 R_s}{\Delta T}\right) = \ln(k_0 A \Delta H) - \frac{Q + \Delta H}{RT} \quad . \tag{5}$$

From Eq. (5), we can see that a plot of $\ln(T^2 R_s/\Delta T)$ versus $1/T$ should yield a straight line with a slope equal to $(Q + \Delta H)/R$. Using the corrosion rates from *H3*, *H4*, R5, and H6 (see Fig. 8.2.1), plots based on Eq. (5) were made for each of the three loops. The best fit was for loop *3* (see Fig. 8.2.4), with poorer agreement for loops 2 and *4*. The slope from the plot in Fig. 8.2.4 yielded −81.2 J/mol for the sum $Q + \Delta H$, a value that is much smaller than an activation energy for solid-state diffusion. However, this magnitude would be appropriate for the combination of a heat of solution of iron in lithium (for example, OH for Fe in Li can be estimated to be approximately 59 J/mol from the data of Leavenworth and Cleary[6]) and a Q for diffusion of iron from the stainless steel through the liquid lithium boundary layer to the region of turbulent flow. Therefore, the temperature dependence of the corrosion rate in our loops appears consistent with the model of the corrosion rate being controlled by the liquid-phase diffusion of iron. After this analysis is refined, it will be applied to the data from the small thermal-convection loops, where the greater number of insert specimens should improve the statistical accuracy of a given weight change determination.

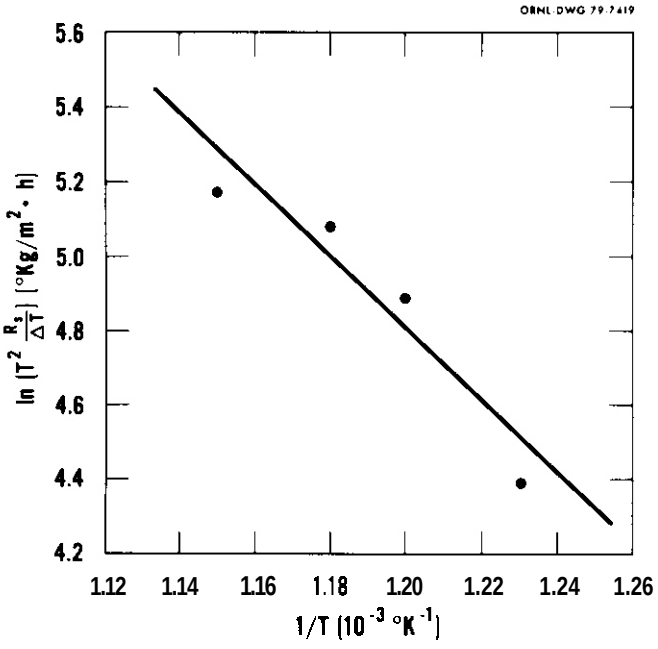

Fig. *8.2.4*. Temperature Analysis of the Corrosion Rate of Loop **3**.

8.2.5 Conclusions

1. Small additions of nitrogen (500 wt ppm) to flowing lithium did not adversely affect the hot-leg weight loss rate at 590°C.

2. Weight losses in thermal-convection loops operated at 600°C exhibit a steady-state behavior in which the corrosion rate becomes linearly dependent on exposure time after about 1000 h of operation.

3. A preliminary analysis of the temperature dependence of the corrosion rates indicates that the diffusion of iron through the liquid lithium surface boundary layer is rate controlling in our larger thermal-convection loop systems.

8.2.6 References

1. J. H. DeVan and J. R. DiStefano, "Thermal-Convection Loop Tests of Type 316 Stainless Steel in Lithium," *ADIP Quart. Prog. Rep. March 31, 1978*, DOE/ET-0058/1, pp. 200–08.
2. P. F. Tortorelli and J. H. DeVan, "Capsule Tests of Type 316 Stainless Steel in Nitrogen-Contaminated Lithium," *ADIP Quart. Prog. Rep. Sept. 30, 1978*, DOE/ET-0058/3, pp. 84-91.
3. J. M. McKee, *Effect of Nitrogen on Corrosion by Lithim*, NDA-40 (June 14, 1957).
4. E. E. Hoffman, Corrosion of *Materials* by *Lithium at Elevated Temperatures*, OWL-2674 (March 9, 1959).
5. W. R. Holman, *Mass Transfer* by *High Temperature Liquid Sodium*, *Interim Progress Report 2, American-Standard Project D-14*, AECU-4072 (Oct. 15, 1958).
6. H. W. Leavenworth and R. E. Cleary, "The Solubility of Ni, Cr, Fe, Ti and Mb in Liquid Lithium," *Acta Metall.* 9: 519–20 (1961).

8.3 HYDROGEN PERMEATION CHARACTERISITCS OF TITANIUM-BASE ALLOYS – E. H. Van Deventer and V. A. Maroni (Argonne National Laboratory).

8.3.1 ADIP Task

I.A.4. Hydrogen Dissolution and Permeation Effects. The results presented in this section contribute to Subtask I.A.4. Milestones I.A.b. and I.A.c.

8.3.2 Objective

The objective of the work reported in this section is to provide base-line hydrogen dissolution and permeation data for the group of titanium-base alloys currently under examination as part of the ADLP Path C alloy development activities[1]. The hydrogen dissolution, outgassing and permeation characteristics of this family of materials is vital to an understanding of their performance as first-wall and blanket structural materials for fusion devices. A further objective of this work is to begin examining methods for overcoming any serious hydrogen isotope uptake and migration problems associated with the rather strong hydride-forming nature of titanium and its alloys.

8.3.3 Summary

The hydrogen permeation characteristics of the alloy Ti-6Al-4V have been evaluated. This alloy was found to have a permeability nearly 1000 times greater than that of conventional 300-series stainless steels. The dependence of the permeation rate on hydrogen pressure, P, was observed to vary over the range from $P^{0.4}$ to $P^{1.0}$. This resultwas construed as evidence for a permeation process that is at least partially influenced by surface impurity effects. The surface condition and mechanical integrity of the Ti-6Al-4V membrane appeared to be unaffected by ∿1400 hours of hydrogen infiltration under typical power-reactor plasma-chamber conditions with respect to temperature, gas pressure and gas composition. A nitride coating (applied by ion-implantation methods) on a second Ti-6Al-4V sample does not appear to have caused a significant reduction in the gross

permeability observed for the initial sample.

8.3.4 Progress and Status

The hydrogen permeation studies of titanium-base alloys[2] have continued through the first quarter of FY-1979. A sample of the alloy Ti-6Al-4V, obtained from J. W. Davis (MDAC), was investigated within the temperature range from 650 to 820 K using hydrogen driving pressures that ranged from *0.4* to 40 Pa. Over the course of this investigation, the dependence of permeation rate on hydrogen driving pressure, P, varied from $P^{1.0}$ during initial phases of the study to as low as $P^{0.4}$ as the experiments progressed. Hydrogen permeability data for the Ti-6Al-4V alloy, normalized to a $P^{0.5}$ pressure dependence for purposes of comparison with other materials, are plotted in Fig.8.3.1 together with the baseline permeability curve for 316-SS determined using the same apparatus and procedures[3]. Although no distinction is made with respect to the order in which individual data were collected, it is generally true that the uppermost points in Fig. 8.3.1 represent measurements taken towards the end of the study.

Considering the scatter in the data and the fact that the pressure dependence was not uniformly close to half-power, no attempt has been made to derive a permeation equation for the subject alloy. (Both the scatter and the variable pressure dependence are construed as evidence that the permeation process is at least partially influenced by surface impurity effects.) For the same reasons, no attempts were made to derive solubility and diffusivity data from the transient portions of each permeation measurement. The results, presented as they are in Fig.8.3.1, are intended to provide insight and guidance concerning the steady-state permeability of the Ti-6Al-4V alloy relative to other materials.

Following completion of the study discussed above, the sample was removed from the permeation assembly and examined visually. After over 1400 hours of hydrogen infiltration under conditions typifying those anticipated in the first-wall region of a fusion reactor, there was no visual evidence of change in appearance or mechanical integrity.

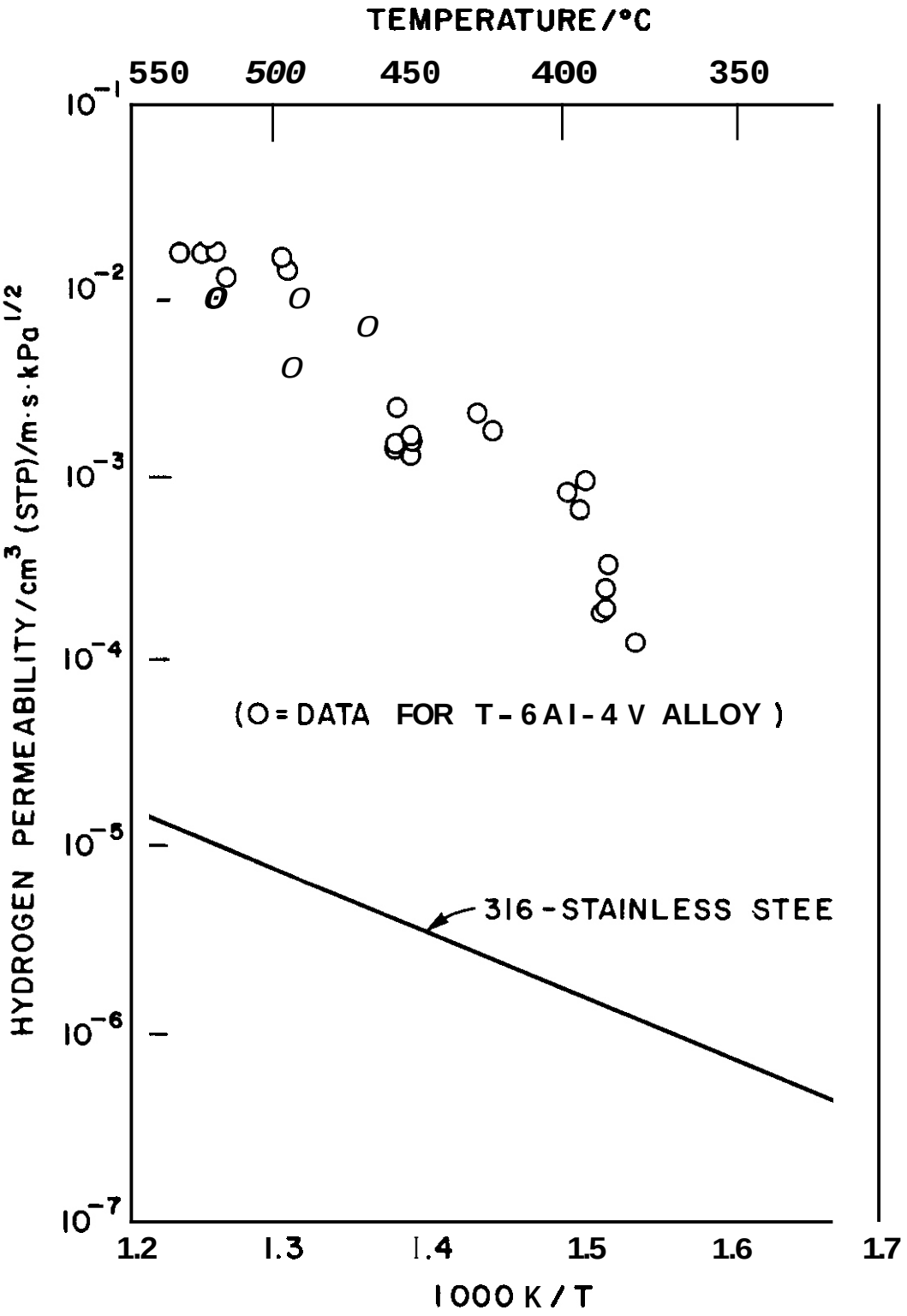

Fig. 8.3.1. Hydrogen permeation data as a function of temperature for Ti-6Al-4V compared to the hydrogen permeability of 316 stainless steel.

Sections of the permeation specimen and the as-received alloy are being prepared for comparative microscopic and microprobic analyses. Also, an attempt is being made to determine the solubility of hydrogen in a sample of the Ti-6Al-4V alloy using steady-state tensimetric methods.

A sample of the Ti-6Al-4V alloy with a nitride coating on the upstream surface[2] is currently under study[4]. Although only a few data points had been collected at the time of this writing, it appears safe to say that only a small reduction (perhaps a factor of 5 or so) in hydrogen permeation rate has been achieved with the nitride coating. The particular coating now being studied was applied by an ion-nitriding method[5]. Plans are being made to prepare an anodized Ti-6Al-4V specimen in collaboration with J. W. Davis of MDAC.

In the previous progress report[2], we presented permeation results for a sample of the 5621S alloy of titanium (Ti-5Al-6Sn-2Zr-1Mo-0.25Si). During the first quarter of FY-1979, a section of that sample was subjected to microstructural analysis by J. W. Davis and coworkers at MDAC. This sample, which had been studied for over 2500 hours at temperatures between 500 and 920 K, gave no indication of any residual hydride phases. (The sample had been outgassed prior to its removal from the permeation assembly.) However, some evidence of a microstructural transformation in the form of very small precipitates was observed. It is suggested (J. W. Davis, MDAC) that these precipitates may be due to in-growth of 6-phase titanium or Ti-Sn compounds. Additional efforts to characterize this specimen are in progress at MDAC.

8.3.5 Conclusions

The Ti-6Al-4V alloy has a hydrogen permeability roughly 1000 times greater than that for ordinary 300-series stainless steels at temperatures (650 and 820 K) and hydrogen pressures (0.4 to 40 Pa) in the range of interest for fusion power reactor first-wall applications. The observation of a non-uniform dependence of permeation rate on hydrogen pressure is tentatively construed as evidence for a

permeation process that is at least partially influenced by surface impurity effects. Over 1400 hours of hydrogen infiltration under typical first-wall operating conditions did not appear to have affected either the surface condition or mechanical integrity of the alloy. Based on preliminary studies, a nitride coating applied to the surface of Ti-6Al-4V does not appear to have afforded the magnitude of permeation reduction needed for this type of alloy.

8.3.6 References

1. J. W. Davis *et al.*, *Microstructure of Titanium Scoping Alloys Prior to Irradiation,* Alloy Development for Irradiation Performance Progress Report for the Period Ending June 30, 1978, U. S. Department of Energy Report DOE/ET-0058/2 (1978) pp. 85-99.
2. E. H. Van Deventer and V. A. Maroni, *Hydrogen Permeation Characteristics of Path A, Path B, and Path C Alloys,* Alloy Development for Irradiation Performance Progress Report for the Period Ending September 30, 1978, U. S. Department of Energy Report DOE/ET-0058/3 (1978) pp. 101-107.
3. E. H. Van Deventer and V. A. Maroni, *Hydrogen Permeation of Type 316 Stainless Steel,* Alloy Development for Irradiation Performance Progress Report for the Period Ending March 31, 1978, U. S. Department of Energy Report DOE/ET-0058/1 (1978) pp. 215-220.
4. Work performed in collaboration with D. M. Gruen (Argonne National Laboratory), G. O'Donnell and G. L. Kulcinski (University of Wisconsin).
5. M.-B. Liu, D. M. Gruen, *et al.*, "Ion Nitriding of Titanium and Zirconium by a D. C. Discharge Method," *High Temp. Sci. 10*:53 (1978).

DOE/ET-0058/4
Distribution
Category
uc-20, -20c

DISTRIBUTION

1-5. Argonne National Laboratory, 9700 South Cass Avenue, Argonne, IL 60439

Director, Materials Science Division
L. Greenwood
V. Maroni
D. L. Smith
H. Wiedersich

6-7 Battelle-Pacific Northwest Laboratory, P.O. Box 999, Richland, WA 99352

J. L. Brimhall
D. Dingee

8 Carnegie-Mellon University, Schenley Park, Pittsburgh, PA 15213

J. C. Williams

9-210 Department of Energy, Technical Information Center, Office of Information Services, P.O. Box 62, Oak Ridge, TN 37830

For distribution as shown in 'TID-4500 Distribution Category, UC-20 (Magnetic Fusion Energy), and UC-20c (Reactor Materials)

211-217 Department of Energy, Office of Fusion Energy, Washington DC 20545

M. M. Cohen
C. R. Finfgeld
T. C. Reuther, Jr. (5 copies)

218. Department of Energy, Oak Ridge Operations Office, P.O. Box E, Oak Ridge, TN 37830

Assistant Manager, Energy Research and Development

219. General Atomic Company, P.O. Box 81608, San Diego, CA 92138

S. M. Rossenwasser

220-223. Hanford Engineering Development Laboratory, P.O. Box 1970, Richland, WA 99352

R. E. Nygren
E. C. Opperman
R. W. Powell
J. L. Straalsund

224–227. Lawrence Livermore Laboratory, P.O. Box 808, Livermore, CA 94550

C. Gatroosis
M. Guinan
C. M. Logan
R. R. Vandervoort

228. Massachusetts Institute of Technology, Cambridge, MA 02139

D. J. Rose

229. McDonnell Douglas Astronautics Company, East, P.O. Box 516, St. Louis, MO 63166

D. L. Kummer

230–232. Naval Research Laboratory, Washington, DC 20375

Superintendent, Materials Science and Technology Division
J. A. Sprague
H. Watson

233–269. Oak Ridge National Laboratory, P.O. Box X, Oak Ridge, TN 37830

Central Research Library (2 copies)
Document Reference Section
Laboratory Records Department (2 copies)
Laboratory Records Department, RC
ORNL Patent Section
E. E. Bloom (20 copies)
D. N. Braski
T. A. Gabriel
M. L. Grossbeck
M. R. Hill
K. C. Liu
P. J. Maziasz
C. J. McHargue
S. Peterson
T. C. Roche
J. W. Woods

270–271. University of Virginia, Department of Materials Science, Charlottesville, VA 22901

W. A. Jesser
D. Wilsdorf

272–275. University of Wisconsin, 1500 Johnson Drive, Madison, WI 53706

R. Conn
P. Wilkes
W. G. Wolfer
G. L. Kulcinski

*U.S. GOVERNMENT PRINTING OFFICE : 1979 0-281-704/43